POLITECNICO DI MILANO

School of Industrial and Information Engineering

Master of Science in Nuclear Engineering

Laser-driven Neutron Sources: A First Numerical Investigation

Advisor:
Prof. Matteo Passoni

Supervisors:
Dr. Luca Fedeli

Graduation Thesis of:
Alessandro Tentori
837226

Academic Year 2017-2018

Abstract

Neutron beams serve an important role in many research fields, including nuclear energy, material science and medical applications. Nowadays, the neutron fluxes are mainly provided by research reactors or by conventional accelerators. These latter accelerate light ions against proper converters, in order to exploit nuclear reactions of the types (p,n), (p,p',n) and (d,n). The neutron fluxes made available from these conventional sources are exploited in order to perform techniques like the crystal lattice analysis, the "neutron activation analysis", the neutron radiography or the "boron neutron capture therapy" (an innovative medical application of the neutron beam). Until recently, the experimental access to a high neutron flux was exclusive to reactor and accelerator-based facilities. In the past few years, the availability of tabletop particle sources based on high intensity lasers has enabled the realization of an alternative high flux neutron generators. Laser-driven ion acceleration relies on ultra-intense ($I > 10^{18}$ Wcm^{-2}), ultra-short ($\sim$10 fs - ps) laser pulses interacting with solid targets. Employing a compact table-top laser ($\sim$ tens of TW of power), it is possible to generate proton bunches characterized by an exponential energy spectrum with maximum energy of some MeV. These energies are suitable for inducing proton-neutron reactions in appropriate targets. Beryllium or lithium are the two main converters suggested by the literature, because of the high values of the (p,n) cross section in this range of energy.
If compared with the conventional neutron sources, laser-driven sources should offer many advantages: the compactness, which leads to more maneuverability and the possibility to develop a portable sources; the simplification of the experimental set-up; the reduction of radioprtection issues; the reduction of the costs (in particular if compared with the construction and the operation of a nuclear reactor).
The purpose of this thesis work is a numerical investigation, performed with the Monte-Carlo code Geant4, on how the variations of the physical parameters of a laser-driven system could affect the generation of neutrons. In particular, in the simulations implemented, low energy proton beams ($\sim$ MeV) impinge on beryllium or lithium converters. Since the numerical tool is essential to the development of the work, a detailed investigations of its behaviour and a benchmark between its outputs and the experimental or theoretical data from literature is carried out.
After ensuring about the reliability of the code, comparisons between monoenergetic and laser-driven proton beam impinging on the converters are carried out. As a parameter of comparison, the mean energy of the exponential energy spectrum of the laser-driven proton beam is setted equal to the energy of the monoenergetic beam. Considering the same number of protons impinging on the

converters, a comparison between the neutron yields, energy spectra and angular distributions arising from the two cases is performed. Moreover, a study of how the converter thickness influences the neutron production is accomplished, with the aim of searching for the optimum solution.
Finally, considering the obtained neutron fluxes, a list of possible applications that it could be realistic to realize with laser-driven sources are presented, also in sight of the future improvement of the technique.

Sommario

Le sorgenti di neutroni ricoprono un ruolo sempre più importante nella ricerca, in quanto vengono impiegate in applicazioni che spaziano dalla produzione di energia (reattori a fissioni), all'analisi dei materiali e alle applicazioni medicali. Al giorno d'oggi i flussi neutronici vengono prodotti tramite l'utilizzo di reattori di ricerca, o sfruttando reazioni nucleari del tipo (p,n) (d,n) (p,p'n) indotte da ioni leggeri carichi accelerati contro opportuni convertitori. I flussi neutronici resi disponibili da queste sorgenti sono comunemente utilizzati per l'esecuzione di tecniche come l'analisi dei reticoli cristallini, la "neutron activation analysis", le radiografie neutroniche o la "boron neutron capture therapy" (un' applicazione medicale basata sull'uso dei neutroni per trattare particolari tumori non trattabili con le tecniche convenzionali).
Negli ultimi anni è stato dimostrato come le sorgenti basate su laser ad alta intensità possano essere sfruttate per la produzione di elevati flussi neutronici. L'accelerazione di ioni tramite laser si basa su impulsi ultra-intensi ($I > 10^{18}$ Wcm^{-2}), ultra-corti ($\sim$10 fs - ps) focalizzati su target solidi. Sfruttando laser compatti "table-top" di potenze dell'ordine di decine di TW, è possibile accelerare ioni, in particolare protoni, caratterizzati da uno spettro di energia esponenziale, che si estende a energie dell'ordine di qualche MeV. Queste energie sono l'ideale per indurre reazioni nucleari di tipo (p,n) in opportuni convertitori e, considerando i loro alti valori delle sezioni d'urto (p,n), i principali materiali suggeriti dalla letteratura sono il berillio e il litio.
Se paragonati alle convenzionali sorgenti neutroniche, le sorgenti basate sui laser potrebbero offrire molti vantaggi. Primo su tutti la compattezza, che offre una maggiore maneggevolezza permettendo di pensare a una portabilità della sorgente, risolvendo così il problema di dover effettuare misure e applicazioni in-situ. Un altro vantaggio è la semplificazione del set-up sperimentale e la riduzione dei problemi legati alla radioprotezione. Infine tramite un sistema laser-driven è possibile un abbattimento dei costi (a differenza dei costi di costruzione e gestione di un reattore nucleare, che sarebbero molto più alti).
L'obiettivo del lavoro di tesi è uno studio numerico, effettuato tramite il codice Monte-Carlo Geant4, su come la variazione di diversi parametri fisici di un sistema laser-driven possa influenzare la resa, lo spettro di energie e le distribuzioni angolari dei neutroni emessi. Nelle simulazioni implementate, fasci di protoni a bassa energia ($\sim$ MeV) urtano su dei convertitori di berillio o di litio. Dal momento che lo strumento numerico è di fondamentale importanza nello sviluppo del lavoro, è stato effettuato uno studio dettagliato del suo comportamento e una validazione dei suoi output con risultati sperimentali o teorici presi dalla letteratura.
Dimostrata affidabilità del codice, è stato effettuato un paragone tra fasci di pro-

toni monenergetici e accelerati da laser. Come parametro di paragone, l'energia media dello spettro esponenziale da laser è stata posta uguale all'energia del fascio monoenergetico. Inoltre è stato effettuato uno studio su come lo spessore del convertitore possa influenzare la produzione di neutroni, con lo scopo di ricercare la soluzioni ottimale in termini di resa.
Infine, considerando i flussi neutronici ottenuti da queste simulazioni, nell'ultima parte della tesi viene presentata una lista di possibili applicazioni potenzialmente eseguibili con sorgenti di neutroni da laser, tenendo conto anche dei futuri sviluppi della tecnica.

Estratto

L'obiettivo del lavoro di tesi è uno studio teorico riguardante la produzione di neutroni tramite reazioni nucleari indotte da fasci di protoni accelerati da laser. Uno degli aspetti approfonditi durante il lavoro svolto riguarda la possibilità di simulare, in maniera affidabile, le reazioni nucleari indotte da protoni a bassa energia ($\sim$ MeV) tramite il codice montecarlo Geant4.
Il neutrone, insieme al protone, è uno dei costituenti fondamentali della materia e, grazie alla sua carica elettrica netta nulla, interagisce principalmente con essa prevalentemente tramite reazioni nucleari o di scattering elastico. Questa peculiarità rende il neutrone una particella unica nel suo genere, particolarmente penetrante nella materia e quindi sfruttata in una vasta gamma di applicazioni. La più importante tra queste è la produzione di energia tramite i reattori nucleari, basati sulla fissione indotta da neutroni. Tuttavia, esistono una serie di altre possibili applicazioni che sfruttano le singolari proprietà di questa particella: nel lavoro di tesi ne sono approfondite alcune.
Grazie al fatto che non interagiscono per via elettromagnetica, i neutroni sono delle particelle altamente penetranti nella materia. Questa proprietà può essere sfruttata per eseguire analisi dei materiali. In particolare, disponendo di sorgenti di neutroni termici monocromatici §1.2.2, §2.3, è possibile sfruttare il fenomeno di diffrazione per l'analisi dei reticoli cristallini e valutare lo stato di sforzo di un materiale in maniera non distruttiva. Questa tecnica è comunemente effettuata tramite raggi X, tuttavia con l'utilizzo di sorgenti convenzionali non è possibile analizzare profondità del materiale maggiori di 100 μm. Tramite l'utilizzo di raggi X da sincrotrone, oppure sfruttando flussi neutronici, è possibile scendere a profondità dell'ordine del $\sim$ mm.
Durante la diffusione nella materia, un fascio di neutroni è sensibile alla presenza di elementi leggeri (Idrogeno, carbonio...) con i quali si verificano fenomeni di scattering elastico. Sfruttando questo fenomeno, è possibile effettuare "radiografie neutroniche" il cui scopo è quello di verificare la presenza di elementi leggeri, spesso legati a fenomeni di corrosione nei metalli o infiltrazioni di acqua nei materiali cementizi.
Una delle tecniche radiochimiche di analisi con la quale è possibile rivelare la presenza di elementi in traccia in una soluzione o in materiale è la "neutron activation analysis" (NAA) §1.2.4. Questa tecnica si basa sulla propensione dei neutroni di indurre reazioni nucleari (n,γ) negli elementi. Rivelando l'energia della radiazione γ con rivelatori al germanio (HPGE) o con gli ioduri di sodio (NAI(Tl)), è possibile identificare la presenza dell'elemento fino a concentrazioni dell'ordine del $\sim$ ng/g. Solitamente questa tecnica è svolta utilizzando neutroni temici, tuttavia esistono varianti come la "fast neutron activation analysis" (FNAA) o la "epitermal neutron activation analysis"(ENAA), che sfruttano

neutroni a energie più alte. Un' ulteriore variante di questa tecnica è la "prompt neutron activation analysis" (PGNAA) , basata sulla rivelazione di raggi gamma pronti a seguito dell'irraggiamento.
Negli ultimi decenni è stata proposta un' applicazione a fini medicali dei neutroni, indirizzata al trattamento dei tumori che presentano delle criticità trattamento con tecniche convenzionali di radioterapia o chirurgia. La "boron neutron capture therapy" (BNCT) si basa sul fatto che i neutroni termici sul ^{10}B danno luogo a una reazione nucleare che ha come prodotti la generazione di due particelle ad alto LET: n + ^{10}B $\rightarrow^{7}$Li + α. Nel caso in cui il boro sia accumulato preferenzialmente nelle cellule tumorali, questi nuclei rilasciano la loro energia provocando danni a queste cellule e uccidendole in maniera selettiva. L'efficacia di questa tecnica risiede quindi nelle capacità di accumulo del radiofarmaco preferenzialmente dei tessuti tumorali, e nella disponibilità di flussi neutronici collimati e non contaminati da altre radiazioni che possono causare danni ai tessuti sani.
A seguito di queste applicazioni sopraccitate, risulta chiaro del perché la ricerca compia costanti sforzi nello studio di sorgenti neutroniche di intensità adeguata. Nella seconda metà del XX secolo, le sorgenti di neutroni più sfruttate furono i reattori nucleari §2.3. Anche al giorno d'oggi ci sono diversi reattori di ricerca sparsi per il mondo, che incanalano un flusso neutronico nelle cosiddette "colonne termiche" per poi sfruttarlo per eseguire i processi menzionati. Due importanti esempi sono il "MITR", che risiede al Massachusetts Institute of Technology (MIT) 2.3, e il CARR, il più potente reattore di ricerca in uso al giorno d'oggi in Cina.
Un altro tipo di sorgente neutronica sono le cosiddette sorgenti da spallazione. Irraggiando elementi pesanti tipo il mercurio con un fascio di protoni ad alta energia ($\sim$ 100 MeV, $\sim$ GeV), si danno luogo alle reazioni di spallazione. In queste reazioni, per ogni protone incidente sul nucleo, vengono rilasciati più neutroni ad alta energia che possono raggiungere le decine di MeV. In Europa è in costruzione la European Spallation Source (ESS) §2.4. Sorgenti di questo tipo offrono i flussi neutronici molto elevati, tuttavia presentano anche degli elevati costi di costruzione e di gestione, oltre che a una serie di problematiche riguardanti la radioprotezione.
Per abbattere i costi e la complessità del set-up sperimentale negli ultimi anni si sono sperimentate delle sorgenti di neutroni basate sulle reazioni indotte da protoni accelerati da acceleratori convenzionali §2.5. In particolare, sfruttando degli acceleratori elettrostatici o dei ciclotroni, è possibile accelerare dei protoni ad energie dell'ordine del $\sim$ MeV, adatti a indurre reazioni nucleari di tipo (p,n) su opportuni convertitori di litio o di berillio. Diversi esperimenti sono stati eseguiti e hanno dimostrato l'efficacia della tecnica, generando flussi neutronici minori rispetto a quelli da reattore, tuttavia sufficientemente intensi per essere sfruttati nelle applicazioni. Queste tipologie di sorgenti presentano costi e problematiche di gestione ridotti, che li rendono appetibili per l'installazione nei laboratori universitari o industriali.
Negli ultimi anni è stata dimostrata la possibilità di accelerare fasci di protoni o di ioni tramite impulsi laser 2.5.4. Questi sistemi si basano sull'interazione laser-plasma tramite impulsi ultra corti ($\sim$ decine di fs o ps) e ultra intensi (decine di TW o PW), con intensità che superano i 10^{18} $\frac{W}{cm^2}$. Controllando i parametri del laser e la tipologia di target irradiato, è possibile raggiungere energie dei protoni dell'ordine delle decine MeV. In generale, lo spettro di en-

ergie che si ottiene da questo sistema è uno spettro ampio, che può essere ben interpolato da funzioni esponenziali. La divergenza angolare di tale spettro va da 6° a 10°, presentandosi più ampia rispetto a quella fornita da un acceleratore convenzionale. Le correnti generate da questi sistemi sono più basse rispetto a quelle generate dagli acceleratori convenzionali, in quanto si attestano sulle $\sim$ 100 nA e dipendono dalla frequenza di sparo del laser, che generalmente va dall' Hz alle decine di Hz.
La capacità di un laser di dimensioni non eccessive ($\sim$ decine di TW) di accelerare protoni ad energia sull'ordine del MeV, apre la strada a una nuova tipologia di sorgente di neutroni, basata su sistemi compatti "laser-driven". In particolare, indirizzando questo fascio di protoni su un opportuno convertitore di berillio o di litio, è possibile dar luogo, come nel caso degli acceleratori convenzionali, a reazioni di tipo (p,n) e quindi alla generazione di neutroni. Diversi esperimenti hanno dimostrato la fattibilità della tecnica: tramite laser di $\sim$ 100 TW, sfruttando convertitori di litio, si sono ottenute fluenze neutroniche dell'ordine di 10^8 neutroni per steradiante. Considerando che l'impulso neutronico ha durata di $\sim$ ns, il flusso di picco risulta essere molto elevato $\sim 10^{18}$ neutroni/cm^2 s.
La possibilità di sfruttare sorgenti laser in futuro porta a diversi vantaggi:

- Riduzione dei costi e semplificazione del set up sperimentale;
- Riduzione delle problematiche legate alla radioprotezione (in particolare se confrontate con un reattore nucleare);
- Portabilità: le sorgenti di neutroni sfruttabili oggi sono pensate per misure o per sviluppo di applicazioni sono in sito. Le possibilità offerte da una sorgente laser driven consentono di ripensare il set-up sperimentale, prevedendone una maggiore versatilità e quindi portabilità.
- Possibilità di sfruttare la natura pulsata della sorgente per applicazioni mirate come la PGNAA.

Lo scopo del lavoro di tesi è quindi quello di effettuare uno studio numerico teorico sull'applicabilità di sorgenti da laser per la produzione di flussi neutronici.
Avere strumenti numerici, che consentano di simulare in maniera affidabile le reazioni nucleari indotte da protoni nel range di energie considerate, può essere utile sotto diversi aspetti: consente di esaminare le caratteristiche del set-up sperimentale, scegliendo la soluzione ottimale in termini di geometria del target ed energie dei protoni incidenti; di valutare alcuni aspetti radioprotezionistici, come il rateo di dose e la predisposizione di schermature; consente infine di interpretare i risultati sperimentali.
Geant4 §3 è un codice Monte-Carlo che permette di simulare il trasporto di particelle all'interno della materia. La fisica inclusa nel codice copre una vasta gamma di processi fisici: elettromagnetici, ottici e adronici. Il range di energie coperto dal codice va da $\sim$ eV fino ai $\sim$ TeV. Nel software sono inclusi anche un'ampia serie di particelle, materiali ed elementi. Il codice è scritto nel linguaggio informatico C++, e offre all'utente la possibilità di sviluppare la sua applicazione definendo la geometria e i materiali coinvolti, le particelle e gli elementi implicati e i processi fisici considerati. In letteratura il codice è stato usato per simulare l'interazione di particelle alle alte energie (LHC); per studiare

il rilascio di energia di particelle nella materia; per applicazioni radioprotezionistiche vicino agli acceleratori o nello spazio; per lo studio dei raggi cosmici.
Il software è organizzato in classi, ciascuna delle quali è riferita a un determinato ambito della simulazione. L'utente deve sviluppare le sue classi concrete, basate sulle classi virtuali che il codice fornisce, in modo da implementare la sua simulazione. In particolare le classi da definire sono:

- : **DetectorConstruction**: questa classe si occupa della geometria del sistema. L'utente deve implementare i materiali e gli elementi coinvolti nella simulazione, e definire le loro forme geometriche. Per fare ciò, il codice mette a disposizione una vasta gamma di metodi e di classi e librerie, in modo da fornire versatilità.

- : **PrimaryGeneratorAction**: in questa classe è possibile definire il fascio di particelle primarie. Il codice fornisce tre appositi metodi per definire posizione, energia e momento iniziale delle particelle.

- : **PhysicsList**: in questa classe l'utente deve implementare i processi fisici coinvolti nella simulazione. Dal momento che il codice permette di simulare diverse tipologie di processi che coprono un vasto range di energia, l'utente deve scegliere tra questi quelli adatti ai suoi scopi.

- **SteppingAction**: in questa classe vengono definiti gli elementi sensibili della geometria, atti a raccogliere le informazioni che l'utente vuole estrapolare nel corso della simulazione. È possibile ad esempio registrare il numero di particelle che raggiunge un dato volume, la loro energia cinetica e il loro momento.

- **AnalysisManager**: in questa classe le informazioni raccolte dalla classe precedente vengono raccolte e messe in istogrammi.

- **Main()**: Questo è il punto di accesso del programma. Tutte le classi che l'utente ha sviluppato nella simulazione devono essere istanziate al suo interno, in modo da dare al programma tutte le informazioni per sviluppare la simulazione.

Una particolare attenzione va riservata alla fisica del implementata in Geant4. I vari processi fisici implementati sono raggruppati in 5 principali categorie:

- **Processi elettromagnetici**,

- **Processi adronici**;

- **Processi ottici**;

- **Decadimento radioattivo**;

- **Processi foto-leptonici**;

I processi rilevanti ai fini del lavoro di tesi sono in particolare i processi elettromagnetici e i processi adronici.
La fisica elettromagnetica implementata in Geant4 consente di simulare il rilascio di energia di particelle cariche nella materia, considerando tutti i fenomeni ad esso connessi (produzione di elettroni secondari, bremsstrahlung, eccitazione

e ionizzazione di atomi ...). Permette inoltre di simulare i processi indotti da fotoni nella materia (effetto fotoelettrico, produzione di coppie, effetto Compton);
La fisica adronica implementata in Geant4 ricopre diversi ordini di grandezza, dagli eV fino ai TeV. Diversi modelli sono considerati:

- *Quark-Gluon-String-Parton* (QGSP): questo modello ricopre un range di energia che va dai 20 GeV ai 50 TeV;
- *Fritiof* (FTF): come il precedente, questo modello simula interazioni adroniche per $P_{lab} > 3$ GeV/c;
- *Bertini cascade* (BERT): questo modello simula una cascata nucleare indotta da adroni. Valido da 0 a 10 GeV;
- *Binary cascade* (BIC): altro modello che simula una cascata nucleare indotta da adroni. Valido da 0 a 3 GeV;
- *INCL++*: questo modello è stato sviluppato per la simulazione di fenomeni di spallazione, quindi per particelle con energie $\sim$ 100 MeV;
- *ParticleHPInelastic*: modello per la simulazione dell'interazione e il trasporto dei neutroni nella materia, o per la simulazione di reazioni indotte da particelle cariche a bassa energia.

I primi cinque modelli sono basati su formule teoriche che forniscono il valore delle sezioni d'urto e le probabilità di decadimento. Sono ben validati per applicazioni alle alte energie. Si parla quindi di "Theory-driven models".
Il modello *ParticleHPInelastic* acquisisce i dati relativi alle sezioni d'urto dalle librerie ENDF:B-VII e TENDL. Si parla quindi di "Data-driven model". L'utente può sviluppare la sua classe "PhysicsList" implementando i processi di suo interesse, oppure può riferirsi a "Pre-compiled PhysicsList", ossia a liste precompilate, messe a disposizione dal codice, che ricoprono i casi più classici 3.3.7. Queste sono:

- *G4HadronPhysicsFTFP_BERT_HP*
- *G4HadronInelasticQBBC*
- *G4HadronPhysicsINCLXX*
- *G4HadronPhysicsQGSP_BIC_HP*
- *G4HadronPhysicsQGSP_BIC_All_HP*.

È importante sottolineare come solo nell'ultima PhysicsList (*G4HadronPhysicsQGSP_BIC_All_HP*) sia implementato il modello data-driven *ParticleHPInelastic*.
In letteratura il codice è ampiamente validato per la simulazione di processi ad elevata energia (dai $\sim$ 100 MeV in su) e per il trasporto di particelle cariche o di neutroni nella materia a bassa energia ($\sim$ eV), Tuttavia c'è una mancanza di documentazione relativa al suo comportamento nella simulazione di reazioni indotte da particelle cariche a bassa energia ($\sim$ MeV).
Nella prima parte del lavoro di tesi è stato quindi necessario accertarsi del corretto funzionamento del codice, confrontando i suoi output con risultati sperimentali o lavori teorici presi dalla letteratura.

Le simulazioni implementate consistono quindi in convertitori di berillio o litio, sui quali incide un fascio di protoni monoenergetico, utilizzando le "PhysicsList" sopraccitate. Nel caso del berillio, l'energia del fascio monoenergetico è stata settata a 3.7 MeV, mentre nel caso del litio a 2.25 MeV (in modo da riprodurre situazioni presenti in letteratura). Come output il codice fornisce la resa, lo spettro di energia e la distribuzione angolare dei neutroni emessi dal convertitore.
Nel caso in cui il convertitore sia fatto di berillio, i modelli theory-driven sottostimano la resa totale di un fattore 100, rivelandosi inadeguati alla simulazione. Un maggiore accordo in termini di resa e spettro è ottenuto tramite il modello data-driven, il quale sottostima la resa neutronica del 22 %, ma si rivela più efficiente rispetto ai precedenti.
Nel caso in cui il convertitore sia fatto di litio, i modelli theory-driven risultano ancora una volta inadeguati, non prevedendo l'emissione di alcun neutrone. I modelli data-driven si rivelano maggiormente adeguati anche in questo caso con una sottostima di circa il $\sim 20\%$ rispetto ai dati da letteratura.
La validazione del codice e la conoscenza della precisione dei modelli implementati in esso sono importanti non solo ai fini di questo lavoro di tesi, ma anche per lo sviluppo di ulteriori applicazioni che simulino interazioni simili negli stessi range di energia.
Una volta accertatisi dell'affidabilità del codice, è possibile ritenere validi i risultati che seguono nel capitolo 5 della tesi, dove è svolto un paragone tra neutroni generati da protoni monoenergetici (accelerati da un acceleratore convenzionale), e protoni generati da un'interazione laser-plasma. In particolare è stato scelto uno spettro esponenziale ideale, che presenta come estremi di energia 2 e 10 MeV, e ha un valore medio di energia pari a 2.66 MeV. Come termine di paragone, l'energia media dello spettro esponenziale laser-driven è stata posta uguale all'energia del fascio monoenergetico. Nel caso monoenergetico, lo spessore del convertitore è stato settato in modo da fermare completamente i protoni al suo interno, mentre nel caso esponenziale, diversi spessori sono stati implementati nelle simulazioni in modo da studiarne l'effetto sulla resa neutronica. Questo studio è stato effettuato per ricercare la soluzione ideale in termini di resa, ma anche di fattibilità da un punto di vista industriale. In tutte le simulazioni è stato lanciato un numero di protoni pari a 10^9, essendo questo l'ordine di grandezza di protoni accelerati per singolo impulso laser (i.e. $\sim 10^9$, 10^{10}).
In generale, le rese neutroniche sono simili nei casi laser-driven e fascio monoenergetico. Nel primo caso gli spettri neutronici si estendono fino a energie superiori rispetto al secondo. I risultati sono coerenti con il fatto che nel primo caso ci sono protoni a più alta energia che conseguentemente eccitano neutroni a più alta energia. Per quanto riguarda le distribuzioni angolari, esse risultano maggiormente piccate in avanti per i casi laser-driven.
Considerando che, come evidenziato in precedenza, il singolo impulso laser accelera all'incirca $\sim 10^9$, 10^{10} con frequenze che possono andare dal $\sim$ Hz a decine di Hz, la corrente neutronica stimata di è di circa $\sim 10^7$, 10^6 n/secondo. Flussi di neutroni con le caratteristiche trovate, possono essere sfruttati per l'esecuzione di alcune applicazioni come la NAA, la ENAA o la PGNAA, o le radiografie neutroniche. Considerando le caratteristiche epitermiche del flusso risultante, è anche possibile uno sviluppo della BNCT.
I risultati sviluppati in questo lavoro di tesi rendono le sorgenti di neutroni basate su laser una tecnologia promettente. Se lo sviluppo della tecnologia sarà

all'altezza della aspettative, questa potrà diventare uno strumento alla base di molte applicazioni.

Contents

List of Figures

List of Tables

Chapter 1

Neutrons: basic properties and applications

1.1 Fundamental properties of the neutron

Together with the proton, the neutron is one of the building block of matter at the nuclear scale. It is constituted by one quark up and two quarks down and, considering that the charge of these subatomic particles is $\frac{2}{3}e$ and $-\frac{1}{3}e$ respectively (where e is the proton charge, 1.602×10^{-19} Coulomb), the overall charge of neutron is "zero". For this neutron appears as a unique particle, distinguished by the absence of nearly all electrical properties: "no" electrical charge, "no" electrical dipole moment and "no" electrical polarizability. Up to now, the word "no" means "absolutely no", but the electrical properties of neutron remain still object of refined experimentes [22]. Since the neutron is composed by three quarks, it belongs to the family of hadron and in particular it is classified as baryons. A brief classification of quarks is given in table 1.1 from [16]. Even though the neutron is a neutral particle, its magnetic moment

Quark	Rest Mass $\frac{GeV}{c^2}$	Electric charge
u (up)	0.31	2/3
d (down)	0.31	-1/3
c (charm)	1.6	2/3
s (strange)	0.5	-1/3
t (top)	180	2/3
b (bottom)	4.6	-1/3

Table 1.1: Classifications of quarks and their properties. From [16].

is not zero and it interacts with magnetic fields. The magnetic moment is an indication of its quark substructure and its internal charge distribution. The first experimental measure of the neutron magnetic moment was performed by Alvarez and Bloch in 1940 [23]. Nowadays the measured value is equal to -1.913 μ_n, where μ_n is the nuclear magneton defined in the equation 1.1:

$$\mu_n = \frac{e\hbar}{2m_p} = -9.662 \times 10^{27} JT^{-1} \ (in\ S.I\ units) \tag{1.1}$$

where e is the proton charge, $\hbar$ is the reduced Planck constant and m_p is the proton mass [24].
The semi-integer spin makes the neutron a fermion. The rest mass of this particle is equal to 1.674 $\times$ 10^{-27} Kg or 939,57 $\frac{MeV}{c^2}$, slightly greater than the proton one. In vacuum it decays through the beta channel n $\rightarrow$ p^+ + e^- + $\overline{\nu}_e$ with an half life of $\sim$ 10.6 min [18]. The properties of the neutron are summarized in table 1.2.

The first experimental observation of neutrons occurred in 1930 when Bothe

Mass	m_n = 1.674 $\times$ 10^{-27}
Magnetic moment	μ = -1.913μ_n = -0.96623 $\times$ 10^{-26} J/T
Charge	0 Coulomb
Spin	1/2

Table 1.2: Fundamental properties of neutron.

and Becker bombarded beryllium targets with α particles, obtaining a very penetrating but not ionizing radiation. Later, Irène Curie and Joliot noticed that this radiation on paraffin caused the release of protons, but they were not able to explain its nature. In 1932 Chadwick identified this radiation as neutral particle with mass similar to that of proton:
"We must conclude that the beryllium radiation does in fact consist of particles, and that these particles have a mass about the same as that of a proton. Now the experiments further showed that these particles can pass easily through thicknesses of matter, e.g. 10 or even 20 cm lead. But a proton of the same velocity as this particle is stopped by a thickness of 0.25 mm of lead. Since the penetrating power of particles of the same mass and speed depends only on the charge carried by the particle, it was clear that the particle of the beryllium radiation must have a very small charge compared with that of the proton. It was simplest to assume that it has no charge at all. All the properties of the beryllium radiation could be readily explained on this assumption, that the radiation consists of particles of mass 1 and charge 0, or neutrons" [25].

1.2 Examples of selected applications

1.2.1 Introduction

As uncharged particle, the neutron is unaffected by the Coulomb force and it interacts with atoms via nuclear and magnetic scattering or inducing nuclear reactions. For these reasons, the particle presents high penetrability in matter and opened new fields of study, from the material analysis to medical applications. In particular, exploiting the elastic scattering phenomenon, it is possible to explore the crystal structure of materials or to investigate the presence of light elements like hydrogen through neutron radiography §1.2.2 §1.2.3. On the other side, the ability of this particle of induce nuclear reactions is at the basis of fission reactor physics, but it could be also exploited for other applications such as the neutron activation analysis, to evaluate the presence of elements in trace in samples §1.2.4. In the last decades, also a medical application based on neutrons induced reactions on boron has been proposed to treat tumors which

present critical issues in operating with conventional therapies §1.2.5. The aim of these paragraph is to present some selected applications based on the unique way through which the neutron interacts with matter.

1.2.2 Characterization of the crystalline structure

Neutron-based techniques constitute a powerful and non-destructive method for material characterization. They can give bulk information and are a very sensitive probe of light elements, in particular hydrogen and its isotopes.
Considering that the neutron mass is comparable to those of light nuclei, thermal neutrons show a wave-length of the order of interatomic distances in condensed matter, ~ 0.1 nm, and kinetic energy close to atomic vibration energy, $\sim 10^{-2}$ eV. For these reasons, when they interact with matter, they give rise to diffraction phenomena or they can absorb or emit phonons, raising the possibility of spectroscopic analysis. Both phenomena are revealed by analysing the change of direction and speed of thermal neutrons. In the case of scattering the crystal can be seen as an array of many scattering centres constituted by single nuclei that re-irradiates the incident radiation in all directions as a spherical wave.
The neutron-matter interaction is generally weak and can be described by the perturbation theory in Born approximation. Let us consider a parallel and monochromatic neutron beam incident on a sample, characterized by a wavevector $\mathbf{k}_i$ and energy E= $\frac{\hbar^2|\mathbf{k}_i|^2}{2m}$ where m is the mass of neutron. The interaction between the particles and the crystal is governed by mean potential energy field U($\mathbf{r}$) which has the same shape of the direct lattice. The wave function of scattered particles is determined by the time-independent Schroedinger equation 1.2

$$-\frac{\hbar^2\nabla^2\psi(\mathbf{r})}{2m} + U(\mathbf{r})\psi(\mathbf{r}) = E\psi(\mathbf{r}). \tag{1.2}$$

In the case of elastic scattering we can write $|\mathbf{k}_i|^2 = |\mathbf{k}|^2 = \mathrm{k}^2$ and the equation 1.2 can be written as

$$(\nabla^2 + k^2)\psi(\mathbf{r}) = \frac{2mU(\mathbf{r})}{\hbar^2}\psi(\mathbf{r}) \tag{1.3}$$

The initial state of incoming particle is described by the plane wave 1.4

$$\varphi(\mathbf{r}) = e^{(i\mathbf{k}_i\cdot\mathbf{r})}. \tag{1.4}$$

The main approximations used in this treatment are the *far-field approximation* which consists in setting our detector of scattered waves in a point far from the finite crystal, and the *Born approximation* in which the potential energy is considered as a perturbation of kinetic energy. Considering this, it is possible to solve the equation 1.3 and to write the scattered wave function as the sum of the incoming plane wave plus a spherical wave modulated by scattering amplitude A_{si}

$$\psi(\mathbf{r})_s = e^{(i\mathbf{k}_i\cdot\mathbf{r})} + A_{si}\frac{e^{ikr}}{r}. \tag{1.5}$$

It is possible to show that the scattering amplitude is proportional to the Fourier transform of the interaction potential energy over the volume of scattering:

$$A_{si} = -\frac{m}{2\pi\hbar^2}\int_V U(\mathbf{r}')e^{-i\mathbf{Q}\cdot\mathbf{r}'}d\mathbf{r}' \tag{1.6}$$

where $\mathbf{r}'$ are the positions of scattering centres and $\mathbf{Q} = \mathbf{k}_i - \mathbf{k}_f$ is the scattering vector.
Exploiting the lattice periodicity one can write $U(\mathbf{r}) = \sum_{hkl} U_{hkl} e^{\mathbf{g}_{hkl'}\mathbf{r}}$ where *hkl* are the miller indexes and $\mathbf{g}$ is the reciprocal lattice vector. In the case of elastic scattering, substituting U($\mathbf{r}$) in equation 1.6, it is possible to obtain:

$$A_{si} = \frac{4\pi^2 m}{\hbar^2} \sum_{hkl} U_{hkl} \delta \left(\mathbf{Q} - \mathbf{g}_{hkl} \right) \tag{1.7}$$

and the well known Bragg law

$$2d_{hkl} sin\theta_{hkl} = n\lambda. \tag{1.8}$$

Hence the scattering amplitude is not zero if and only if $\mathbf{Q} = \mathbf{g}_{hkl}$ and the peak intensity is proportional to the squared modulus of U_{hkl} which depends on the position of nuclei in the primitive cell (scattering centres). In particular, considering the short range of interaction between neutrons and nuclei, one can write the potential in the form 1.9:

$$U(\mathbf{r}) = \sum_{p=1}^{s} \delta(\mathbf{r} - \mathbf{r}_p) \tag{1.9}$$

where $\mathbf{r}_p$ is the position of the nucleus in the unit cell. In this case the scattering amplitude will be proportional to the squared modulus of the quantity

$$F_{hkl} = \sum_{p=1}^{s} b_p e^{-i\mathbf{g}_{hkl}\cdot\mathbf{r}_p} \tag{1.10}$$

where b_p are the scattering amplitudes of nuclei and F_{hkl} is called *geometric structure factor* [26].

Measurement of stress in material

From this theory of scattering, it is easily understandable that diffraction peaks result from the coherent scattering of incident beam with the periodic structure of a crystal. This means that only periodic domains of the material can be analysed with this technique. However the crystal structure is altered by defects and discontinuities such as vacancies, substitution or interstitial atoms, grain boundaries etc. These discontinuities do not take part in the diffraction phenomena, but will lead to a re-diffused wave. For this it is necessary to consider a sample volume small enough to contain a negligible number of discontinuities. Analysing this volume, the mean angular position of the diffraction spots is linked by the Bragg law to the lattice spacing d_{hkl}, which is related to the lattice strain in the direction normal to the diffracting planes. The peak intensity is linked to the number of elementary sources contributing to the diffraction phenomenon, and the peak shape is related to the size of the coherently diffracting domain and to its local micro-strain distribution. Hence, with this technique it is possible to achieve information about the *macrosstresses*, (stresses that are homogeneous over very large number of crystal domain), but also about *microstresses* (stresses that are homogeneous along the crystal domain).

It must be pointed out that diffraction is not sensitive to the plastic deformation, which is produced by the displacement or multiplication of crystal defects. Diffraction with conventional X-ray sources can provide determinations of stress to less than 100 μm deep, while with synchrotron radiation and neutrons, penetration depths of a few millimetres or centimetres, respectively, can be achieved in specific materials [2].
The use of neutrons to measure strains began in the late 1970, fifty years after the first use of X-ray for that purpose. In 2009 it was found out that this technique could reach a deep resolution of $\sim$ 0.1 mm and could give information about strain gradient with sufficient detail. In the experiment the incident and reflected beam apertures define a gage volume of the shape of a wide but thin parallelepiped, and the strain along the depth of the sample is scanned. A schematic view is shown 1.1. The incident beam is filtered with cadmium sheets in order to follow the outline of specimen surface and enter in the sample. Different orientations of the scattering vector $\mathbf{Q}$ are achieved by combinations of different specimen orientation or through different wavelengths, but since it is difficult to reproduce a wavelength with sufficient accuracy, it is necessary to measure a reference or unstressed d_0 sample at each orientation and each wavelength.

This experiment demonstrated that neutron diffraction can be successfully used for the non-destructive investigation of sub-surface strains for a class of materials that previously were analysed with destructive methods (X-ray diffraction with layer removal) [1].
To perform diffraction analysis a monochromator is necessary. Indeed the usual neutron sources used in this type experiment are research reactors or spallation sources that provide a borad spctrum which must be attenuated and filtered. Most common monochrmator materials are highly oriented crystal of pyrolitic graphite, copper or hot-pressed germanium that, exploiting the Bragg law 1.8, are able to select the chosen wavelength. Collimators before and after the monochrmoator define the angular spread of the neutron beam [2]. Figure 1.2 shows a scheme of neutron diffractometer facility.

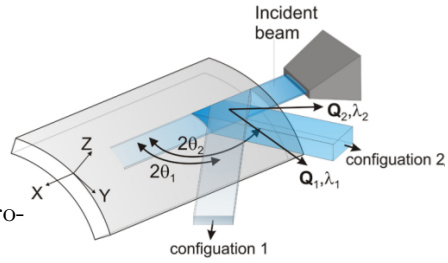

Figure 1.1: Neutron stress determination with high resolution from [1].

1.2.3 Neutron radiography

During the propagation into materials, a neutron beam is particularly sensible to light elements such as hydrogen, carbon or oxygen. Neutron radiography exploits the scattering or absorption contrast between different elements to give information about material. The technique involves three principal components shown in figure 1.3:

- a suitable neutron beam;
- an object of radiographic interest;

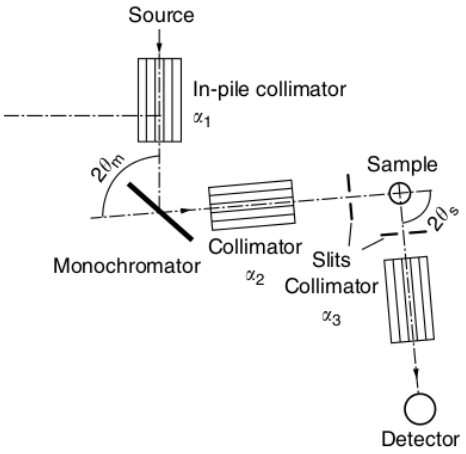

Figure 1.2: Schematic diagram of a neutron diffractomer from [2].

- a device to record the radiation intensity information associated with the neutron beam transmitted through the object.

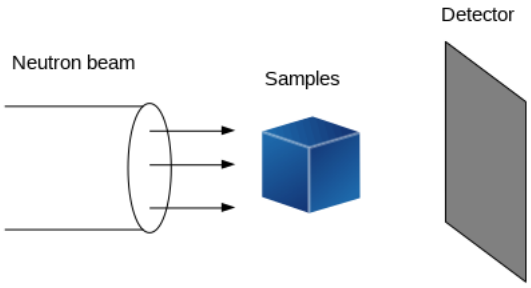

Figure 1.3: Principal components of a neutron radiography system.

Neutron radiography is primarily performed with thermal neutrons §2, which are usually produced by fission reactor §2.3. Considering that the typical reactor fluxes present a fast component ($\sim$ MeV) it is necessary to filter, to slow down and to collimate the neutron beam[27].
When neutrons pass through the target to be analysed, they interact with nuclei by scattering and absorption leading to an attenuation of the beam. This attenuation is registered by a proper detector.
Since neutrons do not ionize directly the matter, they do not directly lead to the formation of developable centers in conventional radiographic film. Hence it is necessary the placement of a converter chosen for its efficiency to capture neutrons and emit appropriate radiation: a metallic foils which emit internal conversion electrons, alpha particles, y-rays, or light-emitting scintillation screens are frequent choices.
Very recent applications of this technique was done in China at the CARR

reactor §2.3, in order to study the penetration of water and other aqueous solutions into cracked cementitious specimens. The neutron flux that irradiated the cracked samples was of $1.2 \times 10^8 \frac{n}{cm^2 s}$ and a A 0.1 mm thick neutron sensitive 6 Lif/ZnS scintillation screen was used. The process of water penetration into the cracked mortar was followed by neutron radiography, demonstrating the effectiveness of the technique to capture the early time dynamics of the rapid penetration of water into cracked cement-based material [28].
Neutron radiography offers also the possibility to reveal hydrogenated component in metallic structures or to perform various metallurgical controls, such as the aluminium corrosion, with a non-destructive method. This technique was employed in the study of corrosion of the main rotor of helicopter blades: in particular the study tried to detect $Al(OH)_3$, AlO(OH) and water in aluminium structures exploiting the high scattering neutron attenuation cross section of hydrogen against the low neutron attenuation cross section of Al. This fact makes aluminium almost transparent to neutrons but the corrosion products, oil or water ingress, are highly opaque. Samples were analysed with maximum thermal neutron flux of $1.2 \times 10^7 \frac{n}{cm^2 s}$ delivered by a research reactor with a thin gadolinium filter. Before the irradiation the blades were cleaned with acetone to remove all visible contaminants from the surface. The radiography was performed with the aid of T200 Kodak films exposed for 45 s.
As can be seen from figure 1.4, neutron radiography produces excellent results in detecting water or oil ingress, and the formation of corrosion product [3].

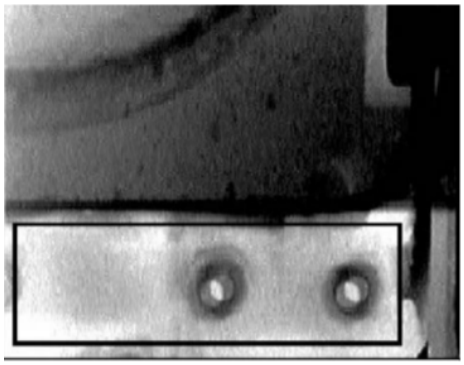

Figure 1.4: de Beer et al. Neutron radiograph showing corrosion product [3].

1.2.4 Neutron activation analysis

The neutron activation analysis (NAA) is a radiochemical technique that makes use of nuclear reactions to generate radionuclides or excited states in the target nuclei, whose decay is at the basis of analytical determination. In the NAA the nuclei undergo trough a (n,γ) reaction. Exploiting the half life λ and the energy of radiation emitted it is possible to perform a quantitative analysis, identifying the amount and the type of nuclide present in the medium. Irradiating the target with a neutron flux ϕ, the rate of accumulation of the radionuclides N^* is given by the equation 1.11:

$$\frac{dN^*}{dt} = N\sigma\phi - \lambda N^* - N^*\sigma^*\phi \tag{1.11}$$

where N is the total number of nuclei in the target and σ and σ^* are the neutron capture cross section for the initial and activated nuclei respectively.
After an irradiation time T, the activity will be 1.12:

$$A(t) = n\sigma\phi\left(1 - e^{(-\lambda T)}\right)e^{(-\lambda t)}. \tag{1.12}$$

Hence an important parameter to choose the irradiation time T, which is a function of the half life of the element. Generally T doesn't exceed weeks or one month.
Different types of neutron sources are employed in the NAA. The most common method is to exploit reactor fluxes, but it is also possible to use spontaneous fission sources, t(d,n)α or ^{9}Be(d,n)^{10}B sources and high energy neutrons from spallation reactions. With typical reactor fluxes, i.e $\phi \sim 10^{14}\frac{n}{cm^2 s}$, induced reactions are mainly (n,γ) and, due to the relatively high cross section for most element, an activity of 10 Bq allows detection limits of the order of $10^{-14}\frac{g}{g}, 10^{-10}\frac{g}{g}$, in general not available by other analytical methods. Table 1.3 lists limits of detection for different nuclei for irradiation time of one hour with typical reactor fluxes.

Detectable in 1 g of sample [g]	Irradiation time 1 h
$10^{-14}10^{-13}$	Dy
$10^{-13}10^{-12}$	Co, Rh, Ag, In, Eu, Ir
$10^{-12}10^{-11}$	V, Mn, Se, Br, I, Pr, Er, Yb, Hf, Th
$10^{-11}10^{-10}$	Mg, Al, Cl, Ar, Cu, Ga, Nb, Cs, Sm, Ho, Lu, Re, Au, U
$10^{-10}10^{-9}$	F, Na, Ge, As, Kr, Rb, Sr, Mo, Ru, Pd, Sb, Te, Ba, La, Nd, Gd, W, Os, Hg, Tl
$10^{-9}10^{-8}$	Ne, Si, K, Sc, Ti, Ni, Y, Cd, Sn, Xe, Tb, Tm, Ta, Pt
$10^{-8}10^{-7}$	P, Cr, Zn, Ce
$10^{-7}10^{-6}$	S, Zr, Pb, Bi
$10^{-6}10^{-5}$	O, Ca

Table 1.3: limits of detection for different elements for irradiation time of one hour. From [17].

As one can notice, light elements (H, Be, Li, O, N, C, B) are not present in the table because they show low activations under neutron flux, and they must be detected with other technique. Li and B undergo through (n,α) reaction.
It should be mentioned that the energy spectrum of neutrons from reactor differs considering different reactors or different position of irradiation, therefore it is necessary to use standards that are irradiated under the same conditions and at the same position as the samples to be analysed. Considering this, NAA is not performed to determine the absolute amount of an element in a sample, but it is referred to a standard one irradiated in the same conditions, i.e same

irradiation time, same position in the reactor, and analysed by same detector (with same efficiency). In this way, knowing the mass m_s of the element in the standard, revealing the activity of the sample A_x and of the standard A_s, it is possible to calculate the mass of the element in the sample:

$$m_x = \frac{A_x}{A_s} m_s. \tag{1.13}$$

Due to its high sensitivity, NAA is one of the most important methods for the determination of microcomponents and trace elements in materials of high purity or in water or biological samples. A great advantage of this technique is the possibility to determinate a large number of elements simultaneously by γ spectrometry. The γ spectra are taken with high resolution detectors such as germanium semiconductor or NaI(Tl). Radionuclides emitting only β radiation must be measured individually, mostly after preceding chemical separation or dissolving, when possible, the sample in a liquid scintillator [17]. Some example of the application of NAA are reported below.

Landsberger et al. [29] exploited the technique to investigate the amount of Uranium (235 or 238), ^{232}Th and ^{40}K in geological samples. The activity of ^{238}U can be easily determined by the reaction ^{238}U(n,γ)^{239}U with epithermal neutrons. The use of epithermal neutrons allows for better counting statistics at low uranium concentrations because of the large absorption cross section of ^{238}U and the low absorption cross section of other elements like ^{37}Cl and ^{23}Na, which increases the background signal reducing the ability to detect other nuclei. Based on this quantity, one can make an informed extrapolation about the activity of all nuclides in the decay chain by assuming secular equilibrium between ^{238}U and its daughters.

The determination of ^{235}U is more difficult because the (n,γ) product has a half-life of 2.5×10^7 years and it is an alpha emitter. It is possible to access the amount of ^{235}U considering the isotopic ratio between ^{238}U and ^{235}U, and assuming that it is constant in the sample.

To detect ^{40}K one should reveal the 1.46 MeV photopeak of the beta-decay, but because of the long half-life of this element, $t_{\frac{1}{2}} = 1.3 \times 10^9$ years, and because of its low occurrence, it is difficult to determine its activity maintaining fast analysis time and small samples volume. An alternative approach is to determine the concentration of ^{41}K through the ^{41}K(n,γ)^{42}K reaction and then to use the natural isotopic ratios to determine the concentrations of the ^{40}K in the material.

Thorium concentration can be evaluated trough the 312.17 keV photon of its activation product ^{233}Pa.

Samples were irradiated at 1.1 MW TRIGA research reactor at different power and times, according to the type of radionuclide to be detected. The experiment proved the ability of neutron activation analysis to determine the activity and the concentrations of these radionuclides using fast and non invasive methods [29].

Most of the time NAA is performed with thermal thermal neutrons and reactor irradiations with the aim of quantitative analysis. In the case that the (n,γ) cross section is too low or if the macrocomponents are too highly activated by thermal neutrons, high energy neutrons could be a valid alternative for the analysis. Fast Neutron Activation Analysis (FNAA) is thus a complementary technique of NAA that exploits neutrons with energies of the order of $\sim$ MeV. It

is attractive because it can be used to determine the concentrations of the light elements (hydrogen, carbon, nitrogen, and oxygen) which cannot be determined by the conventional thermal NAA. Since these light elements are the primary constituents of explosives or narcotic substances in luggage and cargo containers the FNAA could be an appealing application in this fields [30].
The generation of fast neutrons is accomplished by bombarding thick beryllium target with 3 MeV deuterons, giving rise rise to neutrons varying in energy, from epithermal to $\sim$ 7 MeV with a broad beak at $\sim$ 4 - 5 MeV. Another common technique is to exploit the T(d,n)α reaction which produce neutrons of 14 MeV [31].
Early applications of FNAA were to the determination of oxygen through the 14 MeV neutrons induced reaction ^{16}O(n,p)^{16}N. The detection was done exploiting the γ rays from ^{16}N revealed by germanium detectors. Neutrons derived from deuteron-bombardment of beryllium were used to determine fluorine in a wide range of geochemical samples, using the reaction ^{19}F(n,α)^{16}N. The advantages of using low energy neutrons compared to 14 MeV is that the competing reaction with oxygen is energetically impossible and fluorine can be determined without interferences [31].
Another variant of the technique is the Epithermal Neutron Activation Analysis (ENAA) which exploits the epithermal and the slow regions of the neutron energy spectra (from $\sim$ eV to 1 MeV). ENAA finds its application in the analysis of biological or water (especially sea water) samples which cannot be analysed with thermal sources because of the predominant activation of ^{24}Na. Epithermal fluxes can be obtained from reactor facilities, filtering in adequate way the unwanted component of the spectrum, or exploiting the ^{7}Li(p,n) ^{7}Be reaction. With this technique it was possible to investigate the presence of ^{76}As, ^{82}Br, ^{115}Cd, ^{64}Cu, ^{56}Mn, ^{99}Mo, ^{65}Zn and ^{69m}Zn in liver tissue, minimizing the interference due to the presence of ^{24}Na [32].
A fast variant of the NAA is based on the revelation of prompt gamma rays emitted by samples after the neutron irradiation, making the so-called prompt gamma neutron activation analysis, (PGNAA). An application of this technique was carried out in 2011 by Ma et al., where 50 cm^3 samples containing liquid solutions or powders with Ni, Pb, Cd, Hg, As, Sb, Cr, Mg, Zn, B and Li were measured with GENIE 16 pulsed neutron generator. γ spectroscopy was performed with high purity germanium detector which captured gamma rays 2 ms after the pulse. The neutron pulse duration was set at 100 μs. Pb, Sb, Mg, Zn and Li radiations were too weak for a clear identification, hence study focused mainly on the detection of B, Cd, Cr, Ni, Hg and As. The experiment proved the effectiveness of PGNAA to analyse nuclear waste [33].
Also a rapid and quantitative determination of some elements such as B, Cd, Sm and Gd can be performed exploiting this technique: at the MITR reactor §2.3, samples were irradiated by thermal-diffracted neutron flux of $\sim 10^6$ $\frac{n}{cm^2 s}$ and the prompt-gamma rays revealed with germanium detectors. The experiment proved the ability of the technique to reach sensitivity of ppm for the elements mentioned before [34]. A PGNAA facility is installed also at the CARR reactor, in China, where two beam guides drive neutrons on the samples. The thermal neutron flux at the sample position is expected to be about $10^9 \frac{n}{cm^2 s}$ [35].

1.2.5 Boron neutron capture therapy

Boron neutron capture therapy (BNCT) [36] is an experimental hadrontherapy treatment based on the administration of a drug able to concentrate an amount of ^{10}B in tumour cells, followed by low energy neutron irradiation. The neutron beams at the depth where the tumour is seated should be thermal, so that thermal neutron capture on ^{10}B generates two high LET [1] particles, i.e α and ^{7}Li, that release all their energy in a range comparable to the cell diameter. In this way, the charged particles cause irreparable damage to the cell where the reaction takes place, without affecting the surrounding healthy cells. The reaction implicated in this therapy is the $^{10}B(n,\alpha)^{7}Li$ reaction, and its cross section at the reference thermal energy (0.025 eV) is about 3800 barns. The reaction can occur through the production of ^{7}Li either in the ground state, (6 %), or in the excited state which de-excites by emitting a gamma ray of 480 keV (94%). Considering the Q-value of the reaction, that is 2.79 MeV, the α particle and the Li are generated with an initial kinetic energy of 1.47 MeV and 0.84 MeV respectively, and they move in the tissue with a range of 8 μm and 4 μm. Considering that the average dimensions of the cell is about $\sim$ 10μm, all the kinetic energy is deposited in the cell loaded with the boron isotope. A schematic view of the process is shown in figure 1.5. The main difficulty is in the

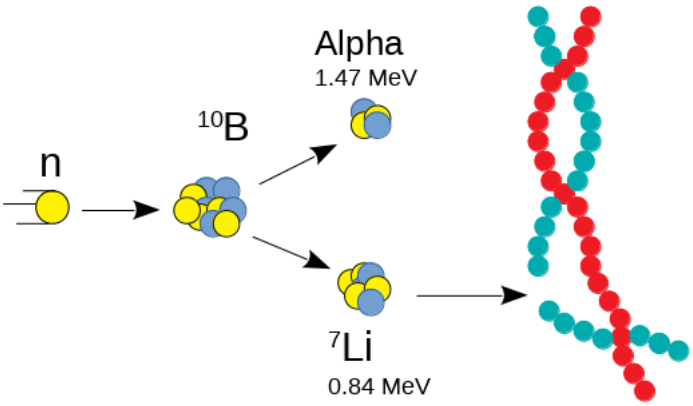

Figure 1.5: Schematic representation of the physics process at the basis of BNCT.

development of pharmaceuticals for carrying boron to the tumoural cells, minimizing the boron concentration in the healthy cells and in the blood. The ratio of the tumour/brain, tumour/blood concentration should be higher than 3-4:1 for the effectiveness of therapy. The most extensively employed boron containing drugs are L-boronphenylalanine (BPA) and sodium mercaptoundecahydrocloso-dodecaborate (BSH) because they are characterized by a low toxicity, a

[1] When a charged particle passes through the matter, it goes through electromagnetic collisions that excite and ionized the atoms of the material. The term LET means "Linear Energy Transfer " and it the physical dimension related to this phenomenon: it is the amount of energy that an ionizing particle transfers to the material traversed per unit distance [37].

longer persistence in the tumour, higher tumour/brain and tumour/blood concentration.
This type of therapy should be useful for that kind of tumours where surgery operation or conventional radiotherapies cannot be performed, such as the glioblastoma multiforme (brain tumours) or the pigmented melanoma. The first disease propagates into the brain healthy tissue along multiple directions and therefore is very difficult to treat with surgery or conventional radiotherapy. The latter is very aggressive skin tumour that generates metastases which cannot be diagnosed and removed surgically, hence BNCT represent the ideal treatment which could be effective for eradicating the satellite metastases. 18 patients were treated in japan and showed local control of the primary tumour and of the metastatic nodules, and some of them did not suffer from any recurrence up to 4 years from BNCT.
In order to perform this treatment, a thermal or epithermal neutron fields is required and, up to now, all treatments have used a field generated by research reactors. However, there are many studies on developing new type of neutron sources, more compact, cheaper, and less diffcult to operate: these type of sources are based on the acceleration of protons on targets, typically made of beryllium or lithium[21, 38].

Chapter 2

Production of neutron beams: from conventional to innovative sources

2.1 Introduction

Neutron beam can be produced from a variety of nuclear reactions. Since the particle is not affected by the Coulomb interactions, it is difficult to select the direction and the energy of the beam, but it is possible to reduce the energy of an high-energy neutron flux through collisions with atoms of various materials. The classification of neutrons beam according to energy is given in table 2.1: The aim of this chapter is to provide a description of the main approaches

	Energy
Thermal	$\sim$0.025 eV
Epithermal	$<$0.5 eV
Slow	$\sim$1KeV
Fast	$>$ 1 MeV

Table 2.1: Classifications of neutron fluxes according to their energy. From [18].

for the production of neutrons, focusing the attention on the yields and on the energies range of neutron emitted. Particular attention is given to the possibility of generating neutrons via (p,n) reactions with low energy ($\sim$ MeV) protons, accelerated by conventional accelerators or exploiting the innovative laser-driven method.

2.2 Natural sources

The reaction ^{4}He + ^{9}Be $\rightarrow$ ^{12}C + n (Q = 5.7 MeV) can be used to produce neutrons. Therefore, mixing together long-lived α-emitting material, such as ^{226}Ra (1602 y), and ^{9}Be there will be a constant rate of neutron production.

The emission will be isotropic, and the most probable neutron energy is about 5 MeV with a production rate of $\sim 10^7$ $\frac{n}{s}$ for each Ci of ^{226}Ra. Because of high γ-emission of ^{226}Ra and its daughter, sometimes it preferable to use ^{210}Po (138 d), ^{214}Am (458 y) or ^{238}Pu (86 y) that produce 3×10^6 $\frac{n}{s}$ for Ci of α activity [18].
A common source of neutrons is the spontaneous fission of isotope ^{252}Cf (2.65 y) which produces about 4 neutrons per fission. The production rate is 4.3×10^9 $\frac{n}{s}$ per Ci of ^{252}Cf, and the neutron energy distribution presents a continuous distribution with average energy of 1-3 MeV. The fission occurs only about 3% of the decays, α decay accounts for the rest [18].
This isotope is sometimes used for neutron activation analysis technique when high sensitivity is not needed.

Those type of sources (spontaneous fission and α-beryllium sources) produce a modest amount of neutrons and do not imply high costs, therefore are ideal at laboratory scale. Anyway, it is necessary to handle with radioactive materials and from the radioprotection point of view it is required a continuous control and shielding. Moreover it is not possible to control the intensity of the neutron fluxes emitted, the neutron energy and the angular distribution. If greater intensity or particular angular directions of the fluxes (like in the case of BNCT) are needed, other approach must be pursued.

2.3 Research Fission Reactors

The neutron flux near the core of fission reactors can reach values typically of the order of 10^{14} $\frac{n}{cm^2 s}$. The neutron energy distribution from a moderated research reactor shows fast, slowing-down and thermal component.
To moderate and attenuate this spectrum common moderators like light or heavy water and nuclear graphite are used. Up to few MeV, hydrogen presents higher elastic cross section compared with deuterium so light water is more effective in slowing down neutrons, but at the same time the flux is impoverished and gamma rays are emitted because of higher values of capture cross sections. Nuclear graphite is high purity graphite where the concentration of impurities such us ^{10}B and Gd are minimized.
In the case that an epithermal spectrum is needed (0.5 eV – 10 keV), aluminium, fluorine and oxygen play a fundamental role for filtering and tailoring the flux because of their resonances of elastic-scattering cross section in the range 5 Kev – 1 MeV.
If the thermal component of spectrum must be attenuated, classical absorbing materials like cadmium, ^{10}B, or ^{6}Li are employed taking into account the fact that cadmium and boron generate prompt gamma rays. Common attenuator to shield photons are lead or bismuth.

Example of research reactors implicated in neutron production

At the Massachusetts Institute of Technology (MIT), the research reactor MITR is designed specifically for neutron capture therapy: a large area of thermal neutron flux impinges upon fissionable materials, the converter, generating a fission neutron spectrum that is moderated and filtered to produce epithermal neutron

beam of high intensity and purity. The converter is composed by ten spent MITR fuel elements that operate at 83 KW of fission power with the MITR at 5 MW, and that produce a fission neutron source 60 cm high and 74 cm wide in the thermal column of MITR. Increasing the converter power up to 250 KW the flux will increase by a factor of three.
The beam line, starting at the converter, is equipped with filter made by 81 cm-thick aluminium slab, flanked with 13 cm-thick PTFE and 0.5 cm-thick cadmium to moderate and to filter the neutron beam.
A 6 cm thick lead shield is used to reduce photon contamination in the beam and a lead collimator with 15 cm thick walls directs the epithermal neutron beam to enter the medical irradiation room. The epithermal beam in this point has an intensity of $1.2 \times 10^9 \frac{n}{cm^2 s}$ [39].
In Italy there is a research reactor called TRIGA, placed in Pavia. It is a light water pool reactor, and it is an intrinsically safe reactor, i.e. it posses negative reactivity coefficient against temperature. This behaviour is due to its fuel/-moderator rods composed by ZrH2/U: ZrH2 behaves as an harmonic oscillator, and if the temperature increases, the number of excited states increases with the probability that neutrons are up-scattered and gain in energy. The fuel rods are subcritical and the water pool is fundamental for maintaining the system critical. In this reactor in 1996 an epithermal neutron facility was built, employing a neutron moderator called "FLUENTAL", a compound composed by aluminium fluoride (69%), aluminium (30%), and lithium fluoride (1%). Bismuth layer was chosen in order to reduce the gamma component.
In China, until 2006 the only neutron source available for neutron scattering experiment was the the 15 MW Heavy Water Research Reactor (HWRR) at China Institute of Atomic Energy (CIAE). In 2007, after fifty years of service the reactor was taken out of service and the China Advanced Research Reactor (CARR) has taken over this role [40, 41]. CARR was built for the research in the fields of neutron scattering, radioisotopes production and neutron activation analysis, and it is is one of the most powerful research reactors in the world [35]. It is a 60 MW tank-in-pool reactor using heavy water as reflector, and it is designed to reach an undisturbed neutron flux in the center of the active area of $1 \times 10^{15} \frac{n}{cm^2 s}$. Seven horizontal beam tubes are used for thermal neutron-scattering experiments, and three kind of neutron channels are allocated to perform NAA studies. The neutron flux in these channels at the samples position are appoximately $3 \times 10^{14} \frac{n}{cm^2 s}$, $10^9 \frac{n}{cm^2 s}$ and $10^9 \frac{n}{cm^2 s}$ [35].

In conclusion, reactors are continuous neutron sources that can deliver a very high time-averaged flux, and this is very appealing for the neutron activation analysis, neutron capture therapy, or material analysis. The spectrum of neutron energies in nuclear reactors is broad and it varies with the type of reactor and with the positions in the same reactor.
On the other hand, using a reactor as neutron source presents several downsides: first of all the costs of building it and make it work are very high. Also the costs of decommissioning should be taken into account. Furthermore there are radioprotection issues, related to the operation of reactor, but also to the management of nuclear waste. There are also problems related to the nuclear proliferation.

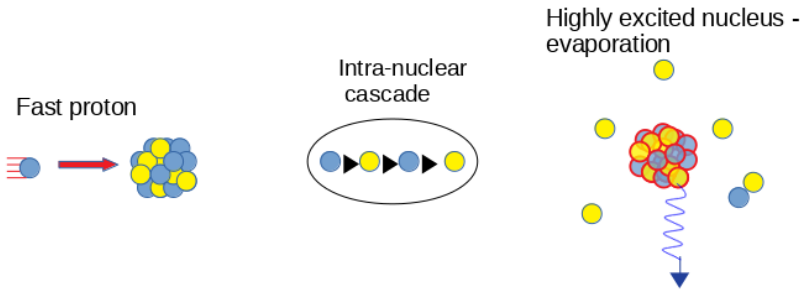

Figure 2.1: Spallation Reaction

2.4 Spallation Reactions

For kinetic energy above 100 MeV in laboratory references system, protons impacting on a target containing heavy nuclei cause the release of large amount of neutrons. In particular, when a proton with high kinetic energy ($\sim$ GeV) hits the nucleus, from 20 to 30 neutrons are "spalled" or thrown off, leading in a very high yield of reaction. The interaction of high energy nucleon with a nucleus consists in two stages: in the first one, the shortest stage, the incident nucleon initiates a set of nucleon–nucleon collisions in which high-energy particles are emitted. In the second stage, the highly excited nucleus loses its residual energy by an evaporation-like process, emitting low-energy particles. The yield is approximately a linear function of the incident particle energy, but it also depends on the target material [42]. The spallation process is schematically shown in figure 2.1.

Spallation facilities in the world

In Europe the *European Spallation Source* (ESS) is under construction: a linear accelerator will deliver 2.0 GeV, 62.5 mA protons beam to a spallation target to generate fast neutrons. Supercritical hydrogen, at 17 K and 1.5 MPa, will circulate as moderator around the target slowing down the neutrons. Since latters will deposit a large amount of energy in the hydrogen, this must be cooled to remain at its operating temperature. This will be done via a heat exchanger that transfers the heat to a gaseous Helium circuit operating between 15 K and 20 K [43].
The shielding of the target comprises about 6000 tons of steel and the estimated neutron brightness will be about $10^{18}\frac{n}{s}$ [44].
The construction began in 2014 and the initial operations are planned for 2019.

In the U.S.A, at Oak Ridge National Laboratory the *Spallation Neutron Source* (SNS) facility was built. The SNS accelerator consists in a 1 GeV linear accelerator and an accumulator ring providing 1.4 MW of protons beam power, in microsecond-long beam pulses, to a liquid mercury target for neutron pro-

duction. The neutron brightness is about 10^{17} $\frac{n}{s}$.
It was predicted that SNS could also provide the world's most intense pulsed source of neutrinos. The proton beam in mercury target produces π^- mesons that decaying in mercury generate neutrinos. The time structure of the beam is particularly advantageous because all neutrinos will be produced within several microseconds of the 60 Hz proton beam pulses, allowing an easier discrimination from the background component due to cosmic rays [45].

In Lanzhou, China, an experiment was performed with 250 MeV protons beam of 10 mA colliding on cylindrical target made by lead surrounded by a water bath. As diagnostic, an air ionization chamber was placed in front of the target to monitor the protons beam current. Before the ionization chamber, an high-purity Al-foil of 300μm thickness was placed to estimate the total number of protons via $^{27}\mathrm{A}l(p, 3p\ n)^{24}\mathrm{Na}$ activation analysis reaction.
The neutrons emitted from target were moderated in the water and measured by the activity induced in an array of Au activation foils covered with cadmium. High purity germanium detectors (HPGe) were used to determine the gamma activity of ^{198}Au. The total yield of reaction deduced was $1,91 \pm 0.16$ neutron for every proton [4]. The experimental facility is shown in figure 2.2

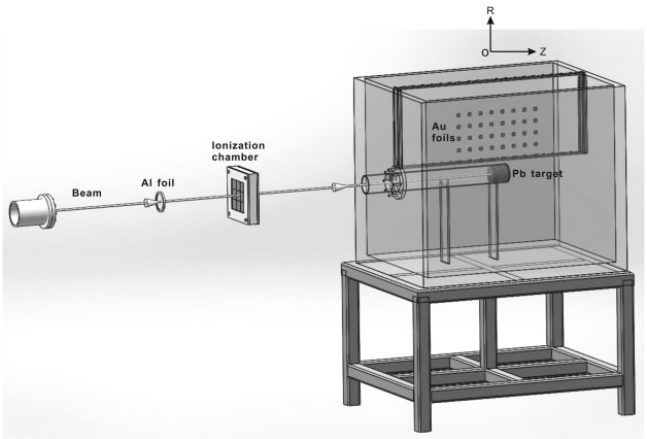

Figure 2.2: Spallation facility scheme in ref. [4]

Still in China, a study where 250 MeV protons beam impinges on a tungsten cylindrical target made of small randomly oriented grains was carried out. To avoid problems related to brittleness of material, an alloy of 93% W, 5% Ni, 2% Fe was used.
The thermal neutron flux in water was measured with the activation of gold foil, similarly to the previous experiment with lead. Most neutrons have energy of several MeV, as well as a small part of high-energy neutrons above 20 MeV. In water most of them are thermalized. Almost all neutrons disappear in water because of capture processes. The estimated neutron flux distribution does not differ too much compared with the one produced by using lead as target: the estimated yield of reaction was 2.02 ± 0.15 neutron for every proton. The only difference is that tungsten is more dense than lead, so the protons stopping

power is higher and along the axis of cylinder the flux is lower [46].

In Japan, at the National Cancer Center, proton irradiation experiments were conducted using the cyclotron accelerator §2.5. In particular, protons ranging between 150 and 235 MeV at 1 nA of intensity were injected into a tungsten target, whose thickness varied according to the proton energy. The high energy neutrons generated by spallation reaction were detected using the $^{209}\mathrm{Bi}(\mathrm{n},\mathrm{xn})^{(210-\mathrm{x})}\mathrm{Bi}$ threshold reaction, ranging between 20 and 90 MeV. The experimental results were obtained by revealing the gamma rays emitted by the reactions, and confirmed the presence of high energy neutrons up to 90 MeV [47].
In conclusion spallation sources can produce high neutron fluxes of $\sim 10^{17} \frac{n}{cm^2 s}$ and high energy neutrons that are useful for studies in material science or fundamental physics. This type of fluxes could also be interesting for applications like boron neutron capture therapy. This reaction is the most efficient to produce neutrons, but it is also the most costly. These facilities have an huge dimensions, and a great mechanical complexity. It is also necessary to deal with radioprotection issues, designing the shielding.

2.5 Low energy charged particles induced reactions

To reduce the cost and the radioprotection issues related to the build and the operations of nuclear reactors or spallation facilities, another approach to produce neutrons is to accelerate protons, deuterium or light ions against targets made by light elements. Choosing in opportune manner the target nuclei, the main reactions exploited for these purpose are the (p,n), (p,p',n) or (d,n) reactions. If compared to the spallation sources, this way to produce neutrons requires much less energetic projectiles ($\sim$ MeV or tens or MeV). Such reactions produce several orders of magnitude less neutrons than spallation reactions, but this fact is partly compensated if high-intensity beams are used. The energies of neutrons produced with this method are of the order of hundred KeV or few MeV according to the target or to the protons beam, and are appealing for many industrial applications such as the analysis of material, neutron activation analysis and the boron neutron capture therapy.
The choice of the converter is based on the values of the proton-neutron cross-section for the energy range of incident protons. Considering incident energies of the order of $\sim$ MeV, from literature, the two main material used in this field are beryllium and lithium.

2.5.1 Materials

Beryllium

Beryllium is a very light metal with density of 1.85 $\frac{g}{cm^3}$ and relative high melting point of 1560 K, with as a close-packed hexagonal crystal structure. Thanks to the high melting point there aren't problem related to the melt of material during the irradiation. It should be noticed that it is toxic and requires an

adequate dust control.
From the isotopic point of view the only stable isotope of beryllium is ^9Be, but in nature there are also present traces of ^{10}Be. Other isotopes have such short half-lives that none are primordial and their abundance is very low.
The high (p,n) cross-section (hundreds of mbarns at proton energies of $\sim$ MeV) and the good mechanical and thermal properties of the material that ease the heat removal, make beryllium important high-intensity source of neutrons for many applications.
The first studies of the proton-capture cross section of this material were made by Marion et al. in 1956 [6]. In particular, the ^{9}Be(p,n)^{9}B (Q = 1.850 MeV) reaction that proceeds through the formation of compound nucleus ^{10}B was investigated. The study foucused the attention on the resonances at 2.56 MeV and 4.70 MeV. Excitation curves for the ^{9}Be(p,n)^{9}B reaction were measured for bombarding energies from 2 MeV to 5 MeV at 0° and 90° (direction of incident beam), and the resonances were observed at both angles with an isotropic distribution, according to the compound nucleus theory [6]. Furthermore, since ^{9}Be has the lowest neutron binding energy of any stable isotope (1.67 MeV), three-body breakup reaction ^{9}Be(p,p' n)^{8}Be can take place under proton bombardment at incident energy of 1.85 MeV, below the ^{9}Be(p,n)^{9}B threshold at 2.059 MeV. The three-body breakup cross section becomes appreciable by 3 MeV, and it shows a broad resonance near a proton energy of 3.5 MeV becoming comparable to the compound nucleus cross section, thus giving a substantial contribution to the total neutron yield. The angular distribution of three-body neutrons seems to be foreword peaked [48]. Figure 2.3 shows the total experimental cross section, which takes into account the two reactions ^{9}Be(p,n)^{9}B and ^{9}Be(p,p' n)^{8}Be. All these considerations will be recalled in the next paragraph §2.5.3 to explain the experimental studies of neutron production through beryllium converters.

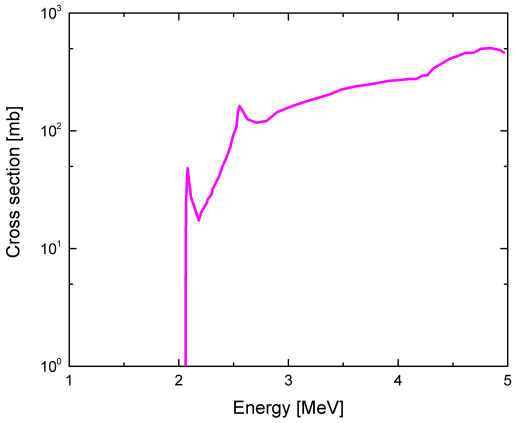

Figure 2.3: Total neutron production cross section of beryllium. From [5, 6]
,

Lithium

Lithium is a valid candidate as neutron converter. It is the lighter metal, with density equal to 0.535 $\frac{g}{cm^3}$ in the solid form and it has a low fusion point of 453.69 K. Because of this low melting point, it was predicted that a solid target could run up to 10 mA proton beam before melting. As alternative, to overcome issues related to the melt, liquid lithium is used. Anyway, in both cases, it should be noticed that this material is difficult to handle, since it is classically reactive with air and water. In particular, the reaction of lithium with liquid water is less vigorous than the reactions of other alkali metals, but occurs easily if the metal is heated. The reaction that occurs is $2Li + 2H_2O \rightarrow 2LiOH + H_2$ [49].
The $^7Li(p,n)$ reaction produces an high neutron yield and requires a relatively lower proton energy compared to the beryllium ones. The threshold of reaction is ∼1.88 MeV and the cross-section presents an high resonance at 2.25 MeV, where it reaches values of ∼ 580 mbarn. The shape of the $^7Li(p,n)^7Be$ cross section is known from the works of Macklin et al in 1958 [50] and it is shown in figure 2.4.

The peak at 2.25 MeV could be exploited to generated a large amount of

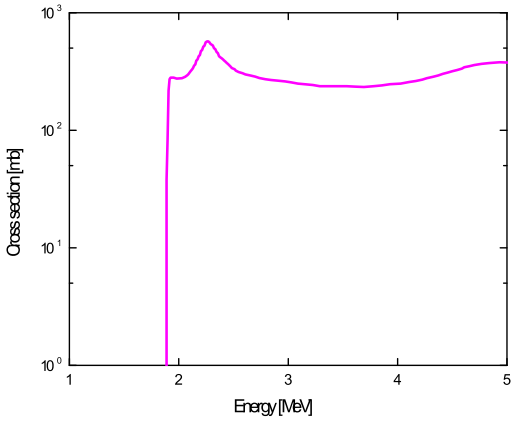

Figure 2.4: The $^7Li(p,n)^7Be$ cross-section

neutrons whose energy and spectrum are appealing for techniques like boron neutron capture therapy.

2.5.2 Conventional proton accelerators

In order to produce neutrons with low energy (i.e ∼ MeV) charged particles induced reactions, an accelerator system which accelerates and directs the particles against the target nuclei is required. The two most popular accelerators to achieve these energies are the "Van-de Graaff" accelerator and the "Cyclotron". Common feature for every ions accelerator system are:

- the ion source which originates the beam of ions or electrons that is to be accelerated. In this basic operation a gas is ionized through an electric discharge and the positively charged ions are extracted by acceleration toward a negative electrode at a potential of the order of 10 kV. For some applications it is desired to have a beam of negative ions, and this is made letting a beam of positive ions pass through a neutral gas characterized by low ionization energy, for example alkali atoms. Even if only 1% of positive ions becomes negative, it is possible to select these latter using magnetic fields;

- the beam transport (or beam optics) is a system that consists of a number of electric or magnetic devices that focus the beam or deflect it along desired direction. For this purpose are used bending magnets, that change the direction of the accelerated beam according to the particles momentum.

Electrostatic accelerators

The simplest way to accelerate a charged particle is to let it move through a constant potential difference. If the particle charge is q, it will acquire a kinetic energy equal to qV. In this case we speak about "Electrostatic accelerator". The largest potential difference that can be maintained under acceleration conditions is about 10^7 V, and thus ions will acquire an energy of the order of 10 MeV per unit of charge.

The most common type of electrostatic accelerator in use today is based on the Van de Graaff generator showed in figure 2.5. An insulating belt, usually made by rubber or silk, is hold between two pulleys and charged by induction through a series of metallic tips connected to a generator of continuous voltage. The charge is transported in a spheric conductor, called "high voltage terminal", where a second series of metallic tips transfers it on the surface of the sphere. The ion sources are placed inside this terminal and ions fall to the ground through the potential difference. A limit in charging the high voltage terminal is imposed by the electrical breakdown (sparking) of the insulating column that supports the conductor or the surrounding atmosphere. To reduce the occurrence of this phenomenon the generator is usually enclosed in a pressure tank containing ten or twenty atmospheres of insulating gas such as SF_6, which inhibits breakdown. This type of accelerator can reach output current of μA or mA, useful for nuclear reaction experiments.

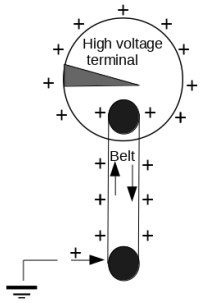

Figure 2.5: Van de Graaff accelerator scheme

A prototype of this accelerator is the *Tandem* Van de Graaf accelerator, in which a negative ions beam is accelerated from the ground potential toward the high

voltage terminal. These beam enters a foil or gas stripper which removes $n + 1$ electrons, resulting in a positive ions[18]. A scheme of the Tandem accelerator is displayed in figure 2.6.

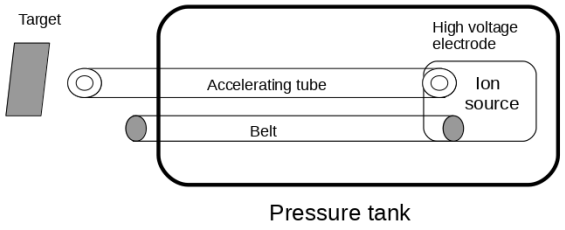

Figure 2.6: Van de Graaff horizontal Tandem accelerator scheme.

Cyclotron accelerators

An alternative to the electrostatic accelerators are the circular devices, in which particles make many cycles through the device receiving a small kinetic energy increment in each orbit, until they reach the MeV range. In this case we talk about cyclotron. The beam is bent into a circular path by a magnetic field, and the particles orbit inside two metallic chambers called *dees*. Inside the dees the particles don't feel any electric field, but follow a circular path under the influence of the magnetic field. In the gap between the dees, the particles feel an accelerating voltage gaining small energy for each cycle. The critical point is that the electric filed in the gap must alternate in exact synchronization with the passage of particles, allowing the acceleration. This must be done considering that the particles bend at larger radii and at higher speed each time. The frequency of the voltage must be equal to the gyrofrequency of particles:

$$\nu = \frac{qB}{2\pi m} \tag{2.1}$$

Generally, frequency is in the range of 10 MHz and magnetic fields near 1 T. The greatest velocity will occur at radius R:

$$v_{max} = \frac{qBR}{m}. \tag{2.2}$$

In order to extract ions from the machine at a specific location, deflection fields, electric or magnetic, must be applied, and they must bend the beam in desired direction.
A serious difficulty comes from the relativistic behaviour of the accelerated particles, that leads to a reduction in the gyrofrequency of the beam because of the relativistic increase in the ion mass. Synchronization can be preserved only if the average bending magnetic field increases with radius, but this will cause vertical defocusing. One way to provide additional focusing is to introduce azimuthal variations in the bending field, creating high and low field sector. Such type

of cyclotron is called azimuthally varying field cyclotron (AVF). AVF cyclotron can deliver continuous beam of the order of $\sim 100\ \mu$A and produce protons with energy of tens or hundreds of MeV [18].

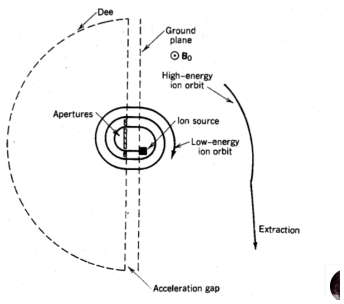

Figure 2.7: Cyclotron scheme

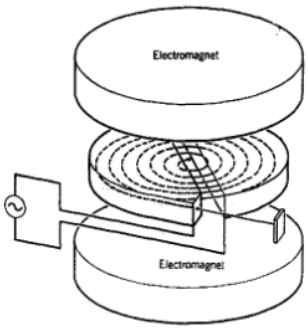

Figure 2.8: Cyclotron layout

2.5.3 Experimental studies of neutrons produced by low energy protons impinging on a target

In this paragraph the main experimental studies in which protons of some MeV impinge on beryllium or lithium converters are reported, focusing the attention on the neutron yields, features of the energy spectra and the angular distributions.

Beryllium

At the *Ohio University Accelerator Laboratory* (OUAL) Howard et al. measured the neutron energy spectra of the ^{9}Be(p,n) reaction using proton beams of different energies (2001). The protons were accelerated using a tandem Van De Graaff accelerator that produces bunched pulses of < 1 ns width with a frequency of $\frac{5}{16}$ MHz. The experiments were carried out using 5.0, 4.0, 3.7, 3.4 and 3.0 MeV protons impinging on 2.5 cm square and 0.25 or 0.5 mm thick targets, 99.9% pure in their beryllium content. The thickness of the target was enough to stop 4 MeV protons [5].
The evaluation of neutron spectra at energies below $\sim$500 KeV and up to 2.3 MeV requires the use of detectors that can discriminate the interaction of low and high energy neutrons: four lithium-loaded glass scintillators were used because of their fast response time and their sensitivity. These detectors contained 6.6% weight fraction of lithium, enriched to 95% of ^{6}Li*(γ).
The neutron spectra were measured and are reported in figure 2.9.
To explain the behaviour of this spectrum one should take into account the various type of nuclear reactions that occur: the ^{9}Be(p,n)^{9}B reaction occurs through the formation of compound nucleus ^{10}B. Since the first excited state for ^{9}B is at 4.64 MeV, it cannot be excited by all the energies of proton beam in use but 5.0 MeV, thus only ground-state transitions (p,n$_0$) will contribute to the compound-nucleus channel. We label this reaction as n$_0$ neutron group. The

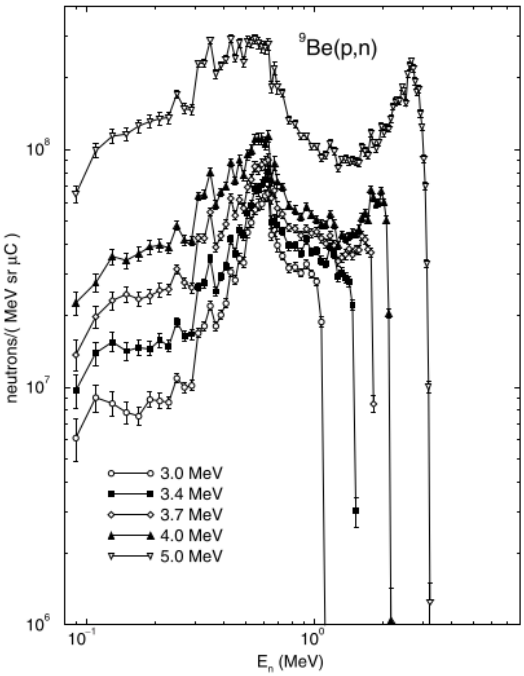

Figure 2.9: Howard et al. "The ^{9}Be(p,n) neutron spectra at 0 deg for five enegies" [5]

three-body break up gives rise to a continuous distribution of neutrons. Other nuclear reactions that actually produce neutrons are ^{9}Be(p,p')^{9}Be* $\rightarrow \alpha + {}^5$He $\rightarrow$ n + α or ^{9}Be(p,α)^{6}Li* $\rightarrow \alpha$ + n + p, ^{9}Be(p,α)^{6}Li* $\rightarrow {}^5$Li + n, but are less important.

It is reasonable to consider beam of uniform intensity passing through the target, since only $\sim$ 16 in 100000 protons actually generate a neutron. Going forward through the target, protons lose their energy with electromagnetic collisions, ionizing and exciting the atoms of material, and producing fewer neutrons because to the lower values of cross sections. As the proton beam enters the beryllium target, with energy of 4 MeV for example, it produces neutrons with energy E(n$_0$)$\sim$ 2.2 MeV through the compound nucleus reaction. Also three-body breakup contribute to neutrons production. Progressing thorough the target, protons slow down and the neutrons produced will have a slightly lower energy. The process continues until the protons reach the resonance at 2.56 MeV. Here the production of neutrons increases, but their energy will be lower. Neutrons produced with energies above 1 MeV are believed to be due primarily to the ^{9}Be(p,n$_0$)^{9}B reaction trough the compound nucleus ^{10}B. At 3.0 MeV of incident proton energy, the production of neutrons is dominated by sequential three-body breakup that leads to a broad peak around 600 KeV in the neutron spectrum. The neutrons production near 500 KeV may also have some contribution from the decay of second excited state of ^{9}Be excited via ^{9}Be(p,p'n) reaction.

The total neutron yield of reaction can be determined integrating over measured

energy range and solid angle, and the obtained values were $9.61 \pm 0.48 \times 10^{11}$ $\frac{neutrons}{mC}$ and $1.48 \pm 0.07 \times 10^{12}$ $\frac{neutrons}{mC}$ for proton beam energy of 3.7 MeV and 4.0 MeV respectively.
Considering the angular distribution, shown in figure 2.10, the total yield is fairly flat, fact that is in accord with the theoretical theory of compound nucleus reactions.

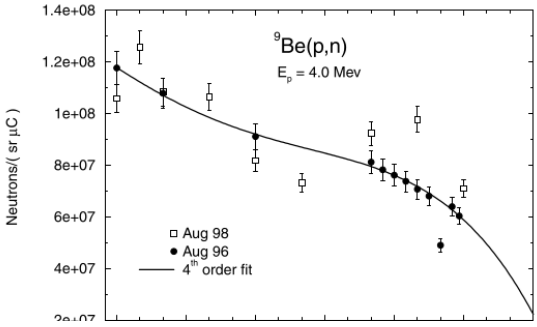

Figure 2.10: Howard et al. "The experimental 4.0 MeV angular distribution" [5]

In 2011, at the Legnaro Laboratories (LNL) of the Italian National Institute for Nuclear Physics research, neutron spectra from Be(p,n) reaction were measured [7]. A systematic characterization of the neutron energy distribution was carried out at different emission angles between 0° and 120°, with 5 MeV protons beam accelerated by a Van de Graaff system. The obtained spectrum at 0°, the total yield and the angular distribution showed a very good agreement with the ones obtained by Howard et al. [5]. It is important to underline that the angular distribution, shown in figure 2.11, presents its maximum at 0°, then it decreases reaching the minimum value at 60° and finally increase again up 120°. This behaviour is due to the presence of three-body breakup neutrons.
One of the first investigations about neutrons spectra from beryllium targets was performed by Guzek et al. in 1998 [8]. In the experiment, beam of protons of different energies were delivered by a Van de Graaf accelerator on thick beryllium target. The energies chosen were of 2.57, 3.00 and 4 MeV. The neutron spectra obtained at 0° are shown in figure 2.12.

The experiments reported demonstrate that thick beryllium targets are valid candidates as proton-neutron converter. With protons delivered by common accelerators, the yield can reach values of $\sim 10^{12}$ $\frac{n}{s}$ and the spectrum could be useful in different applications, in particular the BNCT.
However, one of biggest issue of this material is the embrittlement caused by proton injection, that causes the target destruction in short time, typically several hours. This phenomenon is called "blistering", and it is due to the accumulation

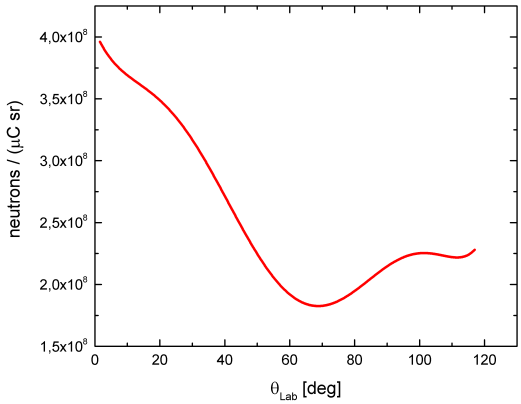

Figure 2.11: Neutrons angular distribution for incident beam of 5 MeV. From Agosteo et al. [7]

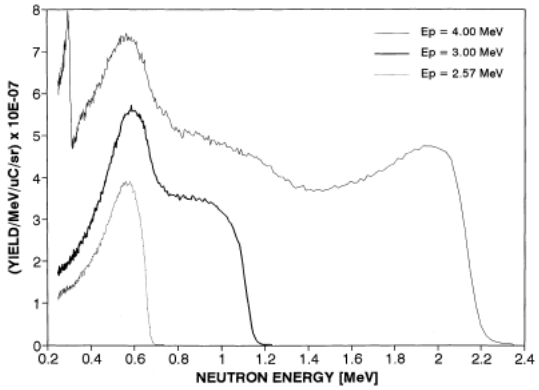

Figure 2.12: Neutron spectra with from beryllium target bombarded with different proton energy, from [8].

of protons because of the Bragg peak in a layer beneath the surface, resulting in a formation of hydrogen between the grains. The presssure of cooling water and the degradation of mechanical properties due to this fact will inevitably lead to the break of mateiral. To solve this problem it is necessary to set a target thickness sufficiently reduced to slow down the proton beam until 2 MeV, since the threshold of ^{9}Be(p,n) is 2 MeV, and to let the protons exit from the rear side of target. Furthermore, in order to give mechanical strength to the target, it was proposed to use a backing material with high hydrogen diffusion coefficient. The backing material must be chosen considering the issues related to the heat removal from the target and related to the activation by neutrons. Of course it is preferable that the target does not mantain high level of radioactivity for a long time. Considering these factors, vanadium is a good candidate since the

activation product ^{52}V has a very short half life of 3.7 min. Also niobium, tantalum or palladium have relative high diffusion coefficient and can be used as backing materials [51].

Lithium

In 1997 Yu et al. [20] measured the neutron yields from ^{7}Li(p,n)^{7}Li reactions (thick target) with incident proton energies near threshold. The neutron spectra, the yields and the angular distributions obtained at these energies are appealing for the BNCT technique. For proton incident energy of 1.885 MeV and current 10 mA the obtained yield was of 3.08×10^{12} $\frac{n}{Csr}$, the maximum angle of the neutron distribution is less than 20° and the maximum neutron energy is about ∼52 KeV. For incident proton energy of 1.9 MeV, the total yield was of 5.71×10^{12} $\frac{n}{Csr}$, the maximum neutron energy of ∼70 KeV and the angular distribution still foreword peaked. For incident energies greater than 1.9 MeV, neutron yields are greater and the neutron angular distributions are wider resulting less suitable for BNCT.
Bayanov et al. studied the neutron production from a solid lithium targets of different thickness. The main requirement for target cooling is to mantain the temperature below 182°C. Hence one of critical issues is the target design: it should have good mechanical properties to resist the coolant pressure and it should be a good heat conductor in order to remove heat during the irradiation. Considering these purposes, a tungsten disk 10 cm in diameter and 3 mm thick was designed with spiral cooling channels and pressed to a titanium body. A thin lithium layer with thickness ∼ 100 μm was applied on the proton beam side through evaporation processes. The use of a thicker layer results in an increased sublimation of lithium, which is dangerous because of the propagation of the radioactive beryllium isotope produced in the reactions [52].
Water was used as coolant. Also liquid metal heat carrier (gallium) was proposed instead of water, as there is no 100°C limit on temperature of a surface to be cooled, and there is no danger in case of coolant leakage into vacuum volume, but there are problems related to the chemical reactivity that leads to the destruction of target [53].

The total neutron yield was valued by measuring the activity of target after irradiation, since each neutron is accompanied by the occurrence of ^{7}Be radioactive nuclei, which decays emitting 477 KeV γ ray. NaI scintillator detectors, properly shielded by lead to remove electromagnetic noise, were used to reveal this radiation. These targets were irradiated with ∼140 μA and the average estimated neutron yield was of 2.6×10^{9} $\frac{n}{s}$ [21].
It is reasonable to believe that the presence of coolant and the target support will cause a perturbation of flux.

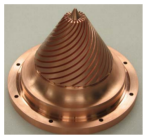

Figure 2.13: Copper comical backing.

Other type of geometries and backing material can be thought in order to maximize the mechanical properties and the heat exchange. Conical target prototype was proposed by Willis et al., and it was designed to held the lithium temperature below 150°C with a water flow rate near 80 $\frac{kg}{min}$. Helical channels let the coolant flow through the copper backing material. In order to solve issues re-

lated by blistering, a $\sim$10μm substrate of electroplated palladium is interposed between the lithium and the heat exchanger thickness to encompass the Bragg peak of the beam and to dissipate hydrogen either by storage or diffusion [54]. A prototype was built and it is shown in figure 2.13.
The use of solid targets, i.e metallic lithium or compounds such as lithium fluoride, limits the proton beam intensities at 100 μA. Blistering of the target backing also sets a limit to high beam-power irradiation of solid lithium targets. There are also issues related the formation of oxides on the surface due to the high reactivity of the material. To overcome all these problematics, liquid target was proposed.

Halfon et al. demonstrated the possibility to use liquid lithium target (LiLiT) to constitute an intense source of epithermal neutrons: they forced a film of liquid lithium at $\sim$ 200 °C to flow at high velocity (7 $\frac{m}{s}$) onto a concave-curvature stainless-steel wall. A nozzle determines the film width and thickness (18 mm and 1.5 mm). The target was bombarded by high intensity proton beam impinging directly on Li-vacuum interface, with an energy near the ^{7}Li(p,n) reaction threshold (1.88MeV). The lithium was recirculated using a pump and properly cooled with a secondary oil loop. One of major concern dealing with liquid lithium is safety, because if exposed to humid air can cause explosions and radioactive fires contaminated with ^{7}Be. Hence a stainless steel enclosure was built around the target, and an air drier was used to impose the level of humidity $< 5\%$.

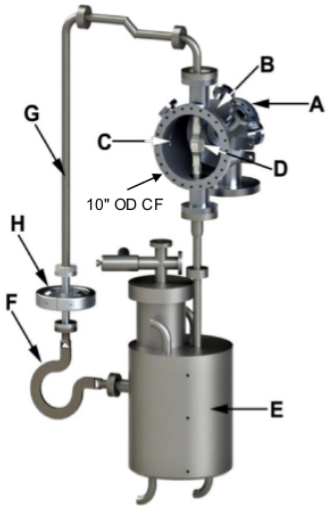

Figure 2.14: Halfon et al. Schematic drawing of the LiLiT assembly viewed from the neutron exit port: (A) proton beam inlet port, (B) target chamber (cross section seen in Fig. 1), (C) neutron port (shown open); (D) lithium nozzle, (E) lithium containment tank (including heat exchanger and 7 Be cold trap), (F) electromagnetic (EM) pump (only the circulation loop is shown), (G) loop line, (H) electromagnetic flowmeter.

LiLiT flowing at 2.4 $\frac{m}{s}$ was irradiated by an 1.940 MeV proton beam with an intensity raising in time. The average current on target was of 1.2 mA. The temperature in the chamber was constantly monitored, giving stable values between 220°C and 240°C. For an accurate neutron flux evaluation, a pair of Au activation foils were positioned in a secondary vacuum chamber downstream the LiLiT and, according to their activity, a neutron rate of 3×10^{10} $\frac{n}{s}$ was estimated. This rate is one order of magnitude higher compared to the one obtained with solid target [55].

2.5.4 Laser-driven ions acceleration

An innovative methods of accelerating particles is based on ultra-intense laser-plasma interaction [56, 57]. Laser-driven ion acceleration systems rely on with

focused intensities exceeding 10^{18} $\frac{W}{cm^2}$ on target, that is usually solid foils. Cut-off energies up to $\sim$ 100 MeV were demonstrated [56]. The laser-accelerated beams have a duration of the order of few picoseconds at the source and a broad energy spectrum whose features depends on the laser parameter and on the irradiated target. Another difference of laser-driven ion beams compared with conventional ion accelerators is that the effective source size of ion emission is extremely small, typically $\sim$ 10 μm. Despite the potential interest, actually laser-driven ion sources don't meet the requirements for several foreseen applications yet. In particular, the conversion efficiency of laser energy into ion kinetic energy if of few % and the broad spectrum is not suitable for several applications.
In the last years, many efforts have been made to increase the particles energy, to control the spectral and angular distribution of the beam and to increase the conversion efficiency of laser energy [57].
The most well know laser-driven acceleration scheme is the so called
target normal sheath acceleration (TNSA) in which ions are accelerated by a strong electric field, greater than 1MVμm$^-$1, generated during the interaction of ultrahigh-intensity laser pulses. TNSA can be outlined as follows: highly energetic electrons, accelerated at the front surface by the laser pulse, cross the bulk and attempt to escape in vacuum from the rear side, generating a strong electric charge-separation field. This field is high enough to ionize the back side of the target, and the resulting ions start to expand into the vacuum following the electrons [57]. All the processes that lead to ion acceleration according to the TNSA scheme are discussed in detail below.

Interaction between laser pulse and the target

When an ultra-high intensity laser pulse interacts with a solid target, a plasma is inevitably created due to heating by a relatively long preceding light, or by the optical ionization field provided by the main pulse's foot. If the target is solid, the plasma formed is typically overdense, i.e with an electronic density greater then the critical density defined in the equation 2.3:

$$n_c = \frac{m_e w^2}{4\pi e^2} = 1.1 \times 10^{21} cm^{-3} \left(\frac{\lambda}{\mu m}\right)^{-2} \tag{2.3}$$

where m_e is the mass of the electron, ω and λ are the angular frequency and the wavelength of the wave respectively, and e is the charge of electron. Given a laser pulse with angular frequency ω, if n_e is greater than n_c the plasma is called "overdense", and the pulse cannot propagate. Conversely, if n_e is lower than n_c the plasma is defined as "underdense" and the pulse can propagate. Since the laser pulse cannot propagate into the solid (overdense) regions, the absorbed energy is transported to these regions mainly by energetic (hot) electrons.

Hot electrons

The process of hot electrons generation turns out to be complex and not yet completely understood. A satisfactory theory should be able to explain several observations, such as the pulsed nature of electron generation, the conversion efficiency of the laser energy, the dependence of plasma parameters and the

energy spectra of electrons. Different models were proposed to explain the electrons acceleration, according to the polarization P or S of the incident wave (figure 2.15)[56]:

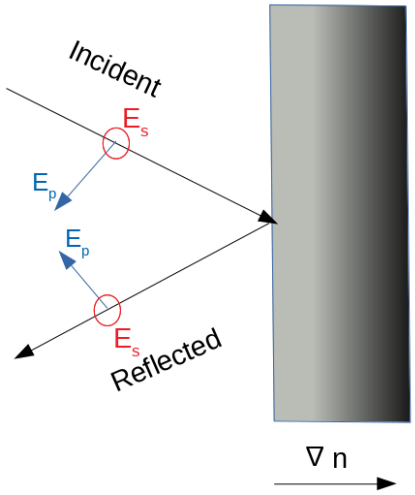

Figure 2.15: P and S polarization of wave

- **Resonance absorption** mechanism consists in the excitation of plasma oscillations in the region where $\omega = \omega_p$ at the critical surface. As a necessary condition, the wave must have oblique incidence and P-polarization. The electromagnetic field is described through an external oscillating field

$$\mathbf{E}_d = Re\left(\tilde{\mathbf{E}}_d e^{-i\omega t} \right). \tag{2.4}$$

Considering the plasma as inhomogeneous with background density $n_0(x)$ and composed by two populations, it is possible to solve the Maxwell equations coupled with the fluid description, obtaining a density perturbation:

$$\delta n_e = \frac{(\mathbf{E} + \mathbf{E}_d) \cdot \nabla n_0}{n_0(x) - n_c} \frac{1}{4\pi e}. \tag{2.5}$$

This equation shows the presence of resonance at the critical surface, when $n_0(x) = n_c$. It must be noticed that a necessary condition is $\mathbf{E}_d \cdot \nabla n_0 \neq 0$, i.e the driving field must have a component different from zero along the density gradient. If this condition is satisfied, longitudinal plasma oscillations propagate in the underdense region, and may accelerate a fraction of thermal electrons along the pulse propagation direction. This model is valid as long as that the density gradient is not too high, and hence the density is nearly constant along the oscillation amplitude [58].

- **Vacuum heating or Brunel absorption** model holds for sharp plasma density gradient, where a local plasma frequency ω_p cannot be defined. In this model, electrons are pushed out from the front surface of target by an oscillating electric field given by the superposition of the surface-perpendicular components of the incident plus the reflected laser electric field. After having performed a half oscillation on the vacuum side, they are re-injected in the target delivering their energy, which is of the order of the oscillation energy in the external field. As in the case of resonant absorption, the driving force is provided by the component of electric field parallel to the density gradient [58].

- **J $\times$ B heating** model describes the nonlinear oscillations that can be driven by the magnetic component of the Lorentz force for high intensity impulse. The main idea is to replace the driving field E_d in the electrostatic model by the longitudinal $\mathbf{v} \times \mathbf{B}$ force. The electrons dynamic is similar to previous models, with the difference that the magnetic force oscillates at 2ω, leading to the generation of hot electron bunches twice per laser period. Furthermore the oscillating component vanishes for circular polarizations, and hence the generation of hot electrons may be suppressed. The force can be written as

$$-\mathbf{v} \times \mathbf{B} = \hat{\mathbf{x}} \frac{e^2 \partial_x A^2(x)}{4 m_e \gamma c^2} \left(1 + \frac{1-\epsilon^2}{1+\epsilon^2} cos(2\omega t)\right) \tag{2.6}$$

  where **A** (x,t) is the vector potential and ϵ is the ellipticity. From this equation is easy to see that for $\epsilon = 1$, i.e circular polarization, the force is suppressed [58].

Transport of hot electrons in the solid matter has been widely investigated over the years. The main feature that characterize this regime are the very high values of current generated during the process. It can be estimated that hot electrons current can reach value of $\sim$ 15 MA over a circular spot of 10 μm radius. This large current must be locally neutralized by a return current, otherwise the fields generated from charge unbalance would stop the hot electrons in the material. The return current is constituted by free, cold electrons present as conduction electrons in metal, or produced by ionization in insulator [56].
In 2000 Hatchett et al., irradiating a thick gold foil with PW laser, estimated that about 40% - 50% of the laser energy is converted to hot electrons [59], but the conversion factor could be greater according to the type of target.

TNSA

TNSA is the main mechanism through which ions and in particular protons are accelerated. As said before, a very intense current of high-energy hot electrons may be generated at the front side of target and eventually can reach the rear side. If the target is sufficiently thin, a cloud of hot electrons can cross the rear side boundary and attempt to escape in vacuum. Because of this, the charge unbalance generates a sheath field E_s normal to the rear surface of the targets. It could be estimated that E_s can reach value of the order of $\sim 6 \times 10^{10}$ Vcm^{-1},

with a laser of irradiance $I\lambda^2 = 10^{20} W cm^{-2} \mu m^2$. This intense electric field backholds most of the escaping electrons, ionizes atoms at the rear surface, and starts to accelerate ions. In particular, protons from a thin layer of hydrogen impurities on the surface are in a favorable condition for acceleration, because they are either located where the electric field reaches its maximum values or because they present highest charge-to-mass ratio [56]. The TNSA mechanism is schematically shown in figure 2.16.

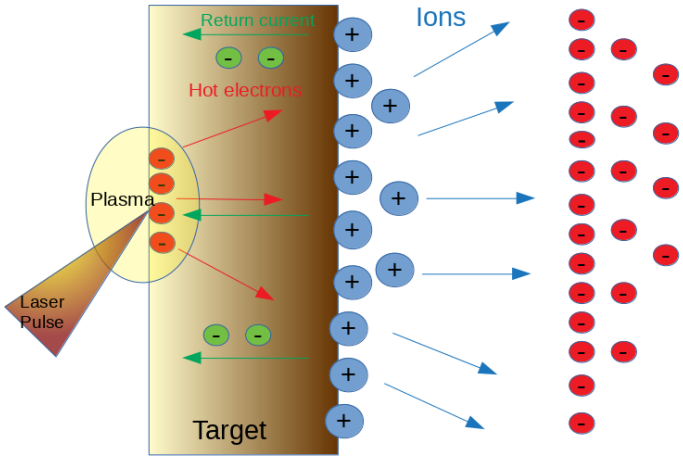

Figure 2.16: Schematic rapresentation of TNSA mechanism.

Characteristic of accelerated beams

In the laste decades different experiments reported the observation of intense emission of multi-MeV protons from solid targets with a thickness of several microns irradiated by ultra-intense lasers. Depending to the intensity of lasers, different number of protons and different maximum energy were reported [56]. R. A. Snavely et al. studied the emission of protons generated from the rear side of thin solid target irradiated by 1 PW power laser with peak intensity of $3\times 10^{20} W cm^{-2}$. The pulses duration was of 500 fs, the focal spot of 9 μm. The experiments generated bunches of 10^{13} protons with kinetic energy greater than 10 MeV and cutoff energy of 58 MeV. The energy spectrum could be well fitted with an exponential function with mean energy of 4 MeV shown in figure 2.17. The conversion efficiency of laser energy to protons with energy grater than 10 MeV was $\sim$ 12% [9].
In the last few years, different target concepts have been developed with the aim of increasing the maximum ion energy and the number of protons in the bunch. Target having an ultralow density layer, deposited on the front surface of micrometric-thick solid foil, seems to be an appealing solution to reach these goals[10, 60, 61]. Double-layer targets, composed by aluminium foil of 0.75 μm of thickness, on which is deposited a near-critical carbon foam of 12 μm and 7

$\frac{mg}{cm^3}$ of density, were irradiated. The intensity of laser pulses ranged from 0.5 to 4.5 $\times$ $10^{20} W cm^{-2}$, the focal spot was of 5 μm and the pulse duration of 30 fs. Laser polarization was changed between linear S and P, and circular. For each laser shot, bunch of 10^{10} - 10^{11} protons with angular divergence between 6° and 10° was put in motion. The spectra for different polarisations are shown in the curves a, b, and c of figure 2.18. Also the bare aluminium foil was irradiated, and its spectra can be found in the curves d and f of the same figure 2.18.

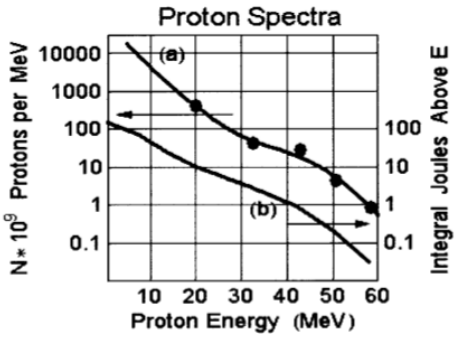

Figure 2.17: Proton energy spectrum from solid target irradiated with 3$\times$ $10^{20} W cm^{-2}$. Ref [9]

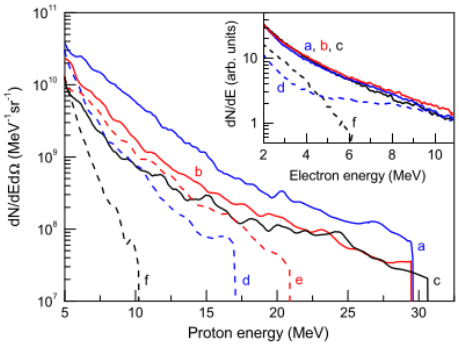

Figure 2.18: Energy spectra of the protons obtained with a laser intensity of 4.1, 3.5, 3.7 $\times$ $10^{20} W cm^{-2}$ for S, P and circular polarization (curve a, b, c) respectively, on double layer targets. The curve f and e are energy spectrum of single layer target. Ref [10]

In conclusion, laser-driven ion acceleration is currently attracting large interest worldwide because the accelerated beams have the potential to be employed in many innovative applications. Typical proton spectra are broadband up to a cut-off energy, where the proton number drops abruptly. The cut-off energy and the behaviour of the spectra depend both from the laser parameters and from the target properties. The various energy components are emitted from the target with different divergence, typically decreasing as the energy increases. The maximum proton energy achieved in function of the irradiance of the employed laser up to 2008 is shown in figure 2.19. A very recent study, [62], reported a maximum proton energy of 94 MeV.

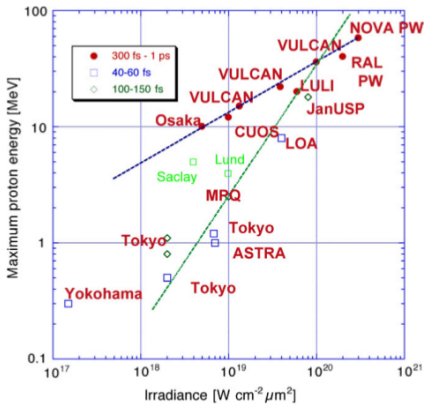

Figure 2.19: Maximum proton energy from laser-irradiated metal foils as a function of the laser pulse irradiance, from [11]

2.5.5 Review of laser-driven neutron sources

The generation of energetic neutrons from solid targets irradiated by short-pulse, high-power lasers is an area of intense experimental activity. At present there are two main methods to produce neutrons through laser facilities: exploiting the emitted ions (protons or deuterium) to induce charged particles nuclear reactions, or exploiting the emitted electrons to induce photo-neutron reactions. Here we briefly review some important recent results.

At the Texas Petawatt Laser Facility (University of Texas), protons accelerated from the rear surface of a thin target irradiated with 60 J, 180 fs laser pulses were exploited to induce (p,n) reactions in lithium targets. The laser was focused to a 10 μm diameter spot corresponding to a mean intensity of $\sim 2 \times 10^{20}$ Wcm^{-2}, and the protons were accelerated according to the TNSA mechanism. The proton angular spread at the rear surface was estimated to be $\sim 10^{\circ}$ and the total number of protons accelerated was of $\sim 7 \times 10^{11}$. Lithium converters, 4.5 mm thick, were used. The neutron yield was estimated to be around 1.6×10^7 neutrons per steradian [63].

Brenner et al. [64] proposed a convertor made up of layered stacks of materials, in order to exploit all the energy spectrum of the proton beam and to enable the photo-neutron emission. The convertor was made of 4 mm thick lithium and 1 mm thick copper (with lithium closest to target rear surface). Neutrons are generated in copper through the reaction ^{63}Cu(p,n)^{63}Zn whose cross section has a peak at $\sim$ 10 MeV, and in lithium through the reaction ^{7}Li(p,n)^{7}Be whose cross-section is peaked at 2–3 MeV proton energy. The neutron yield was predicted with the Monte-Carlo code FLUKA and it demonstrated an increase by a factor of ~ 2 in the number of generated neutrons in the forward direction, for the double layer converter compared to the single layer case (made only by lithium).

At the VULCAN laser facility of the Rutherford Appleton Laboratory, STFC, UK, an experiment was carried out exploiting a 100 TW laser [65, 66]. A laser pulse with a peak intensity of e $\times 10^{19}$ W cm^{-2} impinged on a gold foil (called pitcher), and the generated ions were directed on a ~ 2 cm thick block of lithium

(called catcher). The neutrons produced were moderated using a compact (10 cm × 10 cm × 8 cm) moderator placed at 11 cm from the source. The main component of the moderator was a (5 cm × 5 cm × 4 cm) block of polystyrene, which was designed to slow down the MeV neutrons to the epithermal range. High Z front layers (2.4 cm thick lead and 1.2 cm thick tungsten) served as reflectors to the moderated neutrons thermailzed by the polystyrene block. In the presence of high energy neutrons (∼ 10 MeV) this design would also increase the neutron population by (n, xn) reactions. The polystyrene, tungsten, and lead blocks were housed in a cm-thick aluminium structure, surrounded by 1.5 cm thick lead to reduce neutron leakage from the side walls of the moderator. A Schematic view of experimental set-up is displayed in figure 2.20.

The first stage of the experiment was devoted for characterising spectra and

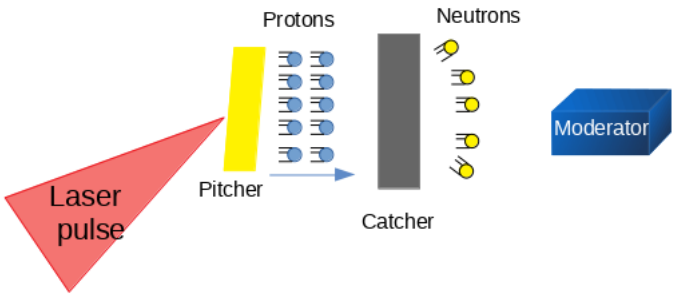

Figure 2.20: Schematic view of experimental set-up for the laser-driven neutron sources.

angular distribution of the fast neutrons produced by the catcher and the second stage was devoted to the characterization of the epithermal fluxes. The neutron flux above 2.5 MeV was measured to be $\sim 10^7$ n/Sr, whereas the spectra indicate that the highest flux lies in the sub-MeV region (estimated to be of the order of 10^9 n/sr between 0.1 and 1 MeV) [67].

At the Los Alamos National Laboratory 200 TW TRIDENT laser facility, neutrons were produced via the nuclear reactions ^{9}Be(d,n), ^{9}Be(p,n) and by deuteron breakup. The duration of laser pulse was of 600 fs and the maximum intensities reached were of $\sim 10^{20}$, 10^{21} W cm^{-2}. Using CH targets in combination with copper and beryllium converters, an isotropic neutron yield of up to 5×10^8 n/sr was observed. Using a CD_2 targets instead of the CH target, without changing the laser parameters, the observed neutron yield was of 5×10^9 n/sr [65, 66].

Still at the Texas Petawatt laser facility Austin Pomerantz et al. performed an experiment in which the electrons generated during the laser-plasma interaction were exploited for the photo-neutrons production [12]. Ultrashort laser pulses of 150 fs with 90 J of energy on target and a wavelength of 1057 nm were focused to a ∼10 μm diameter spot on thin plastic targets. The energy spectrum of electrons at forward angle ($\theta = 14°$) could be well fitted by a Maxwellian distribution (figure 2.21). These electron energies are suitable for generating bremsstrahlung radiation in an high Z material. For this purpose, a stack of 9

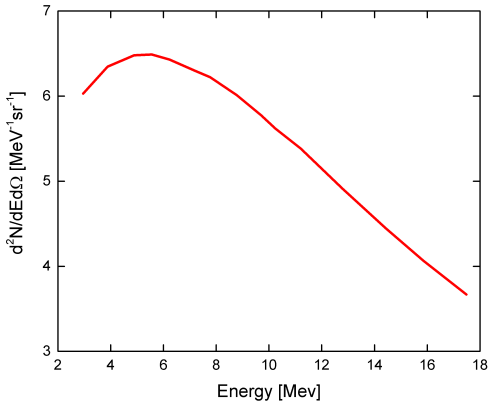

Figure 2.21: Electron energy, from [12]

Cu plates with a total thickness of 1.8 cm was placed downstream the target. While decelerating in the front layers of the Cu, the electrons generate a high-energy photon beam that propagates deeper into the stack. These photons in turn eject neutrons from Cu nuclei via the ^{65}Cu(γ,n)^{64}Cu and ^{63}Cu(γ,n)^{62}Cu reactions. The neutrons produced were measured with Bubble dosimeters at different angles (0°, 30°, 45°, 60°, 90°, 135°, 180°, and 335°). The neutron pulse duration was determined to be less than 50 fs, which correspond to a peak neutron flux of 1.1 $\times$ 10^{18} n/cm^{2}s [12].
All these work demonstrated the capability of laser system to generate neutrons. Even if the fluences obtained were not so high ($\sim$ 10^8 neutrons per steradian), considering that the temporal width of the neutron pulse is of the order of $\sim$ ns, the obtained peak fluxes are very high $\sim$ 10^{18} neutrons/cm^{2}s. These types of peak fluxes are comparable with those achieved by spallation reactions [12]. An experimental proof of an application, i.e. the neutron radiography, based on laser-driven neutron sources was performed by Roth et al [65, 68].

2.6 Open issues and goals of the thesis work

The main goal of the thesis work is to investigate the properties of a neutron source based on a laser-driven proton beam.
As underlined in the chapter 2, the neutron sources available nowadays are mainly based on reactor or spallation facilities and conventional accelerators. Despite reactor and spallation sources can provide the higher neutron fluxes, they present many disadvantages:

- the costs of building, operating and decommissioning these facilities are very high.
- a constant monitoring related to radioprotection issues must be performed, not only during the operation of the facilities, but also taking into account that the activation of the materials could give long term problems;

- the measures must be done on site. The size and the complexity of these neutron sources make them non portable, imposing the realization of the measures or of the selected application only on the site in which the source is installed;
- For reactor facilities there are considerable non-proliferation issues.

Accelerator based neutron sources reduce the costs and the issues compared to the previous cases, but they still present the downside of large dimensions which cause low manageability and require on-site applications.
Laser-driven neutron sources could in principle provide a viable alternative and an innovative method to produce neutrons whose features could be potentially appealing for different applications. In principle these systems should offer the advantages of compactness and handling, with the reduction of the size of the experimental apparatus and the associated costs. In particular, a compact $\sim$ tens of TW laser should be capable of accelerating protons up to energies suitable for inducing (p,n) reactions in materials like beryllium or lithium (i.e $\sim$ MeV). As outlined in the previous section, the features of laser-driven sources are different from the ones of conventional accelerators: first of all, laser-driven protons exhibit a broad energy spectrum and a few-degrees divergence. Moreover, laser-driven sources are inherently pulsed. Important topics to be developed are the investigation on how the features affect the neutron yields, the energy and the angular distributions. Furthermore, a laser-driven neutron source is a complex double targets system: the first target is irradiated by the laser, generating the proton beam which is directed on a second target (converter) aimed to the neutron production. Because of these, many parameters like the laser characteristics or the typology and the thicknesses of the two targets could affect the final neutron beam. An important issue is to evaluate how the variation of part of these parameters affects the neutron generation, trying to find the optimum solution depending on the type of application to be realized. The second step is to understand which applications §1.2 are suitable for a laser-driven neutron source, also in sight of the future develop and improvement of the technique.

Being able to perform realistic numerical simulations is essential to address all these problems and to interpret future experimental data. Monte Carlo codes (like Geant4) are the natural candidates to investigate this type of problems, but from the literature it is not clear the grade of the reliability of the simulations in this scenario.
The final goal of the thesis work is to perform reliable numerical simulations in order to investigate the features of a laser-driven neutron sources. To achieve this goal, two main stages are required. In the first stage it is necessary to understand what are the suitable physical models offered by the code to simulate the generation of neutrons. The second stage is to carry out a benchmark of the code, comparing its outputs with experimental or theoretical works present in literature. This was necessary because, even if Geant4 is well validated for a large range of applications (from the high energy physics to the transport of thermal neutron in matter), there is a lack of literature data and documentation for what concerns the nuclear reactions induced by low energy (< 10 MeV) charged particles. In this stage, the different hadronic physical models provided by Geant4 are tested for this range of energy.
After ensuring about the level of the reliability of the code, a comparison be-

tween a monoenergetic and a laser-driven proton beam impinging on beryllium and lithium targets is carried out. As parameter of comparison, the mean energy of the laser-driven spectrum is set equal to the energy of the monoenergetic beam. Considering the same number of incident protons on converters, neutron yields, energy spectra and angular distribution are compared underlining the differences between the two cases. In the case of monoenergetic beam, the choice of the converter thickness is made in order to maximize the yield, stopping all the particles up to energies lower than the reaction threshold. For the laser-driven case, the proton spectrum is broad 2.17, 2.18 and the variation of the converter thickness could play a significant role in the final form of neutron spectra. For these reasons, targets of different thicknesses are studied both for lithium and for beryllium.
In the final part, analysing the obtained results, the main applications that could be more realistic to realize are pointed out.
In conclusion, the structure of the thesis will be as follows: in chapter 3 the numerical code Geant4 is presented. In the first part from the general point of view and then focusing the attention on the main ingredients to build a simulation with the aim of simulating the proton-neutron reactions. The chapter 4 is dedicated to the benchmark. Chapter 5 presents a comparison between monoenergetic and laser-driven neutron sources, showing the features of neutron spectra arising from both the cases.
In the final part 6 a summary of the obtained results is shown and the future perspective are discussed.

Chapter 3

Geant4: general features, physics and implementation of the code for simulating proton-induced reactions

3.1 Introduction

GEANT4 [69] is a toolkit for simulating the passage of particles through matter and it provides a complete set of software components which can be implemented in a variety of settings. The physical processes included in the code cover a large range of phenomena including electromagnetic, hadronic and optical processes. The properties of a large set of long-lived particles, materials and elements are comprehended. Geant4 is written in C++, an object-oriented programming language.
The toolkit offers the user the ability to create a geometrical model with a large number of components of different shape and materials, and to define a *sensitive* components that record information (hits) simulating detector responses (digits). It also offers the possibility to select the set of particles of interest, and the physics processes that rule their interactions. User can also interact with the toolkit through a choice of interfaces and visualize the geometry and the tracks with a variety of graphical systems [13].
Geant4 is organized in classes and each of them deals with particular aspects of the simulation (e.g a class for the geometry, a class for the particles, a class for the output management...). Technically the user develops is own classes that inherit from those of the toolkit to implement a simulation.

3.2 Structure of the Toolkit

The classes of Geant4 are organised in categories, whose structure is shown in figure 3.2: the categories on the bottom of digram are used virtually by all higher categories and provide the foundation of the toolkit. The category *global* pro-

vides the system of units, constants, random number generators and basic types used in the code. The categories *materials, particles, graphical rappresentations* and *geometry* include classes for geometry description. *Intercomes* provides some means of interacting with Geant4 through user interface, for example the visualisation functionality.
Above these categories, reside categories that manages the tracking of particles and the processes they undergo. The *track* category contains classes for tracks and steps: in Geant4 the path of a particle and the related information are followed by object of the classes *track* and *step*. *Track* is the snapshot of a particle, and it contains physical quantities of current instance only. The track object is deleted when the particle goes out of the world volume, it disappears (by e.g. decay, inelastic scattering), it goes down to zero kinetic energy and no *AtRest* additional process is required, or the user decides to kill it artificially.
Step is defined by two points (figure 3.1) and it contains the "delta" information of a particle such as energy, momentum and time-of-flight spent by the particle in the step.

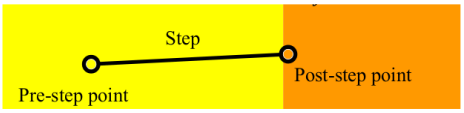

Figure 3.1: Step definition

Processes is the class category that contains implementations of models of physical interactions, and *Digits+Hints* category rules the response of sensitive detector component and the generation of event data.
In Geant4 each particle is moved step by step, and it contains a list of physical processes that can undertake. These processes may be invoked by *tracking* category, which manages their contribution to the evolution of the particle's state, and undertakes to provide information in sensitive volumes for hits and digits.
The main unit of the simulation is the *event*, that follows the single primary particle, storing information for processing further down the program chain, such as reconstruction. The information that can be stored are:

- Primary particles,
- Trajectories,
- Hits collections,
- Digit collections.

Run is the largest unit of simulation, it starts from the generation of the primary beam and finishes when all data are stored and histograms are printed. Within a run, the geometry, the set up of sensitive elements in geometry and the physics process are kept unchanged. A run is represented by a *G4Run* object, and it starts with a method of *G4RunManager* class called *BeamOn()*. G4RunManager class contains also the method *Initialize()*, that manages the construction of detector geometry, the construction of particles and physics processes and the calculation of cross sections tables. This method is thus mandatory before

proceeding to the first run.
Finally the categories *visualization*, *persistency* and *interface* connect the toolkit with external tools [13] [70].

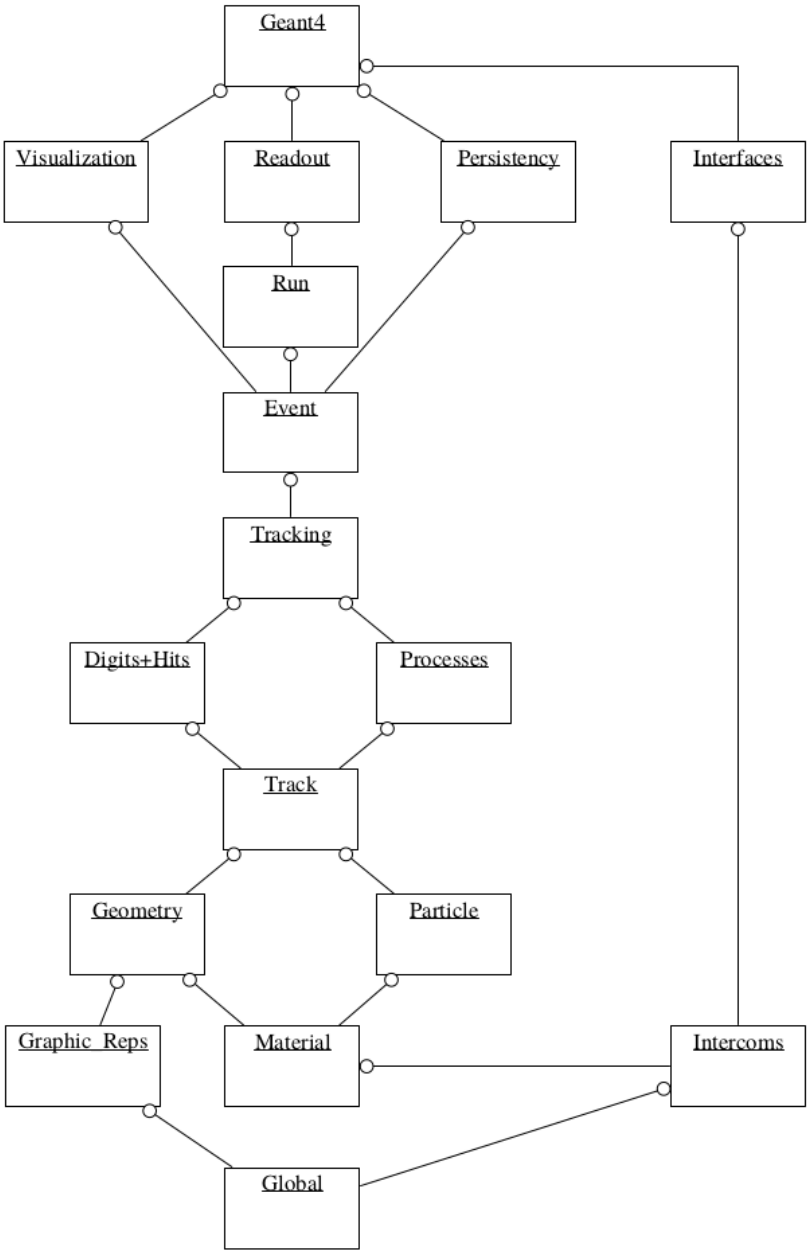

Figure 3.2: Geant4 category diagram. From [13]

3.2.1 Geometry

The geometry category allows to describe geometrical structures. The geometry definition, also called *Detector Construction*, requires the representation of geometrical elements, their materials, their positions and their logical relations to one another, such as the case of containment (e.g. if a volume is inside another one).
The first things to define in the class *Detector Construction* are the materials and the elements involved in the simulation. There are three main classes in Geant4 that manage the construction of materials:

- the *G4Isotope* class that describes the properties of atoms. The object contains a name, atomic number, number of nucleons, mass per mole;
- the *G4Element* class that describes the properties of the elements: effective atomic number, effective number of nucleons, effective mass per mole, number of isotopes, and quantities like cross section per atoms;
- the *G4Material* class that describes the macroscopic properties of materials: density, state, temperature, pressure and macroscopic quantities like radiation length, mean free path, stopping power...

Some materials are included in the internal Geant4 database, which is derived from the NIST library (National Institute of Standards and Technology) and can be built by default [71]. In this way the natural abundance of various isotopes and the properties of materials are automatically implemented. After the choice of materials, the user must implement the geometrical objects and their position. Geant4 uses the concept of *Solid Volume* to manage the shape, the concept of *Logical Volume* to manage the properties and *materials*, and the concept of *Physical Volume* to manage the spatial positioning, orientations and logical relations of geometric elements[13, 70]. This class is one of the mandatory classes that the user must implement.

3.2.2 Particles

Geant4 provides various types of particles which can be used in simulations. Each particle is represented by its own class which is derived from *G4ParticleDefinition*. Particles are organized into six major categories:

- lepton,
- meson,
- baryon,
- boson,
- short lived,
- ion.

The class *G4ParticleDefinition* has a properties which characterize individual particles, such as name, mass, charge, spin and so on. For example, neutrons are represented by the class *G4Neutrons* and one can access to the particle through the method:

```
G4Neutrons::NeutronDefinition()
```

The class *G4Ions* represents all heavy nuclei. More than one hundred types of particle are provided by default to be used in various phyiscal processes [13].

3.2.3 Primary beam implementation

One of the mandatory classes to be implemented is the *G4VUserPrimaryGeneratorAction*, that manages the way primary particles are generated. In particular the user must implement three methods to select the position, the momentum and the kinetic energy of the primary particles:

- *SetParticlePosition(x, y, z)*: this method sets the position in which the primary particles are generated;
- *SetParticleMomentumDirection(x, y, z)*: this method sets the initial direction of the primary particles;
- *SetParticleEnergy()*: this method sets the initial kinetic energy of the primary particles.

After the implementation of these three method, the user must invoke the *GeneratePrimaryVertex(anEvent)* method to generate the primary particles [70].

3.2.4 Physical Processes

Geant4 contains a large variety of physics models that cover the physics of photons, electrons, muons, hadrons and ions for energies from $\sim$ eV up to several PeV. Five main types of processes are considered:

- *electromagnetic*,
- *hadronic*,
- *decay*,
- *optical*,
- *photoelepton-hadron*.

The user must choose the relevant physical processes for the scenario of interest, and must implement them in a class called *PhysicsList*. The physics of Geant4 is discussed in detail in the next section.

3.2.5 Analysis

The toolkit includes the *g4tools* package that provides code to write and read histograms in several formats: ROOT or CSV[1] for example [70].
In Geant4 the "track" is defined as the snapshot of a particle which contains its related physical quantity. The step can be defined as the *delta* of a track and it is composed by two points in the geometry. Various types of information are

[1]CSV stands for "comma separated values" and ROOT is the format for the suite of data analysis of CERN

stored in the classes *G4Track* and *G4Step* and can be accessed by invoking various *Get* methods. Typical information available from the class G4Track are for example the dynamic particle considered, its momentum direction (unit vector), its kinetic energy and the physical volume in which it is found. All these information should be extracted in a proper class called *SteppingAction*[70]. Finally, in the class *AnalysisManager* all data extracted in the class *SteppingAction* are stored and histograms are created with the methods *CreateH1()*. The method *FillH1()* fills the histograms.

3.2.6 Main() function

The *main() function* in C++ language is the access point of the program. In the function, an instance of the class *G4RunManager* must be created. In the RunManager it is mandatory to give all the information necessary to build and run the simulation:

1. DetectorConstruction class;
2. PrimaryGeneratorAction class;
3. PhysicsList;
4. SteppingAction class;
5. AnalysisMananger class.

The first three classes are mandatory, while other classes are related to data analysis and are called *user-action classess*.
The simulation starts with the method *BeamOn(N)*, where N is the number of events, i.e. the number of primary particles shoot in the simulation. When the run finishes, G4RunManager objects are deleted, histograms are printed and the simulation ends [70].

3.3 Phyiscs of Geant4

A particle is subjected to different competing processes. Moreover, it will often travel through many regions of different materials, shapes and sizes before interacting or decaying. During the simulation, the particle proceeds in steps that follows one another according to the process the particle undergoes. It is thus necessary to use an unbiased method to choose what process limits the step and updates the parameters for the next one. Considering a particle in flight in a given material, one of the parameter that characterizes its path is the mean free path λ. This quantity is related to the cross section σ_i on isotope i of mass m_i, that has a fraction x_i in a material of density ρ through the equation 3.1:

$$\frac{1}{\lambda} = \rho \sum_i \frac{x_i \sigma_i}{m_i}. \tag{3.1}$$

The number of mean free paths which a particle travels before it interacts at the point l is given by the integral 3.2:

$$n_\lambda = \int_0^l \frac{dl}{\lambda(l)} \tag{3.2}$$

and the probability of surviving a distance l is $P(l) = e^{-n_\lambda}$. The total number of mean free paths the particle travels before reaching the interaction point, n_λ, is sampled at the beginning of the trajectory as:

$$n_\lambda = -\log(\eta), \tag{3.3}$$

where η is a random number uniformly distributed between 1 and 0. This method is used to determine the distance point of interaction or decay in current material, and considering different random numbers for different processes, it is used to decide what happens. Of course processes other than decay or interaction can also compete to limit the step, for example *continuous energy loss* or *transportation*. The process which returns the smallest distance is selected, and if there is an interaction or decay, the particle is killed and secondaries are generated. If not, the particle is transported and gets another chance to interact or decay. n_λ is updated after each step Δx according the formula 3.4:

$$n'_\lambda = n_\lambda - \frac{\Delta x}{\lambda(x)} \tag{3.4}$$

User can control the length of the steps ensuring that it is small enough so that the cross sections remain approximately constant. In principle one must use very small steps in order to ensure an accurate simulation, but the computing time increases as the step-size decreases. A good compromise depends on the required accuracy [72]. Anyway the user can try different step lengths in order to see the variation of the outputs of the code, and to search the optimum value.

3.3.1 Electromagnetic processes

The Geant4's set of electromagnetic (EM) physical processes and models are used in all types of simulations including high energy and nuclear physics experiments, beam transport, medical physics, cosmic ray interactions and radiation effects in space [13].
The *Standard EM* package includes models for the simulation of ionization, bremsstrahlung, gamma conversion and other electromagnetic interactions of particles with energies from 1 keV to 10 PeV. The *Low-energy EM* package includes alternative models for simulation of photon, electron, hadron and ion interactions at lower energies down to 100 eV. It contains also models for the simulation of atomic relaxation and other atomic shell effects, and models which describe the interaction of radiation with biological systems. The package can perform detailed simulation of particle transport in a media.

Processes involving charged particles

This package manages the energy loss processes of particles due to ionisation and bremsstrahlung. Energy loss may have continuous or discrete components: at high energy, the transfer of energy is simulated as discrete interactions in which secondary δ-electrons[2] and bremsstrahlung photons are generated. Low energy transfers are treated as a continuous process.
To evaluate the latter, consider a particle that moves in a given material with

[2]When a charged particle moves in matter, it ionizes and excites the atoms of the material, causing the emission of secondary electrons, also called δ rays.

energy E, and let $\frac{d\sigma(Z,E,T)}{dT}$ be the differential cross-section per atom (of atomic number Z) for the ejection of a secondary particle with kinetic energy T. The mean value of energy loss is obtained as a result of the integration 3.5

$$\frac{dE(E,T_{cut})}{dx} = n_{at}\int_0^{T_{cut}} \frac{d\sigma(Z,E,T)}{dT} T dT \tag{3.5}$$

where T_{cut} is the production threshold of kinetic energy of secondary particles, δ-electrons or gammas, and n_{at} is the number of atoms per volume in the material. Below this threshold the soft secondaries ejected are simulated as continuous energy loss by the incident particle, while above the threshold they are generated considering discrete process. If there are several i processes providing energy loss for a given particle, then the total continuous part of the energy loss is the sum 3.6:

$$\frac{dE_{tot}(E,T_{cut})}{dx} = \sum_i \frac{dE_i(E,T_{cut})}{dx}. \tag{3.6}$$

These values are pre-calculated during the initialization phase and they are stored in $\frac{dE}{dx}$ tables. Using these tables, the ranges of the particles in given material are calculated and stored in the so-called *range* tables. The default energy interval for these tables extends from 100 eV to 100 TeV.
Continuous energy loss imposes a limit on the step-size because of the energy dependence of the cross sections. The cross sections must be approximately constant along the step, thus its size should be small enough so that the change in cross section along the step is also small.
The *G4VeEnergyLoss* class computes the continuous energy loss of electrons and positrons. At present there are two processes contributing to the continuous energy loss of these two particles: the ionisation process, managed by the class *G4eIonisation*, and the bremsstrahlung process, managed by the class *G4eBremsstrahlung*. *G4eIonisation* calculates the contribution due to ionisation and simulates the discrete part of the ionisation (scattering or δ rays production). *G4eBremsstrahlung* computes the energy loss due to soft bremsstrahlung but also simulates discrete or hard bremsstrahlung. The *G4VeEnergyLoss* class also constructs energy loss and range tables for every material simply summing the contributions computed for ionisation and bremsstrahlung.
In the case of charged hadrons moving in matter, the ionisation processes are the only ones that contribute to electromagnetic physics. They are represented by the class *G4hIonisation* which also simulates the discrete process of hard δ rays production. The class *G4ionIonisation* is intended for the simulation of energy loss by positive ions with charge greater than unit. Inside these classes the following models are used:

- *G4BetheBlochModel*, valid for protons with T $>$ 2 MeV;
- *G4BraggModel*, valid for protons with T $<$ 2 MeV:
- *G4BraggIonModel*, valid for alpha particles with T $<$ 2 MeV;
- *G4ICRU73QOModel*, valid for anti-protons with T $<$ 2 MeV.

The integration of 3.5 leads to the Bethe-Bloch formula 3.7:

$$\frac{dE}{dx} = 2\pi r_e^2 mc^2 n_{el}\frac{z^2}{\beta^2}\left[ln\left(\frac{2mc^2\beta^2\gamma^2 T_{up}}{I^2}\right) - \beta^2\left(1+\frac{T_{up}}{T_{max}}\right) - \delta + S + F - \frac{2C_e}{Z}\right] \tag{3.7}$$

where:
r_e = classical electron radius,
mc^2 = mass-energy of the electron,
n_{el} = electron density in the material,
I = mean excitation energy in the material,
Z = atomic number of the material,
z = charge of the hadron in units of the electron charge,
$\gamma = \frac{E}{mc^2}$,
$\beta = \frac{v}{c}$,
$T_{up} = min(T_{cut}, T_{max})$,
δ = density effect function,
C_e = shell correction function,
S = spin correction term,
E = primary energy,
F = higher order corrections.

For energies below 2 MeV the precision of the Bethe-Bloch formula degrades and parametrisations of evaluated data for stopping powers at low energies are required. These parametrisations for all atoms are available from ICRU'49 report [73], that for protons is included in *G4BraggModel* class that is contained by default in the process *G4hIonisation*. The alpha particle parametrisation is used in the *G4BraggIonModel*, which is included by default in the process *G4ionIonisation*. The precision of Bethe-Bloch formula for particle's energy above 2 MeV is within 2%, but below the precision degrades and at 1 keV only $\sim$ 20% may be ensured.
To provide more stable and precise parametrisation the data from the NIST [71] databases, which provides information for 316 predefined materials, are included inside the standard package.
Finally the class *G4MultipleScattering* simulates the multiple scattering of charged particles. It simulates the scattering of the particle after a given step, computes the mean path length correction and the mean lateral displacement [72].

Photons

If the incident particle is a photon, all processes are treated as discrete interactions at the end of the step. The main processes included are the photoelectric effect, the Compton scattering and the pair production. They are modeled respectively by the *G4PhotoElectricEffect*, *G4ComptonScattering* and *G4GammaConversion* classes[72].

3.3.2 Optical processes

A photon is called optical when its wavelength is much greater than the typical atomic spacing, i.e $\lambda \geq 10$ nm, which corresponds to an energy less than 100 eV. In Geant4 optical photons are modeled with a dedicated class separated from the γ photons, allowing the simulation of processes in which the wave like property of electromagnetic radiation is predominant. The catalog of processes at optical wavelengths includes refraction and reflection at medium boundaries,

bulk absorption and Rayleigh scattering. The optical properties of the medium are stored in a properties table linked to the material[72, 13].
Any ionisation process that leaves an atom in an excited state can induce the atomic relaxation. Geant4 uses the "Livermore Evaluation Atomic Data Library", EADL [74] to describe the relaxation of atoms after they are ionised. The library includes radiative and non radiative spectrum of X-rays and electrons emitted as the atom relaxes, i.e. fluorescence and Auger process are implemented. Also PIXE (Particle Induced X-Ray Emission) can be simulated. Ionised shells are selected randomly according the ionisation cross section of each shell [72].

3.3.3 Hadronic Physics: Theory-based models

The physical models of hadronic interactions in Geant4 span more than 15 orders of magnitude in energy. The energy range goes from $\sim$ eV (the physics of thermal neutrons), through 7 TeV (for LHC experiments), to even higher values for cosmic ray physics. Of course in a single application only a small part of this range might be needed. Hence the toolkit offers a very large and flexible choice of alternative cross sections algorithms, tables and interaction models that the user can choose according to his computer memory and performance [72].
Geant4 offers a set of theory-driven models in which the cross sections of interactions and the decay channels are evaluated according to different theoretical formulas. The models are well validated for high energy physics interactions. The current set of theory-driven hadronic models includes:

- the *Quark-Gluon-String-Parton* (QGSP) model;
- the *Fritiof model* (FTF) model;
- the *Bertini cascade* (BERT) model;
- the *Liège intranuclear cascade model* (INCL++) model;
- the *Binary cascade* (BIC) mdel.

In all these models energy, momentum and most quantum numbers are conserved. They handle inelastic interactions of protons, neutrons, pions, kaons and hyperons. The user must choose the most appropriate model according to the scope and to the energy range of the simulation [72].

QGSP

The QGSP model simulates the interaction with nuclei of protons, neutrons, pions and kaons in the energy range from $\sim$20 GeV to $\sim$50 TeV. It is generally used for simulations of high energy physics [72].

FTF

The FTF model is used for simulations of hadron-nucleus interactions at $P_{lab} >$ 3-4 GeV/c and nucleus-nucleus interactions at $P_{lab} >$ 2-3 $\frac{GeV}{c}$. It assumes that

all hadron-hadron interactions are binary reactions of the type $h_1+h_2 \rightarrow h'_1+h'_2$ and, as the QGSP, it is used for simulations related to high energy physics [72].

BERT

The Bertini intranuclear cascade model handles the interactions of incident protons, neutrons, pions, kaons and hyperons up to 10 GeV. It includes the pre-equilibrium, nucleus explosion, fission and evaporation models. It treats nuclear reactions initiated by long-lived hadrons, such as protons or neutrons and γ rays with energies between 0 and 10 GeV. The model is based on the fact that, in particle-nuclear collisions, the de Broglie wavelength of the incident particle is comparable (or shorter) than the average intra-nucleon distance, hence a description of interactions in terms of particle-particle collisions is justified. The target nucleus is modeled by up to six concentric shells of constant density, and the projectile is transported along straight lines through the nuclear medium and interacts according to the mean free path determined by the free hadron-nucleon total cross section. The cascade begins when an incident particle strikes a nucleon and produces secondaries. The secondaries may in turn interact with other nucleons or can be absorbed. For light highly excited nuclei Fermi breakup or fission processes may occur. In the final stage, nuclear evaporation occurs as long as the excitation energy is large enough to remove fragments from the nucleus. Gamma emission then occurs at energies below 0.1 MeV. Relativistic kinematics is applied throughout the cascade. The cascade ends when all particles, kinematically able to do so, escape the nucleus [72, 75].
In the code this model is implemented in the class *G4CascadeInterface*.

INCL++

The Liègel intranuclear cascade was developed to study spallation reactions where ∼200 MeV incident particles are involved. The most appropriate modeling technique in this energy region is intranuclear cascade (INC) combined with evaporation model. The high-energy projectile(s) initiate an avalanche of binary collisions within the target nucleus. All the particles, nucleons and pions, are individually followed and are assumed to move in a spherical volume. Because of these collisions, emission of nucleons, pions and light cluster is possible. The cascade stops when the remnant nucleus thermalises. The list of possible applications of this model includes simulations of accelerator-driver-systems, spallation targets, radiation enviromen close to high energy accelerators and in space, proton or carbon therapy. The supported energy range for incident nucleons and pions is from 1 MeV to 20 GeV. In principle any target nucleus from deuterium is acceptable, but heavy nuclei close to the stability valley have been more thoroughly studied and tested than light or unstable nuclei. Light nuclei (from A = 2 to A = 18 included) can also be used as projectiles [72]
The model is implemented in the class *G4INCLXXInterface*.

BIC

An alternative to the Bertini-style cascade is the Geant4's Binary cascade model. It is designed for protons and neutrons with incident kinetic energy below 3 GeV,

pions with $E_{kin} < 1.5$ GeV and light ions with $E_{kin} < 3$ GeV/A. The model is based on a detailed 3-D model of the nucleus which places nucleons in space according to Woods–Saxon-shaped nuclear density for heavy nuclei with A > 16 3.8:

$$\rho(r) = \frac{\rho_0}{1 + exp\left[(r - R)/a\right]} \tag{3.8}$$

where

$$\rho_0 \sim \frac{3}{4\pi R^3}\left(1 + \frac{a^2\pi^2}{R^2}\right)^{-1}, \tag{3.9}$$

$R = r_0 A^{1/3}$, $r_0 = 1.16(1 - 1.16A^{2/3})$ and $a \sim 0.545$ fm. For light nuclei, A < 17, the nucleon density is given by a harmonic oscillator shell model 3.10:

$$\rho_0 = \left(\pi R^2\right)^{-3/2} e^{\frac{-r^2}{R^2}}. \tag{3.10}$$

An optical potential is included to simulate the collective effect of the nucleus on the nucleons participating in the reaction. For protons and neutrons as projectile, the optical potential is represented by the scalar potential 3.11:

$$V(r) = \frac{P_F^2(r)}{2m} \tag{3.11}$$

where $P_F^2(r)$ is the local Fermi momentum and m is the mass of the neutron or of the proton.
The incident particle and secondaries are then propagated through the nucleus along curved paths computed by the numerical integration of the equation of motion in the potential. The cascade terminates when the average and maximum energy of secondaries is below threshold, which varies from 18 to 90 MeV dependently on A. The model is implemented by the classes *G4BinaryCascade* [72, 75].

Pre-compound Model

For energy of the incident particles below 100 MeV, the interactions with nuclei are treated by the pre-compound model. Compound nuclei are nuclear fragments produced in the interactions that have excitation energies. The aim of this model is to dispatch individual fragments that perform the actual break up of the nucleus and to return a list of particles and nuclear fragments without excitation energies. Evaporation, fission, Fermi breakup, multi-fragmentation and photon evaporation are included by the model [76].
The model is implemented in the class *G4VPrecompoundModel* that is a subclass of *G4BinaryCascade*, *G4CascadeInterface* and of *G4INCLXXInterface* and therefore, when the user activates the Bertini, the Binary or the Liège cascade, automatically activates also the pre-compound model.

3.3.4 Hadronic Physics: Data-driven models

Besides the theory-based models, Geant4 provides also the so-called data-driven models. In these models, the cross sections and the reaction channels are not evaluated according to theoretical formulas, but are taken from data libraries.

Data driven modeling is used in the context of neutron transport, photon evaporation, absorption at rest, isotope production and calculation of cross sections for hadron nuclear scattering. Limitations exist at high projectile energies or for particles with short life-times. In these cases, the theoretical approach is employed to evaluate the missing cross-sections data. The main data driven models in Geant4 are related to proton and neutron induced isotope production or with the detailed transport of neutrons at low energies. These data are based mainly on the ENDF/B-VII (Evaluated Nuclear Data File) library [13, 72, 14].

Low Energy Charged Particle Interactions: High Precision Model

This data-driven model simulates the interactions of protons, deuterons, tritons and α particles with kinetic energies up to 200 MeV. Only inelastic interactions are included in this model, while the elastic interaction is treated by other Geant4 models. Theoretical nuclear models may fail at predicting with reasonable accuracies the nuclear cross sections. For this reason, all physical quantities relevant for an accurate modelling of nuclear reactions in Monte Carlo simulations need to be provided in a database. This database should include: cross sections, double-differential cross sections, angular distribution of emitted particles and energy spectra of the emitted particles. All this information are taken from the ENDF/B-VII evaluated data library for those few elements where data exists, and from the TENDL [15] data library when the experimental data are not available. These latter are generated through the TALYS nuclear model code. While the energy of the TENDL files goes up to 200 MeV, in the case of ENDF it only reaches 150 MeV for most isotopes and for some is even less. These library are stored in *G4NDL* format.
The model is implemented in the *G4ParticleHPInelastic* class [72].

Low Energy Neutron Interaction: High Precision Model

A class library called *G4NeutronHP*, that describes the interactions of neutrons with kinetic energies from thermal up to 20 MeV, is implemented in Geant4. Four models are included: radiative capture, elastic scattering, fission and inelastic scattering. This model can be activated in parallel with other hadronic models to provide a complete description of the physics of the simulation. All cross sections data and other information like fission spectra, fission product yields, neutron per fission and photon production data are taken from the ENDF/B-VII [14] evaluated data library. Users dealing with neutrons in this energy range, should be careful to implement and activate this model, otherwise their simulations can lead to unreliable results [72, 13].

3.3.5 Radioactive Decay processes

The process of radioactive decay is implemented in the class *G4RadioactiveDecay* which simulates the decay, either in-flight or at rest, of radioactive nuclei by α, β^+, β^- emission or by electronic capture. The simulation takes the data from the "Evaluated Nuclear Structure Data File" (ENSDF) [77], which provides information on nuclear half-lives, nuclear level structure for the nuclides and decay branching ratios [72].

3.3.6 Photolepton processes

Gamma-nuclear and lepto-nuclear reactions are handled in Geant4 as hybrid processes which require both electromagnetic and hadronic models for their implementation. The photonuclear cross sections are parameterized in the *G4PhotoNuclearCrossSection* class which covers all incident photon energies from the hadron production threshold upward. Photonuclear database contains about 50 nuclei for which the photonuclear absorption cross sections have been measured. Also an electro-nuclear reactions model was included [13, 72].

3.3.7 Precompiled Physicslists

The *PhysicsList* is one of three mandatory classes that a user must implement to perform a simulation in Geant4. In this class all particles and their interaction processes of interest should be instantiated. The user can develop his own physics list class, adding processes and particles of his interest, or can exploit pre-compiled *reference Physics Lists* which covers typical cases [78]. Focusing the attention on hadronic processes, the main pre-compiled physics lists are:

- *G4HadronPhysicsFTFP_BERT_HP*: this physics list provides elastic, inelastic, capture and fission processes. The inelastic hadron-nucleus processes are controlled by the FTF, BERT and Precompound models. In the physics list the NeutronHP package is included to simulate the physics of neutrons at energies below 20 MeV.

- *G4HadronInelasticQBBC*: as the previous physics list, it implements the elastic, inelastic, capture and fission processes. The inelastic hadron-nucleus processes are handled by the FTF, BERT, BIC and Precompound models. In particular, the Binary cascade is used from 0 to 1.5 GeV for the interactions of protons and neutrons with nuclei.

- *G4HadronPhysicsINCLXX*: this physics list contains QGS, FTF, INCL++ and pre-compound model to simulate hadronic interactions. It is indicated for simulating the spallation reactions.

- *G4HadronPhysicsQGSP_BIC_HP*: in this physics list the inelastic hadron-nucleus processes are implemented by the QGS, FTF, BIC and Precompound models. The physics of neutrons below 20 MeV is handled by the High Precision neutron model.

- *G4HadronPhysicsQGSP_BIC_AllHP*: this class is similar to the previous *G4HadronPhysicsQGSP_BIC_HP*, but it contains also the subclass *G4ParticleHPInelastic* that simulates the interaction of low energy charged particles exploiting the evaluated data file and the cross sections provided by the ENDF/B-VII and TENDL libraries.

3.4 Implementation of proton-induced reaction

This section explains in detail how to write an application in order to simulate the generation of neutrons through proton-induced reaction on beryllium

or lithium targets.

3.4.1 Geometry

The first class to be developed is the *DetectorConstruction* class, in which the materials and the geometrical shape of the objects are declared. The chosen geometry consists in a rectangular target of beryllium or lithium, contained in a sphere whose task is to collect and to register all the generated particles. Recalling the subsection §3.2.1, the first thing to define are the materials employed in the simulations. This could be done either using the implementation of the methods *G4Material* and *G4Elements*, or exploiting the NIST database. In the following lines of code lithium, beryllium, lead and vacuum (called "Galactic") are instantiated in the method *DefineMaterials*:

```
#include "DetectorConstruction.hh"
#include "G4Material.hh"
#include "G4Element.hh"
#include "G4NistManager.hh"
void DetectorConstruction::DefineMaterials()
{
//vacuum
  G4double a;
  G4double z;
  G4double density;
  new G4Material ( "Galactic", z=1., a=1.01*g/mole,
                 density = universe_mean_density,
                  kStateGas, 2.73*kelvin, 3.e-18*pascal);

  G4Element* Be = new G4Element ("Beryllium", "Be",  4.,
                                 9.01*g/mole);
  G4Element* Li = new G4Element ("Lithium",  "Li",  3.,
                                 6.941*g/mole);
  G4Element* elPb = new G4Element ("Lead", "Pb", 82.,
                                 207.2*g/mole);

G4NistManager* nistManager = G4NistManager::Instance();
 nistManager->FindOrBuildMaterial("G4_Pb");
 nistManager->FindOrBuildMaterial("G4_Be")
 nistManager->FindOrBuildMaterial("G4_Li")
 }
```

After having defined the materials and the elements used in the simulation, it is necessary to define the shape, the placement and the relations of various geometric elements. This could be done using the concept of *Solid, Physic* and *Logical Volumes*.
The largest volume that must be created is the *World* volume, which contains all other volumes. It also must be unrotated and it is placed at the origin of coordinate system. Generally it is best to choose a simple solid like a box for the *World*. In this case, the material that constitutes the World is the vacuum ("Galactic"). In the chosen geometry, a small rectangular target of beryllium (or lithium) is placed at the origin of reference frame, inside an a sphere of lead called *envelope*. The envelope is necessary to stop and register all the particles generated during the simulations, and if it is not present, some errors will occur because the particles cannot reach the boundary of the World volume. To define the shape of the geometrical elements, Geant4 provides a set of special

methods to be implemented: for example *G4Box* is the method to create a box and *G4Sphere* is the method to create a sphere. The methods *G4LogicalVolume* and *G4PVPlacement* (Physical volume) should be correctly implemented for all the elements. All these methods have been implemented in the method *DefineVolumes()*:

```
#include "DetectorConstruction.hh"
#include "G4Sphere.hh"
#include "G4Box.hh"
#include "G4LogicalVolume.hh"
#include "G4PVPlacement.hh"

G4VPhysicalVolume* DetectorConstruction::DefineVolumes()
{
\\definition of materials of geometrical elements
G4Material* worldMaterial = G4Material::GetMaterial ("Galactic");
G4Material* envMaterial = G4Material::GetMaterial ("G4_Pb");
G4Material* targetMaterial = G4Material::GetMaterial ("G4_Be");
                                (or it could be "G4_Li")

\\definition of World Volume
G4double worldSizeXY = 40*m;
G4double worldSizeZ = 40*m;

 G4VSolid* sWorld                \\ Solid volume of World
   = new G4Box("World",          \\ Name
               worldSizeXY/2, worldSizeXY/2, worldSizeZ/2
               \\ Dimensions);

  G4LogicalVolume* lWorld        \\ Logical volume of World
    = new G4LogicalVolume(
               sWorld,           \\ its solid object
               worldMaterial,     \\ its material
               "World");          \\ its name

  G4VPhysicalVolume* pWorld      \\ Physical volume of world
    = new G4PVPlacement(
               0,                \\ Rotation matrix (in this
                                    case it is not rotated)
               G4ThreeVector(),  \\ Positioning vector
               lWorld,           \\ its Logical volume
               "World",           \\ its name
               0,                \\ its mother volume
               false,             \\ no boolean operation
               0,                 \\ its copy number
               fCheckOverlaps);    \\ control of overlaps

\\ Construction of the Envelope
  G4double pRmin = 10*m;
  G4double pRmax = 15*m;
  G4double pSPhi = 0;
  G4double pDPhi = 360*deg;
  G4double pSTheta = 0;
  G4double pDTheta = 180*deg;

  G4VSolid* sEnv
    = new G4Sphere ("envelope",
              pRmin, pRmax, pSPhi, pDPhi, pSTheta, pDTheta);

  G4LogicalVolume* lEnv
    = new G4LogicalVolume(
```

```
                    sEnv,
                    envMaterial,
                    "envelope");

  new G4PVPlacement(
                    0,
                    G4ThreeVector(),
                    lEnv,
                    "envelope",
                    lWorld,
                    false,
                    0,
                    fCheckOverlaps);

\\Contruction of the Target volume,
\\in this case of 0,250 mm of thickness
  G4VSolid* sTarget
    = new G4Box("Target",
                    2.5*cm/2, 2.5*cm/2, 0.250*mm/2);

  G4LogicalVolume* lTarget
    = new G4LogicalVolume(
                    sTarget,
                    targetMaterial,
                    "Target");

  new G4PVPlacement(
                    0,
                    G4ThreeVector(0*cm,0*cm,0*cm),
                    lTarget,
                    "Target",
                    lWorld,
                    false,
                    0,
                    fCheckOverlaps);
                    }
```

In figure 3.3 it is shown how a solid envelope appears in the interactive mode of Geant4. Furthermore simple solids can be combined using "Boolean" operations: union, intersection or subtraction. The constituent solid of a Boolean operation should be composed avoiding the sharing of all or part of their surfaces. Through these operation it has been possible to create a lithium target on a tungsten backing through which flows water channels. Figure 3.4.

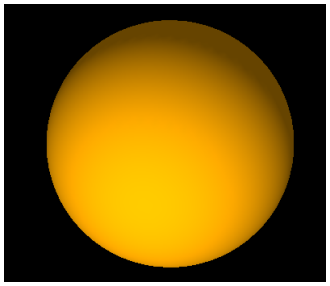

Figure 3.3: Interactive mode of Geant4: solid envelope

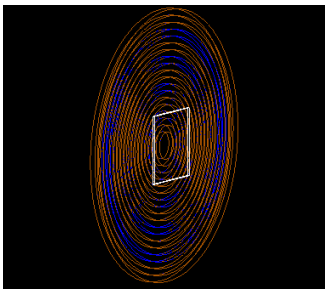

Figure 3.4: Interactive mode of Geant4: lithium target on copper backing through which water channels flow.

3.4.2 Primary proton beam

The second class to be implemented is the *PrimaryGeneratorAction* in which the type of primary particles, their initial position, momentum and kinetic energy should be declared. This is done through the "Set" methods explained in subsection 3.2.3.

```
PrimaryGeneratorAction::PrimaryGeneratorAction()
: G4VUserPrimaryGeneratorAction(),
fParticleGun(0)
//Constructor
{
  G4int n_particle = 1;
  fParticleGun  = new G4ParticleGun(n_particle);
  G4ParticleTable* particleTable =
  G4ParticleTable::GetParticleTable();
  G4String particleName;
  G4ParticleDefinition* particle =
  particleTable->FindParticle(particleName="proton");
  fParticleGun->SetParticleDefinition(particle);
  fParticleGun->SetParticleMomentumDirection(G4ThreeVector(0.
                                          ,0. -1.));
  fParticleGun->SetParticleEnergy(1*MeV);
}

PrimaryGeneratorAction::~PrimaryGeneratorAction()
//Destructor
{
  delete fParticleGun;
  delete gunMessenger;
}

void PrimaryGeneratorAction::GeneratePrimaries(G4Event* anEvent)
{
  G4double x0 = 0*cm;
  G4double y0 = 0*cm;
  G4double z0 = 10*cm;
  fParticleGun->SetParticlePosition(G4ThreeVector(x0,y0,z0));


  G4double DivAngle = G4UniformRand()*6*deg;
  G4double RandAngle = G4UniformRand()*360*deg;
```

```
  G4double x1 = std::sin(DivAngle)*std::cos(RandAngle);
  G4double y1 = std::sin(DivAngle)*std::sin(RandAngle);
  G4double z1 = -std::cos(DivAngle);

  fParticleGun->SetParticleMomentumDirection
                (G4ThreeVector(x1,y1,z1));

  fParticleGun->SetParticleEnergy(5*MeV);

  fParticleGun->GeneratePrimaryVertex(anEvent);
  }
```

In the example above it is shown how to generate a beam of monoenergetic protons of 5 MeV with an angular divergence of 6°, starting from the position (0, 0, 10 cm). The figure 3.5 shows the process in the interactive mode of Geant4.

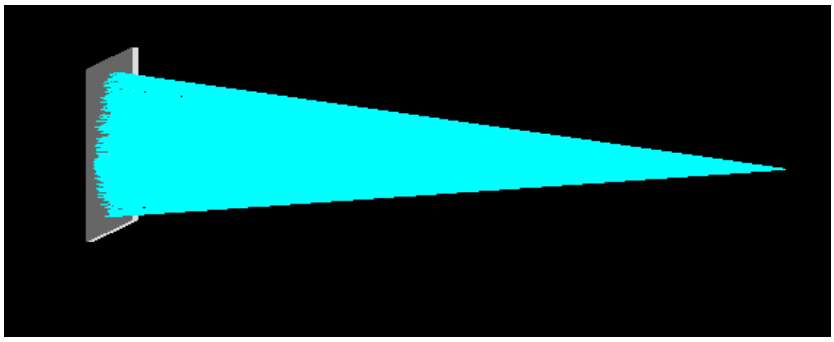

Figure 3.5: Beam of protons on target.

3.4.3 Physics

For our purposes, the two main categories of physical processes to consider are the electromagnetic physics and the hadronic physics. The electromagnetic physics is important to simulate in the correct way the release of energy and the stopping power of the protons inside the targets. The hadronic physics should include the elastic and the inelastic interactions, and the high precision model for the neutron transportation inside the material.
An example of *Electromagnetic PhysicsList* is given below:

```
ElectromagneticPhysics ::
ElectromagneticPhysics(const G4String& name)
   :  G4VPhysicsConstructor(name)
   {
   SetPhysicsType(bElectromagnetic);
   }

   ElectromagneticPhysics::~ElectromagneticPhysics()
{ }
void ElectromagneticPhysics::ConstructProcess()
{
  G4PhysicsListHelper* ph =
  G4PhysicsListHelper::GetPhysicsListHelper();
```

```
  auto particleIterator=GetParticleIterator();
  particleIterator->reset();
  while( (*particleIterator)() ){
    G4ParticleDefinition* particle = particleIterator->value();
    G4String particleName = particle->GetParticleName();

    if (particleName == "gamma") {

      ph->RegisterProcess(new G4PhotoElectricEffect(),    particle);
      ph->RegisterProcess(new G4ComptonScattering(),      particle);
      ph->RegisterProcess(new G4GammaConversion(),      particle);

    } else if (particleName == "e-") {

      ph->RegisterProcess(new G4eMultipleScattering(),    particle);
      ph->RegisterProcess(new G4eIonisation(),            particle);
      ph->RegisterProcess(new G4eBremsstrahlung(),        particle);

    } else if( particleName == "proton" ||
               particleName == "pi-" ||
               particleName == "pi+"     ) {

      ph->RegisterProcess(new G4hMultipleScattering(), particle);
      ph->RegisterProcess(new G4hIonisation(),          particle);

    } else if( particleName == "alpha" ||
               particleName == "He3"     ) {

      ph->RegisterProcess(new G4hMultipleScattering(), particle);
      ph->RegisterProcess(new G4ionIonisation(),          particle);
      ph->RegisterProcess(new G4NuclearStopping(),        particle);

    } else if( particleName == "GenericIon" ) {

      ph->RegisterProcess(new G4hMultipleScattering(), particle);
      G4ionIonisation* ionIoni = new G4ionIonisation();
      ionIoni->SetEmModel(new G4IonParametrisedLossModel());
      ph->RegisterProcess(ionIoni,                        particle);
      ph->RegisterProcess(new G4NuclearStopping(),        particle);
    }
  }
}
```

Here it is possible to see how, given a specific particle identified by the method *GetParticleName()*, different processes available for this latter are implemented and activated for the simulation. Of great importance for our purpose, is the activation of the *G4hIonisation* for protons, through which, as explained in §subsection 3.3.1, the stopping power is simulated. The user can choose which processes to consider and which processes to neglect, according to the scenario he wats to reproduce. As it is possible to see in figure 3.6 and 3.7, if the electromagnetic physics is not activated, the particles travel in the media without taking into account the stopping power, but considering only hadronic or nuclear scattering interactions.
For the hadronic interactions, there is the possibility to exploit the precompiled physics lists explained in subsection §3.3.7. In the following lines of code, how to implement one of the different pre-compiled physicslists is shown. This is done using the method *RegisterPhysics()* in the constructor of the class Physicslist:

```
#include "ElectromagneticPhysics.hh"
#include "G4HadronPhysicsFTFP_BERT_HP.hh"
```

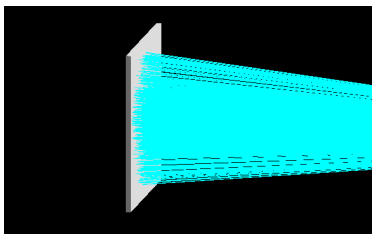

Figure 3.6: Geant4 interactive mode: Electromagnetic physics activated.

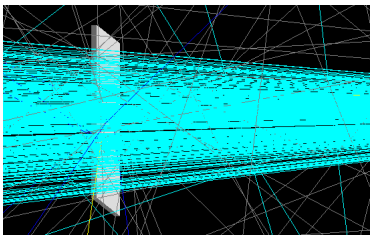

Figure 3.7: Geant4 interactive mode: Electromagnetic physics not activated.

```
#include "G4HadronPhysicsQGSP_BIC_HP.hh"
#include "G4HadronInelasticQBBC.hh"
#include "G4HadronPhysicsINCLXX.hh"
#include "G4HadronPhysicsQGSP_BIC_AllHP.hh"
PhysicsList::PhysicsList()
:G4VModularPhysicsList()
{
  G4int verb = 0;
  SetVerboseLevel(verb);

  //add new units
  //
  new G4UnitDefinition( "millielectronVolt",
                        "meV", "Energy", 1.e-3*eV);
  new G4UnitDefinition( "mm2/g",  "mm2/g",
                         "Surface/Mass", mm2/g);
  new G4UnitDefinition( "um2/mg", "um2/mg",
                        "Surface/Mass", um*um/mg);

  // Hadron Elastic scattering
  RegisterPhysics( new HadronElasticPhysicsHP(verb));

  // Hadron Inelastic Physics
  ////RegisterPhysics( new G4HadronPhysicsFTFP_BERT_HP(verb));
 // RegisterPhysics( new G4HadronPhysicsQGSP_BIC_HP(verb));
  ////RegisterPhysics( new G4HadronInelasticQBBC(verb));
  ////RegisterPhysics( new G4HadronPhysicsINCLXX(verb));
  RegisterPhysics( new G4HadronPhysicsQGSP_BIC_AllHP(verb));

  // EM physics
  RegisterPhysics(new ElectromagneticPhysics());
}
```

The physicslists that are not on comment are activated and implemented for the simulation. In this case, for the hadronic inelastic interaction the *G4HadronPhysicsQGSP_BIC_AllHP* is chosen, for the elastic interactions the *HadronElasticPhysicsHP* and for the electromagnetic interactions the *ElectromagneticPhysics* shown before.

3.4.4 Collection of data and creation of histograms

As explained in §3.2.5, the collection of data should be done in a class called *SteppingAction* through "Get" methods. Since we are interested in the neutron spectra and angular distributions, the quantity to be collected are the kinetic

energy of each neutron and its momentum direction. This is done exploiting the methods *GetKineticEnergy()* and *GetMomentumDirection*(), which extract from the "Track" the desired quantities.

```
#include "SteppingAction.hh"
#include "G4Step.hh"
#include "G4RunManager.hh"
#include "G4Neutron.hh"
#include "G4Track.hh"
#include "G4LogicalVolumeStore.hh"
#include "AnalysisManager.hh"
#include "G4LogicalVolumeStore.hh"

void SteppingAction::UserSteppingAction(const G4Step* step)
{
 G4Track* theTrack = step->GetTrack();

 //kill particles that hit the envelope
 envVolume = G4LogicalVolumeStore::GetInstance()
                          ->GetVolume("envelope");

  if ((step -> GetTrack() -> GetDynamicParticle()
                       -> GetDefinition()) =
                          G4Neutron::Definition())
  {
    G4LogicalVolume* theVolume
      = step->GetPreStepPoint()->GetPhysicalVolume() ->
                                   GetLogicalVolume();
    if (theVolume == envVolume) {
       theTrack->SetTrackStatus(fStopAndKill);
       return;
    }
}

 //extraction of kinetic energy
if ((step -> GetTrack() -> GetDynamicParticle() ->
   GetDefinition()) == G4Neutron::Definition())
  {
  if ((step -> GetPreStepPoint() -> GetPhysicalVolume() ->
  GetName()) == "World")
    {
    if ((step -> GetPostStepPoint() -> GetPhysicalVolume() ->
     GetName()) == "envelope")
     {
        G4double NeutronEnergy = step ->
        GetPostStepPoint() -> GetKineticEnergy();

     \\sending information to the AnalysisManager class
    AnalysisManager* analysis = AnalysisManager::getInstance();
    analysis -> analyseStepping1(NeutronEnergy);
      }
    }
  }
 //extraction of momentum direction
  if ((step -> GetTrack() -> GetDynamicParticle() ->
   GetDefinition()) == G4Neutron::Definition())
  {
    if ((step -> GetPreStepPoint() -> GetPhysicalVolume() ->
    GetName()) == "World")
    {
    if ((step -> GetPostStepPoint() -> GetPhysicalVolume() ->
    GetName()) == "envelope")
```

```
    {
       G4ThreeVector m = step -> GetPostStepPoint() ->
       GetMomentumDirection();

   G4double mx = m.x();
   G4double my = m.y();
   G4double mz = m.z();
   G4double mmm = sqrt(pow(mx,2)+pow(my,2)+pow(mz,2));
   G4double angz = acos(mz/mmm);

AnalysisManager* analysis = AnalysisManager::getInstance();
        analysis -> analyseStepping6(angz);
      }
    }
  }
}
```

The first lines of the class shown above invokes the method *SetTrackStatus(fStopAndKill)* that "kills" all particles that hit the envelope. This is necessary to avoid errors related to a particle that goes to infinite in the World.
Other lines show how to extract the kinetic energy and the momentum direction of the neutrons generated in the simulation: when neutrons hit the envelope, these information are registered and sent to methods of the class *AnalysisManager*. In this class, data are registered and histograms are created.

```
#include "AnalysisManager.hh"
#include "g4csv.hh"
#include "g4root.hh"
#include "G4VProcess.hh"
#include "G4Step.hh"

void AnalysisManager::book()
{
  G4AutoLock l(&dataManipulationMutex);
  G4AnalysisManager* man = G4AnalysisManager::Instance();
  man -> OpenFile(outputFileName);
  man -> SetFirstHistoId(1);

  man -> CreateH1("h1","Spectrum of the emitted neutrons",
                                          100, 0, 4);
  man -> CreateH1("h2", "Angular distributions of neutrons",
                                        100, 0, 180);
  man->SetH1Plotting(1,true);
  man->SetH1Plotting(2,true);
}

void AnalysisManager::analyseStepping1(const G4double
                                      energyNeutron)
{
  G4int id = 0;
  G4AutoLock l(&dataManipulationMutex);
  G4AnalysisManager* man = G4AnalysisManager::Instance();
   man -> FillH1(1, energyNeutron/MeV);
}

void AnalysisManager::analyseStepping6(const G4double Angle)
{
  G4int id = 0;
  G4AutoLock l(&dataManipulationMutex);
  G4AnalysisManager* man = G4AnalysisManager::Instance();
```

```
   man -> Fill H1(2, Angle/deg);
}
```

3.4.5 Main()

All the classes that user implemented must be given to the *Main()* through the *RunManager* object.

```
int main ()
{
G4RunManager* runManager = new G4RunManager ;
// Mandatory classes
runManager -> SetUserInitialization( new DetectorConstruction );
runManager -> SetUserInitialization (new PhysicsList);
runManager -> SetUserInitialization ( new PrimaryGeneratorAction );
// Optional Classes
runManager -> SetUserInitialization ( new AnalysisManager ) ;
runManager -> SetUserInitialization ( new SteppingAction ) ;

runManager -> initialise;
int numberOfEvent = 10;
runManager -> BeamOn( numberOfEvent);
delete runManager ;
return 0;
}
```

In conclusion, the management of the program is administrated by the run-manager, which must be provided, through the pointers to the appropriate classes, with all the information needed to set up the simulation.
The simulation starts with the method BeamOn(N), where in this case N is the number of primary protons sent, and finishes when all the particles are killed and registered by the envelope (or are stopped) and the histograms are printed.

Chapter 4

Benchmarking the code against experimental and theoretical data from the literature

4.1 Recall of the available physicslist

In order to perform Geant4 simulations of proton-induced nuclear reactions, it is of primary importance to assess which physical models are suitable for this kind of simulations As underlined in Chapter 3, Geant4 provides a set of theoretical and data-driven models to simulate the hadronic interactions of particles with nuclei. In order to evaluate the reliability of the code, its outputs using different models are compared with experimental or theoretical results from the literature. Recalling the section §3.3.3, the theoretical hadronic models which simulate the interactions of protons with nuclei are: the Bertini cascade (BERT), the Binary cascade (BIC) and the Liège intranuclear cascade (INCLXX). These models are contained in the following precompiled physicslists:

- $G4HadronPhysicsFTFP\_BERT\_HP$
- $G4HadronPhysicsQGSP\_BIC\_HP$
- $G4HadronInelasticQBBC$
- $G4HadronPhysicsINCLXX$

one from There is also the data-driven model, called "ParticleInelasticHP" which simulates the inelastic interactions of protons, deuterons, tritons, He-3 and alpha particle with kinetic energies up to 200 MeV. The model is contained in the precompiled physicslist

- $G4HadronPhysicsQGSP\_BIC\_All\_HP$.

Cross section data are taken from the ENDF/B-VII [14] evaluated data library for those few elements where data exist, while, for the most of isotopes, data

are taken from the TENDL library [15].
The total neutron yields and, when possible, the neutron spectra computed for each model are compared and they are checked against literature data. This has been done either for beryllium or for lithium converters.

4.2 Simulations with Beryllium converter

Let's consider the behaviour of the code implementig a simulation in which proton beam impinges on a beryllium target. Reproducing the same geometry of the experiment of Howard et al. [5], a monoenergetic (3.7 Mev) proton beam impinges on a 2.5 cm × 2.5 cm, 0.250 mm thick target. All the neutrons produced during the simulation are ideally detected for all the solid angle. The outputs from the simulations are compared with the experimental results of Howard et al. and Agosteo et al. [5, 7] 2.5.3. The figure 4.1 shows the interactive view the simulation:

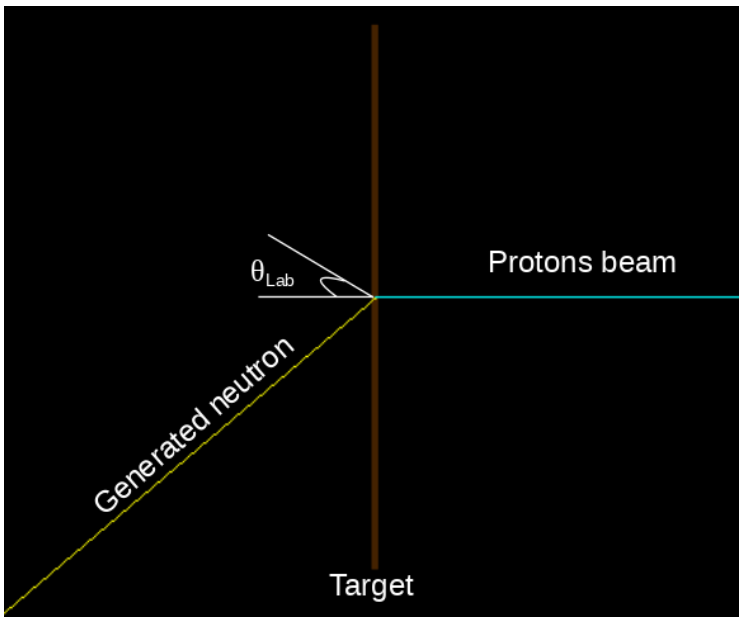

Figure 4.1: Geant4 interactive mode: monoenergetic beam of protons on beryllium target.

4.2.1 Benchmark of the theory-based models

Table 4.1 shows the neutron yields obtained for each theory-driven model, while figure 4.2 shows the corresponding energy spectra.
From the table 4.1 and from the figure 4.2 it is possible to observe how the theory-based models fail catastrophically in reproducing experimental data, underestimating the neutron yields of factor of two orders of magnitude.

Physics List	Total Yield $\frac{neutrons}{mC}$
FTFP_BERT_HP	5.81×10^9
QGSP_BIC_HP	3.56×10^9
QBBC	3.50×10^9
INCLXX	4.62×10^9
Howard et. al, experimental yield	$9{,}61 \pm 0.48 \times 10^{11}$

Table 4.1: Neutron yields obtained performing simulations with different theory-driven models, compared with the experimental yield from the literature [5].

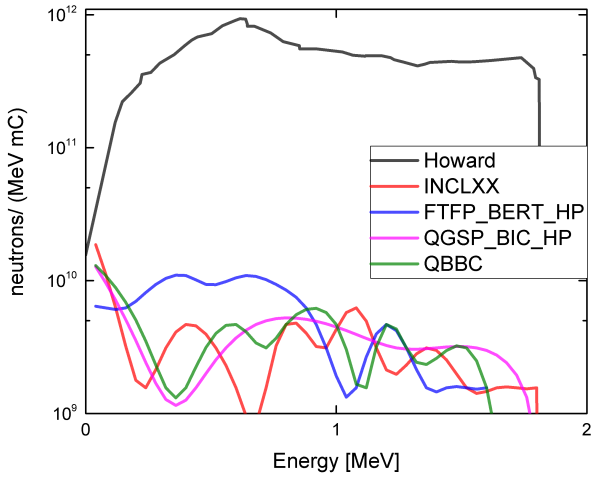

Figure 4.2: Neutron spectra obtained from monoenergetic proton beam of 3.7 MeV impinging on beryllium target. Comparison between theory-driven models of Geant4 and experimental results from Howard [5].

4.2.2 Benchmark of the data-driven model

Considering the energy range of interest, i.e from 0 to $\sim$ 5 MeV, the two main channels of the reaction p + ^{9}Be are:

- The compound nucleus reaction ^{9}Be + p $\rightarrow$ ^{10}B $\rightarrow$ ^{9}B + n;
- The three body breakup: ^{9}Be(p, p' + n)^{8}Be.

The cross section for the compound nucleus reaction is included in the ENDF/B-VII library, while the cross section for the three body breakup is taken from the TENDL library. The cross sections for the two process are shown in figures 4.3 and 4.4 respectively.
Geant4 refers to these two data libraries [72]. It must be remebered that the cross sections from the TENDL library are not evaluated on the base of experiments, but generated from TALYS code, hence their behaviour can be different from the real experimental one. Despite this, focusing the attention on the energy interval of interest and summing the two cross sections, it is possible to

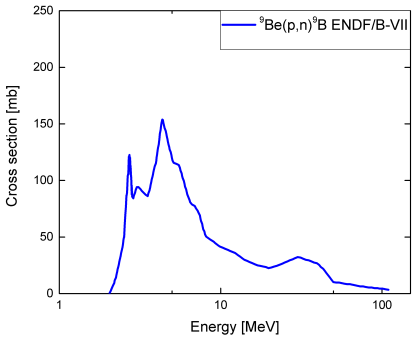

Figure 4.3: ^{9}Be(p,n)^{9}B cross section from ENDF/B-VII data library [14].

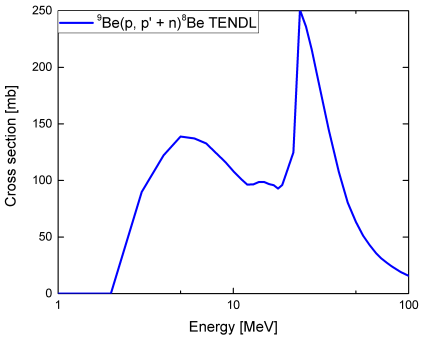

Figure 4.4: ^{9}Be(p, p' + n)^{8}Be cross section from the TENDL data library [15].

verify that there is a good agreement between the sum of the previous two cross sections and the total experimental one given by Marion [6]. The comparison is shown in figure 4.5 and it indicates that in the code the right behaviour of the cross sections, at least for this interval of energies, is taken into account.

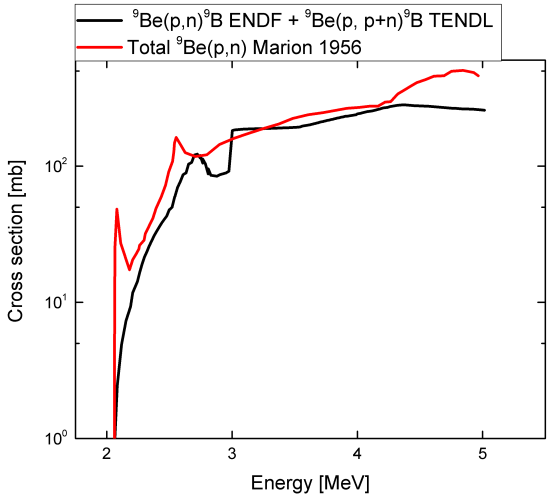

Figure 4.5: Total cross section ^{9}Be(p,n) compared with the sum of ^{9}Be(p,n)^{9}B plus ^{9}Be(p, p' + n)^{8}B cross sections.

The comparison between neutron spectrum obtained with the data-driven *ParticleInelasticHP* model and the experimental one by Howard et al. [5] is shown in figure 4.6.
The total yield obtained compared with the experimental one is shown in table 4.2:

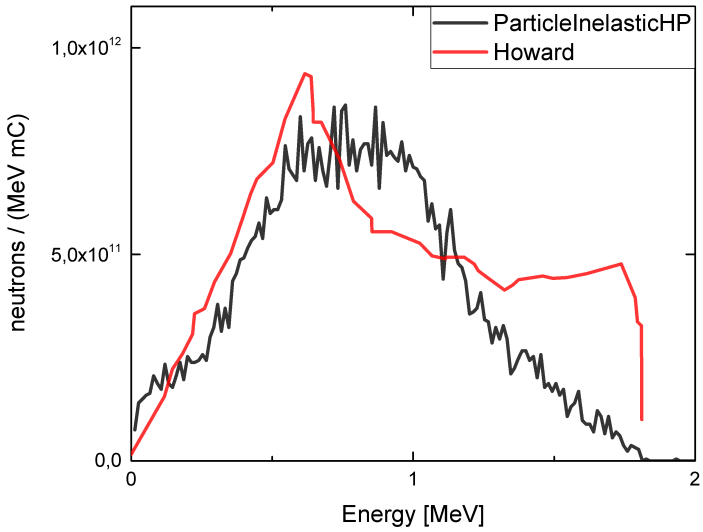

Figure 4.6: Neutron spectra obtained from a monoenergetic proton beam of 3.7 MeV impinging on a beryllium target. Comparison between data-driven model and experimental results from Howard et al. [5].

PhysicsList	Total Yield $\frac{neutrons}{mC}$
$QGSP\_BIC\_All\_HP$	7.5×10^{11}
Howard et. al, experimental yield	$9{,}61 \pm 0.48 \times 10^{11}$

Table 4.2: Total neutron yield: Comparison between PaticleInelasticHp model and experimental data from [5].

Figure 4.6 table 4.2 show that the results of the data-driven model are in reasonable agreement with experimental ones. The neutron yield estimated by the simulation is $\sim 22\%$ less than the experimental yield. The shape of the spectrum exhibits correctly the broad peak at neutron energy of 600 KeV where the distribution is dominated by the three-body breakup.
Compared with the results obtained with the theory-based models, that underestimate the neutron yield by a factor of 100, the data-driven model shows better precision.
Geant4 offers also the possibility to extrapolate the angular distribution of emitted particles: in figure 4.7 the neutron angular distribution obtained from the simulation is compared with the experimental angular distribution from [5].

It is possible to observe a good agreement between the curves, in particular for angles greater then 60°. The fact that the yield increases at lower angles, showing a maximum at 0°, is due to the forward-peaked distribution of the break-up neutrons [8, 48].
A further benchmark of the code can be done performing simple numerical inte-

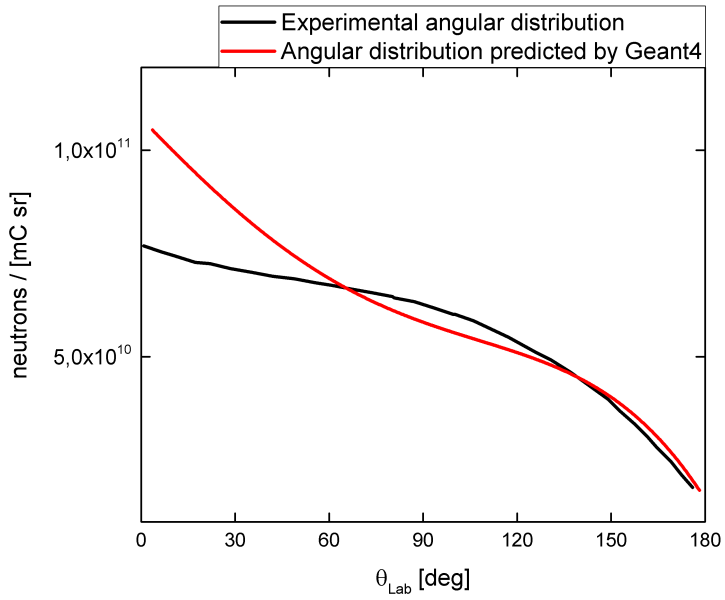

Figure 4.7: Angular distributions: Geant4 output compared with experimental data from [5].

gration of the analytical expression of the total neutron yield as a function of the cross-section and as a function of the proton energy 4.1. In these calculations it was assumed that monoenergetic proton beam stops completely in the target.

$$Y = N\frac{N_A}{m_w}10^{-27}\int_0^{E_p}\sigma(E)\frac{dE}{dE/dx}\rho \tag{4.1}$$

Where:

- N is the number of protons that impinges on the target;
- N_A is the Avogadro's number;
- m_w is the molecular weight of the material;
- ρ is the density of the material;
- E_p is the initial kinetic energy of the beam;
- $\sigma(E)$ is the cross section for the proton-neutron reaction;
- $\frac{dE}{dx}$ is the mass stopping power taken from the *SRIM* code [79], given in $\frac{\mathrm{MeVcm^2}}{\mathrm{mg}}$.

The equation 4.1 was numerically integrated for different beam energies using the two cross sections showed in figure 4.5: the cross section from Marion et al [6] and the sum of compound nucleus σ_{cp} and three-body breakup σ_{bu} cross sections given by ENDF and TENDL libraries. The results of the integration

are shown in table 4.3 where they are compared with the Geant4 outputs and the experimental data from Howard et al. and Agosteo et al. [7, 5]. The yields are given in neutrons/mC.

Energy [MeV]	$\sigma_{cp} + \sigma_{bu}$	Marion	Geant4	Experimental Data
2	0	0	0	•
3	$3{,}9 \times 10^{11}$	$3{,}1 \times 10^{11}$	$3{,}49 \times 10^{11}$	•
3.7	$8{,}4 \times 10^{11}$	9.8×10^{11}	7.5×10^{11}	9.06×10^{11}
4	$1{,}26 \times 10^{12}$	$1{,}38 \times 10^{12}$	$1{,}32 \times 10^{12}$	$1{,}48 \times 10^{12}$
5	$2{,}84 \times 10^{12}$	$3{,}7 \times 10^{12}$	3×10^{12}	$3{,}50 \times 10^{12}$

Table 4.3: Comparison between neutron yields from numerical integration of 4.1, Geant4 outputs and experimental data from [5] and [7]. The yields are given in $\frac{neutrons}{mC}$.

The values in the table seem to be coherent to each other. In particular the yields predicted from Geant4 for the different energies do not differ from the others for factor greater than $\sim$ 25 %. Also the comparison between the yields from experimental cross section (Marion) and the cross sections implemented in Geant4 shows that there is a good agreement, and the discrepancies do not exceed the $\sim$ 25 %. This is a further proof of the reliability of the code and it demonstrates the correct behaviour of the data-driven model and of the cross sections on which it is based.

4.3 Simulations with lithium converter

The behaviour of the ^{7}Li(p,n)^{7}Be cross section shows a threshold value for protons energy of 1.88 MeV and a resonance at 2.25 MeV (See subsection §2.5.1). The shape is shown in figure 4.8. The geometry reproduced in the simulation is similar to the one used for the case of beryllium showed in figure 4.1, with the difference that the target thickness was set at 700 μm. This thickness was chosen because these type of targets are commercially available [80], and 2.25 MeV protons completely stop in them. The yields obtained from the simulations are compared with the theoretical work of C.L Lee et al. [19] or with the experimental results of Bayanov [21] and Yu et al. [20].

4.3.1 Benchmark of the theory-based models

In the simulations with theory-based models, a monoenergetic proton beam with energy of 2.25 MeV was chosen in order to explore the resonance region in the cross section. The neutron yields resulting from the simulations is shown in 4.4, and it is compared with the yield predicted by C.L Lee [19].

Theory-driven models are completely inadequate to simulate protons impacting on lithium target for energy range below 2.25 MeV.

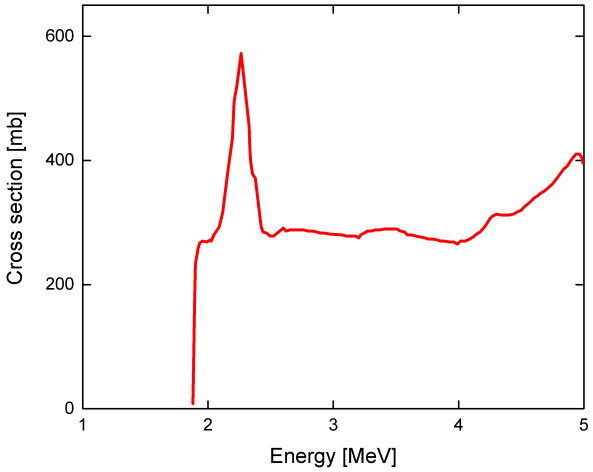

Figure 4.8: Lithium cross section from ENDF/B-VIII [14] data library.

Physics List	Total Yield $\frac{neutrons}{mC}$
FTFP_BERT_HP	0
QGSP_BIC_HP	0
QBBC	0
INCLXX	0
C.L. Lee theoretical predicted yield	$4{,}6 \times 10^{11}$

Table 4.4: Neutron yield of different theory-based physics models compared with the yield predicted by CL. Lee et al. [19]

4.3.2 Benchmark of the data-driven model

To check the reliability of the data-driven model (*ParticleInelasticHP*) implemented, two simulations with different monoenergetic proton beam impinging on the lithium target were performed: 1.91 MeV and 2.25 MeV. The first energy is near the threshold of the reaction, and the second one is centred on the resonance of the cross section 4.8. From the literature, at these energy, the only reaction that contributes to the neutron production is the ^{7}Li(p,n)^{7}Be, whose cross section is included in the ENDF/B-VII library and it is shown in 4.8. Geant4 refers to these data to compute the neutron yields during the simulations.
The results of simulations are displayed in table 4.5.

The obtained yields from the simulations of Geant4 show a very good agreement with literature data at 2.25 MeV, while at 1.91 MeV the discrepancy is of $\sim$ 20%. The neutron energy spectrum obtained from 1.91 MeV beam is displayed in figure 4.9, where it is possible to observe that the maximum neutron energy is of the order of $\sim$ 100 KeV, in aggreement with the experimental results from [20]

Energy MeV	Model	Yield $\frac{neutrons}{mC}$
1.91	*QGSP_BIC_All_HP*	2.03×10^{10}
1.91	C.L Lee	2.41×10^{10}
1.91	Bayanov et al.	2.6×10^{10}
1.91	Yu et al.	$2{,}7 \times 10^{10}$
2.25	*QGSP_BIC_All_HP*	4.8×10^{11}
2.25	C.L Lee	$4{,}6 \times 10^{11}$

Table 4.5: Comparison between neutron yields simulated with Geant4 and works from literature [20, 21, 19].

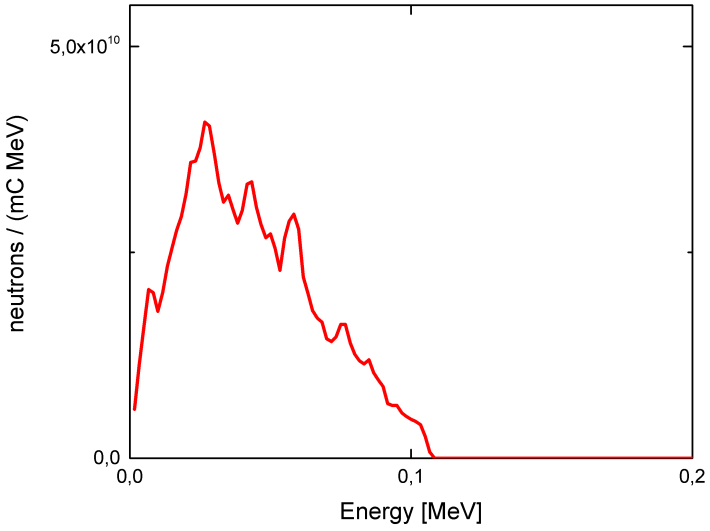

Figure 4.9: Neutron energy spectrum from monoenergetic proton beam at 1.91 MeV.

The simulated angular distribution for the 1.91 MeV case (figure 4.10) shows that the neutron flux is forward peaked. This agrees with literature data, in which it is shown that, for energies of incident protons near the threshold value, the outgoing neutrons are emitted with a narrow cone along the incident proton direction [20]. These forward-peaked neutron fluxes are very appealing for applications such as BNCT because allow to focus the dose, saving the healthy tissues. At incident energies of proton beam greater than 1.9 MeV, neutron yields are greater and the angular distributions become wider. These features are clearly visible in the results of the simulation performed at 2.25 MeV (see figure 4.11).
As done for the beryllium target, also in this case a benchmark based on direct integration of equation 4.1 was carried out. The target was assumed to be thick enough to stop all the protons. The results of the integration are compared with

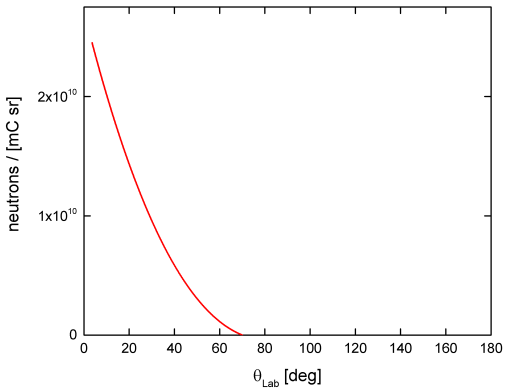

Figure 4.10: Neutron angular distribution obtained with 1.91 MeV incident protons: Geant4 output with ParticleIneasticHP model.

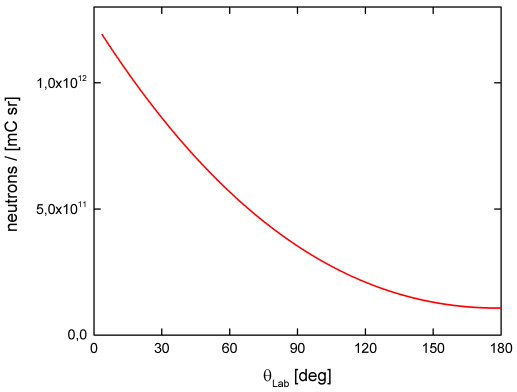

Figure 4.11: Neutron angular distribution obtained with 2.25 MeV incident protons: Geant4 output with ParticleIneasticHP model.

Geant4 outputs and with literature data taken from [19].

Energy [MeV]	σ_{cp}	Geant4	C.L Lee theoretical predictions
1.91	8.7×10^{9}	2.03×10^{10}	2.41×10^{10}
2	8.73×10^{10}	8.7×10^{10}	1.1×10^{11}
2.25	4.3×10^{11}	4.8×10^{11}	4.8×10^{11}
3	1.3×10^{12}	1.8×10^{12}	•
4	2.9×10^{12}	3.6×10^{12}	•
5	4.9×10^{12}	7.0×10^{12}	•

Table 4.6: Comparison between neutron yields from numerical integration of 4.1, Geant4 outputs and theoretical predicted values from C.L Lee [19]. The yields are given in neutrons/mC.

The agreement between the data present in the table 4.6 indicates the reliability of the data-driven *ParticleInelasticHP* model and of the cross section data.

4.4 Reliability of the code with data-driven model

The benchmarks presented in this chapter show that, in order to simulate in accurate manner nuclear reactions induced by low-energy charged particles, it is necessary to use data-driven models. Theory-driven models fail catastrophically in this energy range, with discrepancies up to two orders of magnitude with respect to experimental results. These models were developed for proton energies ranging from $\sim$ 100 MeV to TeVs [72] and are based on theoretical

formulas through which cross sections and emission probabilities are evaluated. The extrapolations of the information for low energy interactions leads to errors and non accurate findings.
Since the data-driven model is based on experimental results, simulations are more accurate and are able to reproduce experimental data with acceptable errors.
It is important to point out that these considerations are valid for beryllium and lithium and care should be taken if other elements are used. Indeed, while for a small set of materials (including beryllium and lithium) very detailed cross sections are included in Geant4 libraries, in the general case the code falls back to TENDL libraries. These libraries consist in cross sections evaluated with TALYS code and, while being more precise than other theory-driven models, their coarse energy resolution ($\sim$ 1 MeV) could make them unsuitable for some applications.
Once it is checked that the yields, the spectra and the angular distributions are in good agreement with literature data, it is possible to proceed and to consider reliable the results of the next chapter.

Chapter 5

Proton-neutron conversion: comparison between conventional and laser-driven proton sources

5.1 Aims of the investigations

As discussed in section §2.5.4, laser driven sources could be an appealing alternative for neutron generation. Laser-driven proton beams are characterized by a broad energy distribution (typically exponetial-like) and by an angular distribution wider than that of traditional accelerators. Investigating how these features influence neutron generation is important to assess the feasibility of laser-driven neutron sources.
In this chapter, the neutron yields, spectra and angular distributions emerging from the simulations with monoenergetic proton beams are compared with yields, spectra and angular distributions of simulations with laser-driven exponential proton beams. As a parameter of comparison, the mean energy of the laser-driven proton beam was set equal to the energy of the monoenergetic beam. This was performed either for beryllium or for lithium converters. Since the choice of the thickness of the converters is not obvious in the case of an exponential proton beam, various thicknesses were investigated in order to study how this affects the yield.
Laser-driven proton sources are pulsed (1 bunch per laser shot) and each bunch contains 10^9 - 10^{10} protons. Thus, in the simulations, the primary beam is a bunch of 10^9 protons impacting on the target, with the aim of simulating the one obtained from the single laser shot.
The spectrum of laser-driven proton beam considered in the simulations is an ideal one (figure 5.1), and it is taken from [10]. The cut-off energies were set up at 2 MeV and 10 MeV, and its mean-energy is equal to 2.66 MeV. The lower cutoff at 2 MeV is not physical, because the laser-accelerated spectrum extends also at lower energies, but the choice of this value is justified by the fact that, both for beryllium and for lithium, the (p,n) cross section becomes important

for energies greater than 2 MeV (figures 4.4, 4.8). The angular divergence of the laser-driven beam was chosen at 6°, while in the monoenergetic case the beam is collimated like in figure 4.1. A compact laser system, whose power is of the order of tens of TW, is able to produce a proton beam with these features. Is

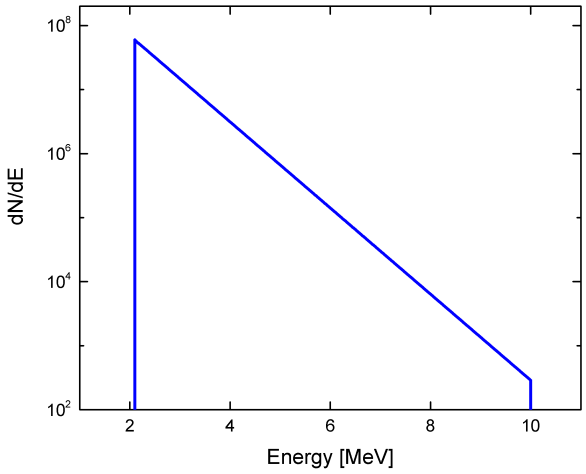

Figure 5.1: Laser-driven proton spectrum taken from [10]

important to remark that for these type of converters (beryllium and lithium) and for these range of energies, the code was benchmarked in chapter 4. Thus we expect that the results are reliable.

5.2 Beryllium Target

5.2.1 Features of the simulations

The geometry chosen for the simulations with beryllium as converter is similar to the one used in chapter 4: a 2.5 cm × 2.5 cm beryllium foils with various thicknesses on which proton beam impinges. Figure 5.2 displays the laser-driven proton beam impinging on the target and the yellow lines represent the neutrons generated during the simulation.

In the monoenergetic case, the thickness of the target was set up at 250 μm (sufficient to stop all the protons), while for the laser-driven cases the following thicknesses were chosen:

- 800 μm, sufficient to stop all the laser-driven beam in the target.
- 500 μm, sufficient to stop protons up to 7.5 MeV. Protons with energies greater than $\sim$ 8 MeV, if not involved in a reaction, exit from the rear side at energies greater than the threshold, and are lost.
- 330 μm, sufficient to stop protons up to 6 MeV. Protons with energies greater than $\sim$ 6.5 MeV, if not involved in a reaction, exit from the rear side at energies greater than the threshold, and are lost.

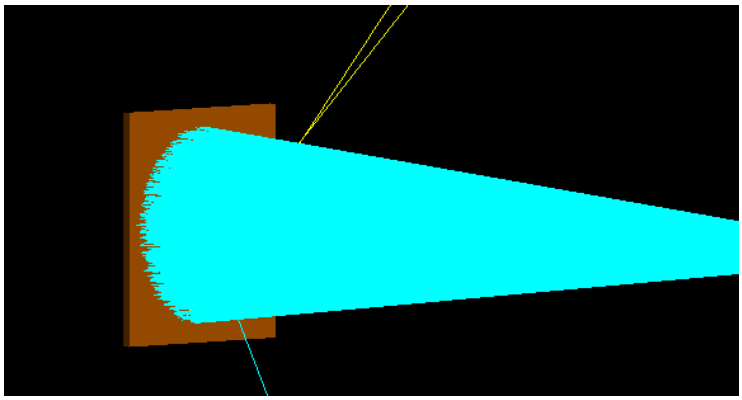

Figure 5.2: Geant4 interactive mode: proton beams with angular divergence on beryllium target.

- 250 μm, sufficient to stop protons up to 5 MeV. Protons with energies greater than $\sim$ 5.7 MeV, if not involved in a reaction, exit from the rear side at energies greater than the threshold, and are lost.

An investigation on how this converter reduction affects the neutron spectra and yields could be interesting in order to find the optimum solution, also considering the costs of manufacturing. Indeed all these target typologies can be easily produced industrially [81]. A further thinning of the target would implies greater production costs and could lead to an excessive lost of protons from the rear side, for these reason the minimum thickness was set at 250 μm. Recalling the energies involved, the mean energy of the exponential proton beam is 2.66 MeV, set equal to the energy of the monoenergetic case.

5.2.2 Obtained neutron spectra and discussion of results

Figure 5.3 shows all the obtained neutron spectra, while the obtained angular distributions are shown in 5.4. The total yields are shown in table 5.1.

Thickness μm	**Total number of neutrons**
Monoenergetic case	
250	18721
Laser-driven case	
250	37871
330	38106
500	38193
800	38206

Table 5.1: Neutron yields obtained for 10^9 impinging protons, for different thicknesses.

For the same number of incident protons (i.e. 10^9), the neutron yields from the laser-driven proton beam are approximately double compared to the monoenergetic case. This is due to the fact that the exponential spectrum contains an

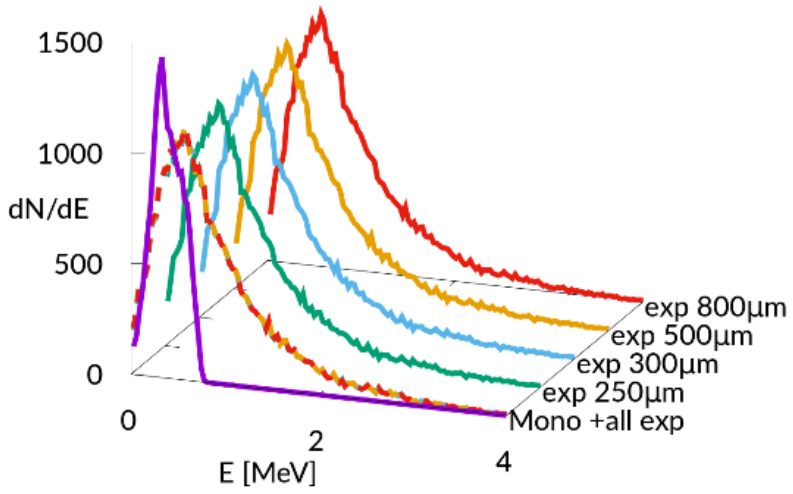

Figure 5.3: Neutron spectra obtained form simulations.

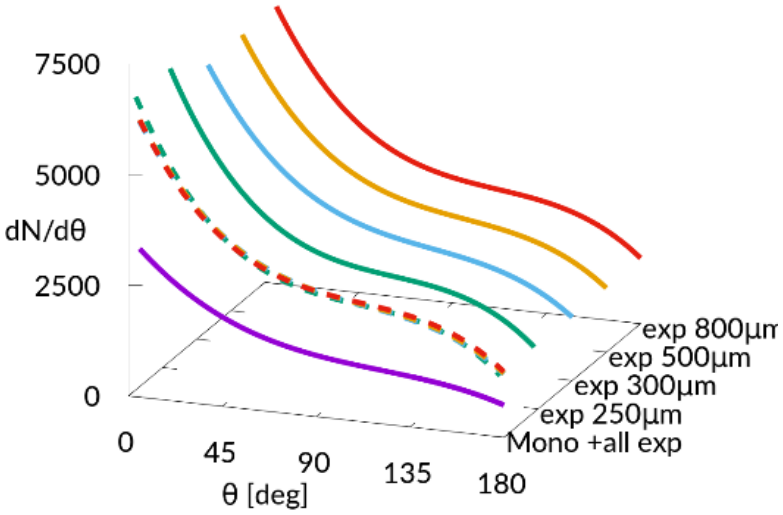

Figure 5.4: Angular distributions obtained form simulations.

amount of protons with energy greater than the monoenergetic case, and this allows to explore regions where the cross section reaches its maximum value, that is around 5 MeV 4.3. In particular, for proton energy greater than 3 MeV, the three-body breakup channel becomes important, leading to a sensitive increase of the total yield.

The neutron energy spectra for the laser-driven cases are broader than for monoenergetic case, and this agrees with the fact that more energetic protons can excite higher nuclear levels of ^{10}B. More energetic protons also cause more energetic neutrons from the three body breakup reactions. Furthermore, the angular distributions in the laser-driven cases are more forward peaked because of the massive presence of breakup neutrons. The comparison between monoenergetic and laser-driven neutron spectra is shown in 5.5.

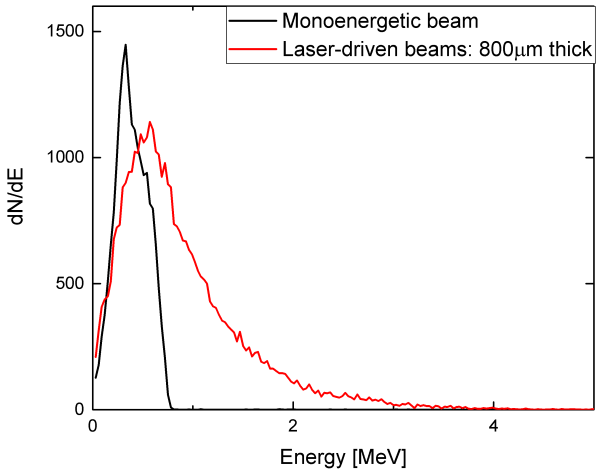

Figure 5.5: Neutron spectra obtained from monoenergetic protons and laser-driven protons.

It is also possible to observe that, even if there is a reduction of target thickness of $\sim$ 30%, the neutron yield remains approximately constant (it varies only of $\sim$ 1%). The loss of protons from the rear side is mitigated from the fact that the more energetic protons are in the tail of the exponential spectrum, and for this are much less compared to lower energy protons that lose completely their energy in the converter, remaining available for the reaction.
Considering a laser that works with a frequency of $\sim$10 Hz, accelerating proton bunches of $\sim 10^9$ - 10^{10} particles it is possible to achieve neutron currents of $\sim 10^6$ neutrons/s. Since the current delivered by the lasers is not as high as the one delivered by conventional accelerators, beryllium targets could run for a long time neither suffering the blistering, nor presenting issues related to material melting.

5.3 Lithium Target

5.3.1 Features of the simulations

The geometry chosen for the simulations with lithium targets is the same of that with beryllium. Proton beams monoenergetic and laser-driven, impinge on 2.5 cm $\times$ 2.5 cm foils of different thicknesses 5.2. Since Lithium presents low

melting point (180.5°), the loss of radioactive liquid lithium during the irradiation could be dangerous both from chemical and radiological point of view. To avoid these issues, in literature is suggested to use liquid lithium. It could be interesting to investigate the different neutron energy spectra and yields arising from the different state of lithium: simulations with either solid or liquid lithium were implemented.
The laser-driven proton spectrum delivered on lithium targets is the same of the previous simulations 5.1.
The chosen thicknesses were: 700 μm for the monoenergetic proton beam on solid target; 700 μm and 1.5 mm for the laser-driven proton beam on solid target; 1.5 mm for the laser-driven proton beam on liquid target.
The thicknesses chosen for the solid cases are commercially available [80]. A 700 μm foil is able to stop 5 MeV protons, while the 1.5 mm foil can stop 8 MeV protons. This latter thickness was also chosen to perform a comparison between solid and liquid converters of the same thicknesses. In the liquid case, is not easy to control the thickness of the flow and, referring to the experiment of Halfon et al. [55], it was set at 1.5 mm.
As underlined previously, during the irradiation the target might melt, and for this in literature is suggested to cool the targets with proper coolant channels. At this purpose, other two simulations with particular geometries were implemented: the first one consists in 700 μm thick solid target laid on a 3 mm thick tungsten disk through which 8 circular water channels are dug. Each channel has a rectangular section of 2 x 5 mm^2. The second one consists in a 700 μm thick solid target embedded in a copper cone through which water channels are dug. The aim of these two simulations is to study the effects of the coolant (water) and of the backing on the generated neutron energy spectra. In the second case, because of the difficulties related to the reproduction of the exact geometry present in the article, the aim of the simulation is not to reproduce in realistic way the experiment, but to give some ideas about the neutron spectrum and the angular distribution in the case of conical geometry. These types of backings are similar to those proposed in literature by Bayanov et al. and [53] and Wills et al. [54].
The figure 5.6 shows the interactive mode of the simulation for the conical geometry.

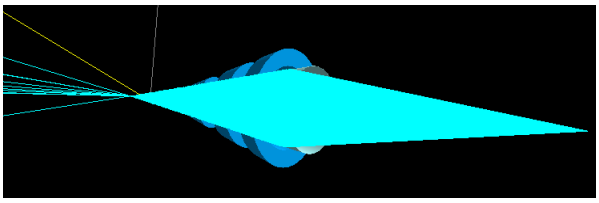

Figure 5.6: Geant4 interactive mode: laser-driven proton beam that impinges on conical lithium target.

5.3.2 Obtained neutron spectra and discussion of results

The neutron energy spectra obtained and the angular distributions are displayed in figures 5.7 and 5.8 respectively. The total yield is shown in table 5.2. The

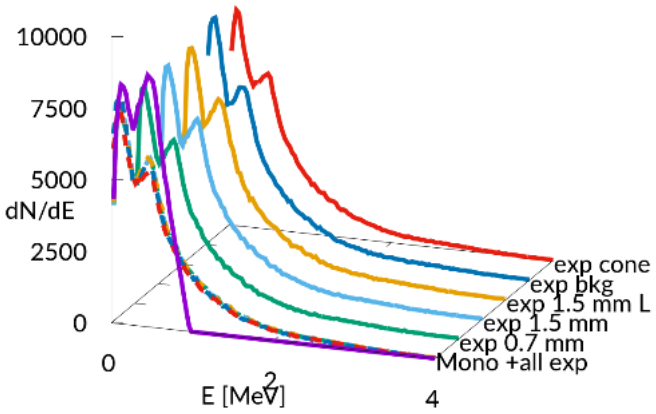

Figure 5.7: Obtained neutron energy spectra.

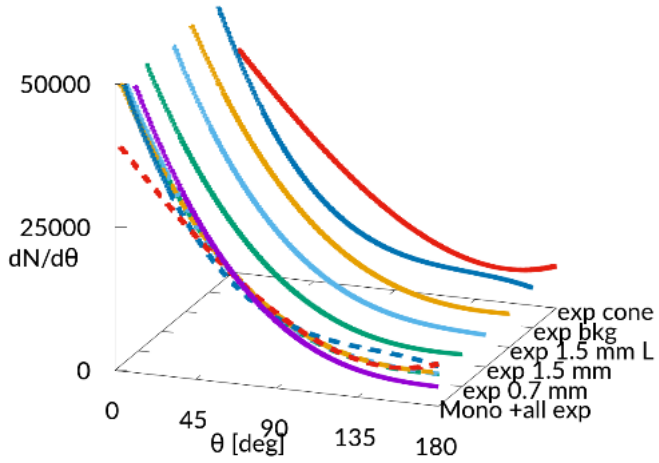

Figure 5.8: Obtained neutron angular distributions.

simulations show that the neutron yield does not vary much between monoenergetic proton beam and laser-driven proton beam. This agrees with the shape of σ(p,n) cross section which shows a resonance at 2.25 MeV, thus a large amount of neutrons are produced in this region either from the monoenergetic beam or from the laser-driven beam. The cross section exhibits another smaller peak at 5 MeV which is explored by the high energy tail of laser-driven protons, leading to an increase of the yields against the monoenergetic case.

Geometry and target thickness mm	Total number of neutrons
Monoenergetic case	•
0.700	189080
Laser-driven cases	•
0.700 (solid)	194628
1.5 (solid)	196623
1.5 (liquid)	196678
0.700 (Tungsten backing)	194105
0.700 (Cone geometry)	186681

Table 5.2: Neutron yields obtained for 10^9 impinging protons, for different target geometries.

From the simulations, it is also possible to observe that the variation of the thickness does not influence the yields decisively. For the 700 μm case we obtained 1.94 neutrons per 10^4 protons while for the 1.5 mm case we obtained 1.96 per 10^4 protons. This small difference is due to the fact that, in the thicker target, protons up to $\sim$ 8 MeV of the spectrum 5.1 are slowed down until $\sim$ 2 MeV being useful for the reaction, while, for the thinner target, only protons up to 5.50 MeV are slowed down until 2 MeV. Protons with energies greater than 8 and 5.50 MeV respectively, if don't react are lost. The scale of the effect is mitigated by the fact that the lost protons are from the tail of the spectrum and thus are much less compared to lower energy protons that reach the peak at 2.25 MeV, maximizing the probability of the reaction.
The neutron spectra and the yields from the liquid and the solid converters are very similar. This is in agreement with the fact that the density of two states are very close (0.53 $\frac{g}{cm^3}$ for the solid and 0.512 $\frac{g}{cm^3}$ for liquid) and hence also the stopping powers of protons are close.
Like the beryllium case, the neutron energy spectra from laser-driven beams reach higher energies (the maximum energy achieved is $\sim$ 5 MeV), while for the mononenergetic case the maximum energy reached by the neutron is $\sim$ 1 MeV. This is because higher energy protons can excite higher nuclear levels in ^{8}Be, leading to more energetic emission of particles. The comparison between neutron yields from monenergetic and laser-driven proton beam on the solid target of 700 μm is shown in figure 5.9.
The angular distribution between the two cases are similar forward peaked because of the large amount of protons with energy near the threshold of reactions. The presence of the thin tungsten backing does not influence much the spectrum and the angular distribution. Indeed the yield is 1.94 generated neutrons for 10^4 impinging protons both for the bare target and for the laid target. This is due to the low amount of water present, not sufficient to give rise to a massive absorption and moderation of the neutron beam.
For the conical geometry, it is interesting to observe how the angular distribution results more isotropic.

Considering, like in the case of beryllium converter, a laser that works with a frequency of $\sim$10 Hz and can accelerate protons bunches of 10^9 - 10^{10} particles, it is possible to achieve a currents of $\sim 10^7$ $\frac{neutrons}{s}$.

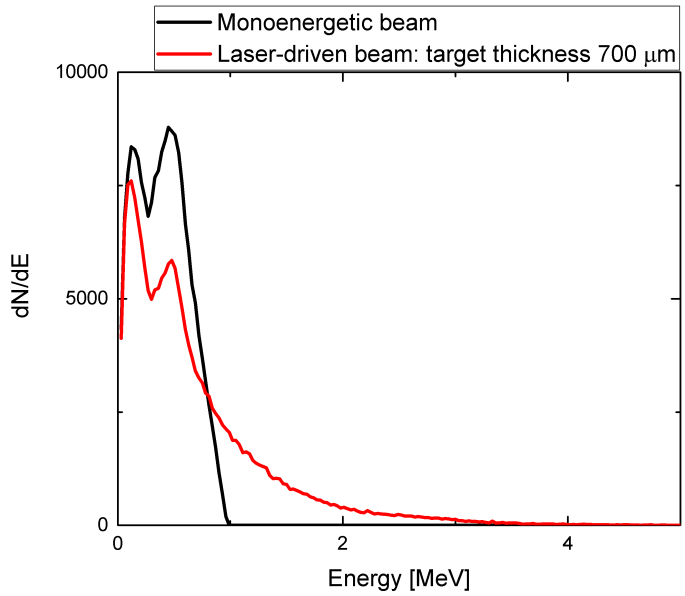

Figure 5.9: comparison between neutron spectra from monenergetic and laser-driven proton beam on lithium solid target

5.4 Conclusion and suitability of laser-driven neutron sources for applications

As expected, lithium targets produce a neutron yields five times greater compared with beryllium ones, but they present several downsides such as the low melting point (180°) and the high chemical reactivity. The latter increases with target temperature and requires an adequate vacuum control. Beryllium targets, because of their high melting point (1278°) seem to be the easier and the cheaper way. In this case, the coolant is not needed and, considering the broad beam divergence and the low currents delivered by a laser system, the targets could run without suffering blistering problems.
The study investigated in detail how different experimental parameters affect the neutron yields and their angular distributions in a laser-driven neutron source. The neutron currents obtained in the simulation were of the order of $\sim 10^6$ - 10^7 $\frac{neutrons}{s}$. Even if these currents are not so high as in the case of conventional accelerators or reactor facilities, it is possible to think to exploit them for some applications. In particular, thermalizing the fluxes, in principle one should be able to perform the PGNAA 1.2.4. Exploiting the pulsed nature of the neutron source and synchronizing the detector system with the laser shot, it is possible to minimize the background signal or the false events like the capture of cosmic rays. Like in the experiment of Harling [34], where the used flux was of $\sim 10^6$ $\frac{n}{cm^2 s}$, with laser-driven sources one should be able to reveal the presence B, Gd, Cd, and Sm exploiting the PGNAA technique.
Considering the epithermal characteristics of the neutron spectra generated by laser-driven system, another suitable technique is the epithermal neutron acti-

vation analysis or the fast neutron activation analysis.
Recalling that in the neutron radiography experiments perfromed with other sources the neutron flux used was of $\sim 10^7 \frac{n}{cm^2 s}$ [3], this type of application could be also performed with laser driven sources. The experimental proof of radiography with laser-driven accelerated neutrons was performed by Roth et al. [65].
Considering the epithermal characteristic of the neutron beam, a future possible application could also be the BNCT [82].
Performing these techniques with a compact laser-driven system of tens of TW, instead of using nuclear reactor facilities, should present several advantages: the lowering of the costs of the experimental setup; the reduction of radioprotection issues and the contamination of neutron fluxes; the greater handling of the system, that can be easily put in place in a research center or industrial site; the possibility to think a portable sources, not forcing in situ measurement [64].

Chapter 6

Conclusion and perspectives

This thesis work is focused on numerical simulations of laser-driven neutron sources, considering in particular schemes based on laser-driven proton sources coupled with a suitable converter. Two main goals have been pursued: benchmarking the appropriate physical models of the Monte Carlo code Geant4 and assessing the effect of the peculiar features of a laser-driven proton source on neutron generation. Here a brief review of the outcomes of these investigations is presented, together with a discussion of the foreseen developments of the activity outlined in this document.

6.1 Validation of the code for low energy protons-induced reactions

In the literature there is a lack of data about the reliability of Geant4 for what concerns the important scenario of neutron generation with low energy protons (i.e. $\sim$ MeV) induced reactions. In chapter 3 there is a detailed description of all the physical models available in Geant4. As discussed in detail in the section §3.3.7, the main pre-compiled *physicslists* available in Geant4, in which the physical hadronic models are implemented are:

- *G4HadronPhysicsFTFP_BERT_HP*
- *G4HadronInelasticQBBC*
- *G4HadronPhysicsINCLXX*
- *G4HadronPhysicsQGSP_BIC_HP*
- *G4HadronPhysicsQGSP_BIC_AllHP*

The first four *physicslists* contain theory-driven models, while the latter contains data-driven model. All the models are explained in detail in the section §3.3.3.
In chapter 4 all these physical models are tested and their outputs are compared with experimental or theoretical works present in literature. A review of these works is given in section 2.5.3. For low energy impacting particles (from 0 up to $\sim$ 10 MeV) the data-driven model, i.e that model that takes the cross sections

and the decay probabilities from evaluated data libraries, provides a good reliability of the code. The cross sections to which the data-driven model refers are contained in the ENDF/B-VII [14] or in the TENDL [15] data libraries. The ENDF/B-VII data library contains very detailed cross-sections for some selected elements. For elements which are not contained in this library, data are taken from the TENDL library. These data are not derived from experiments, but are computed through the TALYS code, a software for the simulation of nuclear reactions: despite the order of magnitude is right considered, the real shape is approximated and some important features like the peaks and the resonances could not be taken into account. The overall precision of the model arising from the benchmark is about 20%.
Theory-driven models, even though well validated for high energy physics, fail catastrophically in reproducing the experimental data. This is evident in the case of monoenergetic proton beam of 2.25 MeV impinging on lithium target. At this energy, protons should explore the 580 mb resonance in the ^{7}Li(p,n)^{7}Be cross section 4.8, maximizing the neutron production, but the prediction of the theory-driven model is of zero produced neutrons. In the case of beryllium targets the underestimation of the yields is of two orders of magnitude. With these models, in the considered energy range, the code is totally unreliable.
Have figured out that the data-driven model is reliable in these range of energy, and its grade of precision, it is an important results for everyone which would like to simulate similar situations. Moreover, this allows to trust the results of the simulations performed in the second part of the thesis work.
The possibility to perform reliable numerical simulations is important especially in the view of pursuing future experimental activities. It offers the possibility to investigate the radioprotection issues and to design the shielding and the experimental set-up.

6.2 Laser-driven vs monoenergetic proton beams

The features of a laser-driven proton beam are different compared to the ones of a conventional accelerator 2.5.4: the typical energetic distribution is exponential-like, and the typical beam divergence is from 6° to 10°. It is of great importance to understand how these differences affect the neutron generation (yields, energy spectra and angular distribution). In the section §5, an ideal laser-driven exponential proton spectrum, taken from literature data [10], is implemented as the primary beam of Geant4. As a parameter of comparison between laser-driven and monoenergetic case, the mean energy of the exponential spectrum (2.66 MeV) was set equal to the energy of the monoenergetic beam. It is important to underline that the lower cut-off of the exponential spectrum (2 MeV) is not physical, because the real spectrum extends at energies below 2 MeV. This choice was made because the cross section (p,n), both for lithium and for beryllium, becomes important for energies greater than 2 MeV and it is not useful to simulate protons under the reaction threshold.
In general, for the same number of protons impinging on the converters, the yields are similar for laser-driven and monoenergetic cases, while the neutron energy spectra are wider for the laser-driven case. This is in agreement with the fact that in the exponential spectrum there are more energetic protons that

lead to more energetic neutrons.
In particular, for the beryllium case, compared to the monoenergetic beam, the neutron yields from the laser-driven beams are approximately double. The neutron energy spectra are wider because the more energetic protons are able to excite higher energy levels in ^{9}B, but also to release more energetic neutrons from the three-body breakup. For proton energies greater than 3 MeV, the σ(p, p' n) cross section becomes important, and the presence of three-body breakup neutrons implies more forward peaked angular distributions.
In the case of lithium the yields between monoenergetic and laser-driven cases are very similar, because a large amount of neutrons results from the 580 mb peak in the ^{7}Li(p,n)^{7}Be cross section. As in the case of beryllium, the neutron energy spectra are wider, and this is related to the fact that more energetic protons can excite higher level in the compound nucleus ^{8}Be. Angular distributions from monoenergetic and laser-driven case are similar forward-peaked, and this is due to the presence in both cases of neutrons generated from protons with kinetic energies near reaction threshold.
The neutron yields arising from the lithium converters are $\sim$ 5 times the yileds from beryllium converters. The maximum neutron energy achieved is $\sim$ 5 MeV for both converters.
Considering the obtained neutron yields and energy spectra, is important to understand which applications are more promising for a laser-driven source. Between the possible applications presented in chapter 1.2 the more realistic to be realized with a laser-driven systems are the NAA, the PGNAA 1.2.4 or neutron radiographies 1.2.3. The PGNAA is particularly suitable for laser driven-neutron sources: synchronizing the detector system with the laser shot is possible to obtain more accurate measurements. Considering the epithermal features of the obtained neutron fluxes, with the improvement of the technique other applications could be the BNCT 1.2.5.

6.3 Perspective and open issues

The advantages of the laser-driven systems reside in their compactness and in the reduced costs of the experimental setup, if compared with conventional accelerator or nuclear reactor facilities. A compact table-top laser of tens of TW could be able to produce a proton beam whose features in term of energy and intensity are capable to induce proton-neutron reaction. In principle such system should also offer the great benefit of portability, not forcing in-sito measures. The reduction of the costs, the simplification of the experimental facility and the greater manoeuvrability of the system are the main motivations that encourage the research in this fields.
A natural extension of this work is to sharpen the numerical method, implementing new simulations in which different aspects are taken into account. First of all it is necessary to consider more realistic laser-driven proton spectra, and this could be done coupling the Monte-Carlo code with particle-in-cell (PIC) simulations [1]. Furthermore, when a laser interacts with solid target, not only protons and ions are accelerated, but also a great amount of electrons 2.18. The energies of these electrons are suitable for generating bremsstrahlung radiation

[1] PIC simulations are a standard numeric technique to simulate the laser-plasma interaction [83]

as they stop in a metal converter, opening the possibility to induce the (γ,n) nuclear reactions and thus to release neutrons. An extension of this work could be the study of more complex systems based on double converters: the first made of copper or tungsten, to exploit the electron induced (γ,n) reactions, and the second made of beryllium, to exploit the (p,n) reaction. It is possible also to use only a beryllium target into which both (p,n) reaction and electron induced (γ,n) reactions are exploited [84, 12].In this scenario, the PIC simulations are able not only to provide a real laser-driven proton spectra, but can be also exploited to simulate the emitted electrons.
On this path, it is also possible to insert in the simulations some elements that behave as detectors with a given efficiency, in order to predict future experimental data. In the simulations presented in this thesis work, all the particles generated were ideally counted and registered by the envelope. This is far from the real scenario, but it was necessary to understand the behaviour of the code and to benchmark the results against literature data.
After a deep investigation of the problem with numerical simulation, the next step is to perform experiments to prove the effectiveness of the technique. Having at disposal reliable numerical instruments is important to design the experimental apparatus and addressing radioprotection issues. It is also useful to interpret the experimental results.
Laser-driven neutron sources hold promise to provide compact, inexpensive neutron sources, appealing for both scientific and technological applications. Several challenges have to be faced to make this a reality. However, high intensity laser technology is progressing fast [85] and recent developments on laser-driven sources could allow to increase the yield of the primary particle source [60, 10]. Moreover, a growing attention has been given recently to high-repetition rate target solutions for laser-driven sources [86], which might enable repetitive operation. The pace of the aformentioned developments make the outlook for laser-driven neutron sources promising. If the development of laser-driven neutron sources will hold up to expectations, they could become an important tool for a variety of applications such as NAA, PGNAA, neutron radiography and BNCT [68].

Bibliography

[1] Thomas Gnäupel-Herold. Techniques for neutron stress determination with high spatial resolution.

[2] M. E. Fitzpatrick and A. Lodini. Analysis of Residual Stress by Diffraction using Neutron and Synchrotron Radiation. *CRC Press*, February 2003.

[3] F. C. de Beer, M. Coetzer, D. Fendeis, and A. Da Costa E Silva. Neutron radiography and other NDE tests of main rotor helicopter blades. *Applied Radiation and Isotopes*, 61(4):609–616, October 2004.

[4] L. Chen, F. Ma, X. Y. Zhanga, Y. Q. Ju, H. B. Zhang, H. L. Ge, J. G. Wang, B. Zhou, Y. Y. Li, X. W. Xu, P. Luo, L. Yang, Y. B. Zhang, J. Y. Li, J. K. Xu, T. J. Liang, S. L. Wang, Y. W. Yang, and L. Gu. Spallation yield of neutrons produced in thick lead target bombarded with 250mev protons. *Nuclear Instruments and Methods in Physics Research Section B: Beam Interactions with Materials and Atoms*, 342:87–90, January 2015.

[5] W. B. Howard, S. M. Grimes, T. N. Massey, S. I. Al-Quraishi, D. K. Jacobs, C. E. Brient, and J. C. Yanch. Measurement of the Thick-Target 9be(p,n) Neutron Energy Spectra. *Nuclear Science and Engineering*, 138(2):145–160, June 2001.

[6] Jerry B. Marion. Excited States in 10b. *Physical Review*, 103(3):713–717, August 1956.

[7] S. Agosteo, P. Colautti, J. Esposito, A. Fazzi, M. V. Introini, and A. Pola. Characterization of the energy distribution of neutrons generated by 5mev protons on a thick beryllium target at different emission angles. *Applied Radiation and Isotopes*, 69(12):1664–1667, December 2011.

[8] J Guzek, W. R McMurray, T Mateva, C. B Franklyn, and U. A. S Tapper. Characterisation of neutron and gamma-ray emission from thick target Be(p,n) reaction for boron neutron capture therapy. *Nuclear Instruments and Methods in Physics Research Section B: Beam Interactions with Materials and Atoms*, 139(1):471–475, April 1998.

[9] R. A. Snavely, M. H. Key, S. P. Hatchett, T. E. Cowan, M. Roth, T. W. Phillips, M. A. Stoyer, E. A. Henry, T. C. Sangster, M. S. Singh, S. C. Wilks, A. MacKinnon, A. Offenberger, D. M. Pennington, K. Yasuike, A. B. Langdon, B. F. Lasinski, J. Johnson, M. D. Perry, and E. M. Campbell. Intense High-Energy Proton Beams from Petawatt-Laser Irradiation of Solids. *Physical Review Letters*, 85(14):2945–2948, October 2000.

[10] M. Passoni, A. Sgattoni, I. Prencipe, L. Fedeli, D. Dellasega, L. Cialfi, Il Woo Choi, I Jong Kim, K. A. Janulewicz, Hwang Woon Lee, Jae Hee Sung, Seong Ku Lee, and Chang Hee Nam. Toward high-energy laser-driven ion beams: Nanostructured double-layer targets. *Physical Review Accelerators and Beams*, 19(6):061301, June 2016.

[11] M. Borghesi, A. Bigongiari, S. Kar, A. Macchi, L. Romagnani, P. Audebert, J. Fuchs, T. Toncian, O. Willi, S. V. Bulanov, A. J. Mackinnon, and J. C. Gauthier. Laser-driven proton acceleration: source optimization and radiographic applications. *Plasma Physics and Controlled Fusion*, 50(12):124040, 2008.

[12] I. Pomerantz, E. McCary, A. R. Meadows, A. Arefiev, A. C. Bernstein, C. Chester, J. Cortez, M. E. Donovan, G. Dyer, E. W. Gaul, D. Hamilton, D. Kuk, A. C. Lestrade, C. Wang, T. Ditmire, and B. M. Hegelich. Ultrashort Pulsed Neutron Source. *Physical Review Letters*, 113(18):184801, October 2014.

[13] S. Agostinelli, J. Allison, K. Amako, J. Apostolakis, H. Araujo, P. Arce, M. Asai, D. Axen, S. Banerjee, G. Barrand, F. Behner, L. Bellagamba, J. Boudreau, L. Broglia, A. Brunengo, H. Burkhardt, S. Chauvie, J. Chuma, R. Chytracek, G. Cooperman, G. Cosmo, P. Degtyarenko, A. Dell'Acqua, G. Depaola, D. Dietrich, R. Enami, A. Feliciello, C. Ferguson, H. Fesefeldt, G. Folger, F. Foppiano, A. Forti, S. Garelli, S. Giani, R. Giannitrapani, D. Gibin, J. J. Gómez Cadenas, I. González, G. Gracia Abril, G. Greeniaus, W. Greiner, V. Grichine, A. Grossheim, S. Guatelli, P. Gumplinger, R. Hamatsu, K. Hashimoto, H. Hasui, A. Heikkinen, A. Howard, V. Ivanchenko, A. Johnson, F. W. Jones, J. Kallenbach, N. Kanaya, M. Kawabata, Y. Kawabata, M. Kawaguti, S. Kelner, P. Kent, A. Kimura, T. Kodama, R. Kokoulin, M. Kossov, H. Kurashige, E. Lamanna, T. Lampén, V. Lara, V. Lefebure, F. Lei, M. Liendl, W. Lockman, F. Longo, S. Magni, M. Maire, E. Medernach, K. Minamimoto, P. Mora de Freitas, Y. Morita, K. Murakami, M. Nagamatu, R. Nartallo, P. Nieminen, T. Nishimura, K. Ohtsubo, M. Okamura, S. O'Neale, Y. Oohata, K. Paech, J. Perl, A. Pfeiffer, M. G. Pia, F. Ranjard, A. Rybin, S. Sadilov, E. Di Salvo, G. Santin, T. Sasaki, N. Savvas, Y. Sawada, S. Scherer, S. Sei, V. Sirotenko, D. Smith, N. Starkov, H. Stoecker, J. Sulkimo, M. Takahata, S. Tanaka, E. Tcherniaev, E. Safai Tehrani, M. Tropeano, P. Truscott, H. Uno, L. Urban, P. Urban, M. Verderi, A. Walkden, W. Wander, H. Weber, J. P. Wellisch, T. Wenaus, D. C. Williams, D. Wright, T. Yamada, H. Yoshida, and D. Zschiesche. Geant4—a simulation toolkit. *Nuclear Instruments and Methods in Physics Research Section A: Accelerators, Spectrometers, Detectors and Associated Equipment*, 506(3):250–303, July 2003.

[14] Endf https://www-nds.iaea.org/exfor/endf.html, 2018.

[15] Tendl $https://tendl.web.psi.ch/tendl_2015/tendl2015.html$, 2015.

[16] Perkins. *Introduction To High Energy Physics*. 2000.

[17] Karl Heinrich Lieser. *Nuclear and radiochemistry*. 2001.

[18] Krane. *Introductory Nuclear Physics*. 1987.

[19] C.L. Lee and X.-L Zhou. Thick target neutron yields for the 7li(p,n)7be reaction near threshold. *Nuclear Instruments and Methods in Physics Research Section B: Beam Interactions with Materials and Atoms*, 152:1–11, April 1999.

[20] Weixiang Yu Gang Yue Xiaogang Han Jinxiang Chen Bo Tian. Measurements of the neutron yields from 7li(p,n)7be reaction (thick target) with incident energies from 1.885 to 2.0 mev. *Medical Physics 25, 1222 (1998); doi: 10.1118/1.598299*, 1998.

[21] B. Bayanov, A. Burdakov, V. Chudaev, A. Ivanov, S. Konstantinov, A. Kuznetsov, A. Makarov, G. Malyshkin, K. Mekler, I. Sorokin, Yu. Sulyaev, and S. Taskaev. First neutron generation in the BINP accelerator based neutron source. *Applied Radiation and Isotopes*, 67(7, Supplement):S285–S287, July 2009.

[22] L Koester A. Steyerl. *Physics of Neutron*. 1977.

[23] Luis W. Alvarez and F. Bloch. A Quantitative Determination of the Neutron Moment in Absolute Nuclear Magnetons. *Physical Review*, 57(2):111–122, January 1940.

[24] K.A. Olive. Particle data group. *China Physics*, 2014.

[25] James Chadwick. The neutron and its properties. *Nobel Lecture*, 1935.

[26] Davydov. *Quantum mechanics*. 1965.

[27] L. Greim A. Harms H. P. Leeflang J. F. W. Markgraf R. Matfield D. J. Taylor G. Bayon, J. C. Domanus. *PRACTICAL NEUTRON RADIOGRAPHY*. 1992.

[28] Peng Zhang, Zhaolin Liu, Songbai Han, Linfeng He, Harald S. Müller, Tiejun Zhao, and Yu Wang. Visualization ofstudy the penetration of water and other aqueous solutions into cracked cementitious specimens. the neutron flux that irradiated the cracked samples was of $1.2 \times 10^8 \frac{n}{cm^2 s}$ and a a 0.1 mm thick neutron sensitive 6 lif/zns scintillation screen was used. the process of water penetration into the cracked rapid penetration of water into cracked cement mortar using neutron radiography. *Materials Letters*, 195:1–4, May 2017.

[29] S. Landsberger, R. Kapsimalis, and J. Dolloff. Measuring activity of 235u, 238u, 232th and 40k in geological materials using neutron activation analysis. *Journal of Radioanalytical and Nuclear Chemistry*, 296(1):323–327, April 2013.

[30] A. A. Faust, J. E. McFee, C. L. Bowman, C. Mosquera, H. R. Andrews, V. D. Kovaltchouk, and H. Ing. Feasibility of fast neutron analysis for the detection of explosives buried in soil. *Nuclear Instruments and Methods in Physics Research Section A: Accelerators, Spectrometers, Detectors and Associated Equipment*, 659(1):591–601, December 2011.

[31] K. Randle. The applications of fast neutron activation analysis (FNAA) at Birmingham. *Nuclear Instruments and Methods in Physics Research Section B: Beam Interactions with Materials and Atoms*, 24-25:1010–1013, April 1987.

[32] D. Brune and B. Bivered. Epithermal neutron activation analysis of elements present in trace quantities in biological materials. *Analytica Chimica Acta*, 85(2):411–414, September 1976.

[33] J. L. Ma, C. Carasco, B. Perot, E. Mauerhofer, J. Kettler, and A. Havenith. Prompt gamma neutron activation analysis of toxic elements in radioactive waste packages. *Applied Radiation and Isotopes*, 70(7):1261–1263, July 2012.

[34] Otto K. Harling, Jean-Michel Chabeuf, Frédérique Lambert, and Gopika Yasuda. A prompt gamma neutron activation analysis facility using a diffracted beam. *Nuclear Instruments and Methods in Physics Research Section B: Beam Interactions with Materials and Atoms*, 83(4):557–562, December 1993.

[35] Bangfa Ni, Caijing Xiao, Donghui Huang, Hongchao Sun, Guiying Zhang, Cunxiong Liu, Pingsheng Wang, Haiqing Zhang, and Weizhi Tian. A brief introduction to NAA facilities of China Advance Research Reactor at CIAE. *Journal of Radioanalytical and Nuclear Chemistry*, 291(2):313–319, February 2012.

[36] Raymond L. Moss. Critical review, with an optimistic outlook, on Boron Neutron Capture Therapy (BNCT). *Applied Radiation and Isotopes*, 88:2–11, June 2014.

[37] Maurizio Pelliccioni. *Fondamenti fisici della radioprotezione*. 1992.

[38] Leonardo Gagetti, Manuel Suarez Anzorena, Alma Bertolo, Mariela del Grosso, and Andrés J. Kreiner. Proton irradiation of beryllium deposits on different candidate materials to be used as a neutron production target for accelerator-based BNCT. *Nuclear Instruments and Methods in Physics Research Section A: Accelerators, Spectrometers, Detectors and Associated Equipment*, 874:28–34, December 2017.

[39] O. K. Harling, K. J. Riley, T. H. Newton, B. A. Wilson, S. Sakamoto, and B. Sutharshan. The new fission converter based epithermal neutron irradiation facility for neutron capture therapy. *Neutron News*, 12(1):24–26, January 2001.

[40] D. F. Chen, Y. T. Liu, and M. M. Wu. The Neutron Scattering Program at the China Advanced Research Reactor (CARR): A Progress Report. *Neutron News*, 20(2):32–35, May 2009.

[41] D. F. Chen, Y. T. Liu, C. Gou, and C. T. Ye. Development of neutron scattering on 60 MW research reactor in CIAE. *Physica B Condensed Matter*, 385:966–967, November 2006.

[42] J. Cugnon. A Short Introduction to Spallation Reactions. *Few-Body Systems*, 53(1-2):143–149, July 2012.

[43] J. Jurns, J. Ringnér, H. Quack, P. Arnold, J. G. Weisend II, and D. Lyngh. Spallation target cryogenic cooling design challenges at the european spallation source. 101.

[44] Alain Letourneau, Anthony Marchix, Ngoc-Hoang Tran, Nicolas Chauvin, Alain Menelle, Frédéric Ott, and Jérôme Schwindling. Development of compact accelerator neutron source. *EPJ Web of Conferences*, 146:03018, 2017.

[45] Yu Efremenko and W. R. Hix. Opportunities for neutrino physics at the Spallation Neutron Source (SNS). *Journal of Physics: Conference Series*, 173(1):012006, 2009.

[46] Xueying Zhang, Yanbin Zhang, Fei Ma, Yongqin Ju, Liang Chen, Hongbin Zhang, Yanyan Li, Bo Wan, Jianguo Wang, and Honglin Ge. Neutron production for 250 MeV protons bombarding on thick grain-made tungsten target. *The European Physical Journal A*, 51(8):106, August 2015.

[47] Cheol Ho PYEON, Hiroshi SHIGA, Kazuaki ABE, Hiroshi YASHIMA, Teiji NISHIO, Tsuyoshi MISAWA, Tomohiko IWASAKI, and Seiji SHIROYA. Reaction Rate Analysis of Nuclear Spallation Reactions Generated by 150, 190, and 235mev Protons. *Journal of Nuclear Science and Technology*, 47(11):1090–1095, November 2010.

[48] Jerry B. Marion and Jules S. Levin. Investigation of the 9be(p,n)9b and be(a,ti)li 6 reactions. *Physical Review*, 115(1):144–149, July 1959.

[49] Martin Schiemann, Jeffrey Bergthorson, Peter Fischer, Viktor Scherer, Dan Taroata, and Günther Schmid. A review on lithium combustion. *Applied Energy*, 162:948–965, January 2016.

[50] R. L. Macklin and J. H. Gibbons. Study of the t(p,n)3he and 7li(p,n)7be reactions. *Physical Review*, 109(1):105–109, January 1958.

[51] Yutaka Yamagata, Katsuya Hirota, Jungmyoung Ju, Sheng Wang, Shin-ya Morita, Jun-ichi Kato, Yoshie Otake, Atsushi Taketani, Yoshichika Seki, Masako Yamada, Hideo Ota, Unico Bautista, and Qinngan Jia. Development of a neutron generating target for compact neutron sources using low energy proton beams. *Journal of Radioanalytical and Nuclear Chemistry*, 305(3):787–794, September 2015.

[52] B. F. Bayanov, E. V. Zhurov, and S. Yu Taskaev. Measuring the lithium layer thickness. *Instruments and Experimental Techniques*, 51(1):147–149, January 2008.

[53] B Bayanov, V Belov, V Kindyuk, E Oparin, and S Taskaev. Lithium neutron producing target for BINP accelerator-based neutron source. *Applied Radiation and Isotopes*, 61(5):817–821, November 2004.

[54] Carl Willis, John Lenz, and Donald Swenson. High-power lithium target for accelerator-based BNCT. *Proceedings of the 24th Linear Accelerator Conference, LINAC 2008*, January 2009.

[55] S. Halfon, A. Arenshtam, D. Kijel, M. Paul, L. Weissman, D. Berkovits, I. Eliyahu, G. Feinberg, A. Kreisel, I. Mardor, G. Shimel, A. Shor, I. Silverman, and M. Tessler. Demonstration of a high-intensity neutron source based on a liquid-lithium target for Accelerator based Boron Neutron Capture Therapy. *Applied Radiation and Isotopes*, 106:57–62, December 2015.

[56] Andrea Macchi, Marco Borghesi, and Matteo Passoni. Ion acceleration by superintense laser-plasma interaction. *Reviews of Modern Physics*, 85(2):751–793, May 2013.

[57] Hiroyuki Daido, Mamiko Nishiuchi, and Alexander S Pirozhkov. Review of laser-driven ion sources and their applications. 75, May 2012. DOI: 10.1088/0034-4885/75/5/056401.

[58] Andrea Macchi. *A Superintense Laser–Plasma Interaction Theory Primer*. 2013.

[59] Stephen P. Hatchett, Curtis G. Brown, Thomas E. Cowan, Eugene A. Henry, Joy S. Johnson, Michael H. Key, Jeffrey A. Koch, A. Bruce Langdon, Barbara F. Lasinski, Richard W. Lee, Andrew J. Mackinnon, Deanna M. Pennington, Michael D. Perry, Thomas W. Phillips, Markus Roth, T. Craig Sangster, Mike S. Singh, Richard A. Snavely, Mark A. Stoyer, Scott C. Wilks, and Kazuhito Yasuike. Electron, photon, and ion beams from the relativistic interaction of Petawatt laser pulses with solid targets. *Physics of Plasmas*, 7(5):2076–2082, April 2000.

[60] I. Prencipe, A. Sgattoni, D. Dellasega, L. Fedeli, L. Cialfi, Il Woo Choi, I. Jong Kim, K. A. Janulewicz, K. F. Kakolee, Hwang Woon Lee, Jae Hee Sung, Seong Ku Lee, Chang Hee Nam, and M. Passoni. Development of foam-based layered targets for laser-driven ion beam production. *Plasma Physics and Controlled Fusion*, 58(3):034019, 2016.

[61] A. Sgattoni, P. Londrillo, A. Macchi, and M. Passoni. Laser ion acceleration using a solid target coupled with a low-density layer. 85(3).

[62] A. Higginson, R. J. Gray, M. King, R. J. Dance, S. D. R. Williamson, N. M. H. Butler, R. Wilson, R. Capdessus, C. Armstrong, J. S. Green, S. J. Hawkes, P. Martin, W. Q. Wei, S. R. Mirfayzi, X. H. Yuan, S. Kar, M. Borghesi, R. J. Clarke, D. Neely, and P. McKenna. Near-100 MeV protons via a laser-driven transparency-enhanced hybrid acceleration scheme. *Nature Communications*, 9(1):724, February 2018.

[63] M. Storm, S. Jiang, D. Wertepny, C. Orban, J. Morrison, C. Willis, E. McCary, P. Belancourt, J. Snyder, E. Chowdhury, W. Bang, E. Gaul, G. Dyer, T. Ditmire, R. R. Freeman, and K. Akli. Fast neutron production from lithium converters and laser driven protons. *Physics of Plasmas*, 20(5):053106, May 2013.

[64] C. M. Brenner, S. R. Mirfayzi, D. R. Rusby, C. Armstrong, A. Alejo, L. A. Wilson, R. Clarke, H. Ahmed, N. M. H. Butler, D Haddock, A. Higginson, A. McClymont, C. Murphy, M. Notley, P. Oliver, R. Allott, C. Hernandez-Gomez, S. Kar, P McKenna, and D. Neely. Laser-driven x-ray and neutron source development for industrial applications of plasma accelerators. *Plasma Physics and Controlled Fusion*, 58(1):014039, 2016.

[65] M. Roth, D. Jung, K. Falk, N. Guler, O. Deppert, M. Devlin, A. Favalli, J. Fernandez, D. Gautier, M. Geissel, R. Haight, C. E. Hamilton, B. M. Hegelich, R. P. Johnson, F. Merrill, G. Schaumann, K. Schoenberg, M. Schollmeier, T. Shimada, T. Taddeucci, J. L. Tybo, F. Wagner, S. A. Wender, C. H. Wilde, and G. A. Wurden. Bright Laser-Driven Neutron Source Based on the Relativistic Transparency of Solids. *Physical Review Letters*, 110(4):044802, January 2013.

[66] D. Jung, K. Falk, N. Guler, O. Deppert, M. Devlin, A. Favalli, J. C. Fernandez, D. C. Gautier, M. Geissel, R. Haight, C. E. Hamilton, B. M. Hegelich, R. P. Johnson, F. Merrill, G. Schaumann, K. Schoenberg, M. Schollmeier, T. Shimada, T. Taddeucci, J. L. Tybo, S. A. Wender, C. H. Wilde, G. A. Wurden, and M. Roth. Characterization of a novel, short pulse laser-driven neutron source. *Physics of Plasmas*, 20(5):056706, May 2013.

[67] S. R. Mirfayzi, A. Alejo, H. Ahmed, D. Raspino, S. Ansell, L. A. Wilson, C. Armstrong, N. M. H. Butler, R. J. Clarke, A. Higginson, J. Kelleher, C. D. Murphy, M. Notley, D. R. Rusby, E. Schooneveld, M. Borghesi, P. McKenna, N. J. Rhodes, D. Neely, C. M. Brenner, and S. Kar. Experimental demonstration of a compact epithermal neutron source based on a high power laser. *Applied Physics Letters*, 111(4):044101, July 2017.

[68] A. Alejo, H. Ahmed, A. Green, S. R. Mirfayzi, M. Borghesi, and S. Kar. Recent advances in laser-driven neutron sources. *Il Nuovo Cimento C*, 38C(6):1–7, May 2016.

[69] Geant4 collaboration. Geant4 http://geant4.cern.ch/, 2018.

[70] Geant4 Collaboration. *Geant4 User's Guide for Application Developers*. 2016.

[71] Nist group. Standard reference data https://www.nist.gov/srd, 2018.

[72] Geant4 Collaboration. *Physics Reference Manual*. 2017.

[73] M. J. Berger, M. Inokuti, H. H. Andersen, H. Bichsel, D. Powers, S. M. Seltzer, D. Thwaites, and D. E. Watt. Report 49. *Journal of the International Commission on Radiation Units and Measurements*, os25(2):NP–NP, May 1993.

[74] Eadl, https://inis.iaea.org, 2018.

[75] J. Apostolakis, M. Asai, A. G. Bogdanov, H. Burkhardt, G. Cosmo, S. Elles, G. Folger, V. M. Grichine, P. Gumplinger, A. Heikkinen, I. Hrivnacova, V. N. Ivanchenko, J. Jacquemier, T. Koi, R. P. Kokoulin, M. Kossov, H. Kurashige, I. McLaren, O. Link, M. Maire, W. Pokorski, T. Sasaki, N. Starkov, L. Urban, and D. H. Wright. Geometry and physics of the Geant4 toolkit for high and medium energy applications. *Radiation Physics and Chemistry*, 78(10):859–873, October 2009.

[76] V. Lara and J. P. Wellisch. Pre-equilibrium and equilibrium decays in Geant4. *CERN Document Server*, 2000.

[77] Ensdf https://www.nndc.bnl.gov/ensdf/, 2018.

[78] Geant4 Collaboration. *Guide For Physics Lists*. 2017.

[79] Srim - the stopping and range of ions in matter www.srim.org, 2018.

[80] sigma aldrich https://www.sigmaaldrich.com.

[81] Goodfellow: All the materials you need for scientific and industrial research and manufacturing http://www.goodfellow.com/e/beryllium-foil.html.

[82] J. Alvarez, J. Fernández-Tobias, K. Mima, S. Nakai, S. Kar, Y. Kato, and J. M. Perlado. Laser Driven Neutron Sources: Characteristics, Applications and Prospects. *Physics Procedia*, 60:29–38, January 2014.

[83] T. D. Arber, K. Bennett, C. S. Brady, A. Lawrence-Douglas, M. G. Ramsay, N. J. Sircombe, P. Gillies, R. G. Evans, H Schmitz, A. R. Bell, and C. P. Ridgers. Contemporary particle-in-cell approach to laser-plasma modelling. *Plasma Physics and Controlled Fusion*, 57(11):113001, 2015.

[84] F Jallu, A Lyoussi, E Payan, H Recroix, A Mariani, G Nurdin, A Buisson, and J Allano. Photoneutron production in tungsten, praseodymium, copper and beryllium by using high energy electron linear accelerator. *Nuclear Instruments and Methods in Physics Research Section B: Beam Interactions with Materials and Atoms*, 155(4):373–381, September 1999.

[85] Colin Danson, David Hillier, Nicholas Hopps, and David Neely. Petawatt class lasers worldwide. *High Power Laser Science and Engineering*, 3, 2015.

[86] I. Prencipe, J. Fuchs, S. Pascarelli, D. W. Schumacher, R. B. Stephens, N. B. Alexander, R. Briggs, M. Büscher, M. O. Cernaianu, A. Choukourov, M. De Marco, A. Erbe, J. Fassbender, G. Fiquet, P. Fitzsimmons, C. Gheorghiu, J. Hund, L. G. Huang, M. Harmand, N. J. Hartley, A. Irman, T. Kluge, Z. Konopkova, S. Kraft, D. Kraus, V. Leca, D. Margarone, J. Metzkes, K. Nagai, W. Nazarov, P. Lutoslawski, D. Papp, M. Passoni, A. Pelka, J. P. Perin, J. Schulz, M. Smid, C. Spindloe, S. Steinke, R. Torchio, C. Vass, T. Wiste, R. Zaffino, K. Zeil, T. Tschentscher, U. Schramm, and T. E. Cowan. Targets for high repetition rate laser facilities: needs, challenges and perspectives. *High Power Laser Science and Engineering*, 5, 2017.